

AD-A206 011



DISTRIBUTION STATEMENT A

Approved for public release
Distribution Unlimited

DEPARTMENT OF THE AIR FORCE

AIR UNIVERSITY

AIR FORCE INSTITUTE OF TECHNOLOGY

Wright-Patterson Air Force Base, Ohio

Best Available Copy

1 80 4 02 030

DTIC
ELE
APR 04 1989
S D
D Cg

AFIT/GAE/AA/89M-1

①

DTIC
ELEC
S APR 04 1989 D
D C

TWO-DIMENSIONAL CONFINED JET
THRUST VECTOR CONTROL:
OPERATING MECHANISMS
AND PERFORMANCE

THESIS

Jeffrey L. Caton
Captain, USAF

AFIT/GAE/AA/89M-1

Approved for public release; distribution unlimited

TWO-DIMENSIONAL CONFINED JET
THRUST VECTOR CONTROL:
OPERATING MECHANISMS
AND PERFORMANCE

THESIS

Presented to the Faculty of the School of Engineering
of the Air Force Institute of Technology

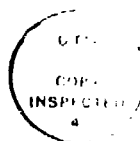
Air University

In Partial Fulfillment of the
Requirements for the Degree of
Master of Science in Aeronautical Engineering

Jeffrey L. Caton, B.S.Ch.E.

Captain, USAF

March, 1989



Accession For	
NTIS CRA&I	<input checked="" type="checkbox"/>
DTIC TAB	<input type="checkbox"/>
Unannounced	<input type="checkbox"/>
Justification _____	
By _____	
Distribution /	
Availability Codes	
Dist	Avail and/or Special
A-1	

Approved for public release; distribution unlimited

Preface

In this thesis, I continued the work performed by several previous students at AFIT on confined jet thrust vector control nozzles. My primary goal was to develop an understanding of the vector operating mechanisms and performance parameters that could lead to further design optimization. The nozzle test assemblies I used were designed at AFIT, while most of my report data was taken from experiments performed at the von Karman Institute for Fluid Dynamics in Belgium.

Although many people contributed to this project, it could not have been accomplished without the following individuals' understanding and dedication. Dr. M. Franke was my mentor for this work who not only provided the foundation for the study, but also continued to help with every detail. Dr. W. Elrod helped me to meet impossible deadlines for my prototype test, sometimes at the cost of his own studies. John Brohas turned crude drawings on paper into exceptionally high quality test articles, also with impossible deadlines.

At the von Karman Institute, Dr. M. Carbonaro provided me with theoretical and practical guidance essential to my studies. Messrs R. Conniasselle and R. Voet created my test facilities at VKI and patiently helped me with numerous modifications. Messr Lobert provided exceptional service in helping me to create my schlieren photographs.

Finally, my wife, Linda, patiently accepted my four

months absence to Belgium only to end up typing all of the following pages when I returned. She was helpful with my studies, but remains invaluable to my life.

- Jeffrey L. Caton

Table of Contents

	Page
Preface	ii
List of Figures	vi
List of Tables	xi
List of Acronyms	xii
List of Symbols	xiii
Abstract	xvii
I. Introduction	1
Background	1
Secondary Injection Thrust Vector Control (SITVC)	2
Previous CJTVC Work	4
Goal and Objectives	5
II. Experimental Apparatus	7
Nozzle Design	7
Test Model Design	9
Test Facilities	14
III. Nozzle Operating Mechanisms Results	17
Separation Studies (no secondary injection)	17
Shock Structures (no secondary injection)	24
Flow Visualization Observations	31
IV. Nozzle Performance Results	36
Performance with No Secondary Flow	36
Thrust Force and Vector Angle	36
Thrust Efficiencies	44
Performance with Secondary Flow	49
Vector Angles	49
Thrust Efficiencies	58
Side Momentum Gains	59
Static Pressure Profiles	68
Nozzle Switching Response	73
Summary	80
V. Nozzle Analytical Model Results	85
Viscous Effects Analysis	85
Side Force to Axial Force Ratio Models	86

	Shock Loss Model	91
VI.	Conclusions	104
VII.	Recommendations	106
	Appendix A	107
	Appendix B	111
	Appendix C	123
	Appendix D	126
	Bibliography	145
	Vita	147

List of Figures

Figure	Page
1. Boundary Layer Thrust Vector Control (BLTVC) System	3
2. Confined Jet Thrust Vector Control (CJTVC) System	3
3. Basic Test Nozzle Design and Geometry Data	8
4. Test Nozzle Configurations	10
5. Wind Tunnel Model	12
6. Nozzle Test Assembly	13
7. Nozzle 0 Separation Schlieren Photographs	18
8. Nozzle 1 Separation Schlieren Photographs	19
9. Nozzle 3 Separation Schlieren Photographs	20
10. Nozzle 4 Separation Schlieren Photographs	21
11. Summary of Normalized Separation Lengths in Test Nozzles	22
12. Oblique Shock Flow Turning in Nozzles	25
13. Shock and Flow Structures for Nozzle 0 Primary Flow	27
14. Shock and Flow Structures for Nozzle 3	29
15. Shock and Flow Structures for Nozzle 4	30
16. Vectoring and Axial Flow for Nozzles 1 and 2	32
17. Vortex Formation in Nozzles	34
18. Nozzle 0 Forces and Vector Angles (no secondary flow)	37
19. Nozzle 1 Forces and Vector Angles (no secondary flow)	38
20. Nozzle 3 Forces and Vector Angles (no secondary flow)	39
21. Nozzle 4 Forces and Vector Angles (no secondary flow)	40
22. Nozzle 5 Forces and Vector Angles (no secondary flow)	41

23.	Summary of Nozzle Centerline Static Pressures	43
24.	Nozzle 0 Thrust Efficiencies (no secondary flow)	46
25.	Nozzle 1 Thrust Efficiencies (no secondary flow)	46
26.	Nozzle 3 Thrust Efficiencies (no secondary flow)	47
27.	Nozzle 4 Thrust Efficiencies (no secondary flow)	47
28.	Nozzle 5 Thrust Efficiencies (no secondary flow)	48
29.	Nozzle 1 Vector Angle and Side Force Variations	50
30.	Nozzle 2 Vector Angle and Side Force Variations	51
31.	Nozzle 3 Vector Angle and Side Force Variations	52
32.	Nozzle 4 Vector Angle and Side Force Variations	53
33.	Mass Flow Ratio versus Pressure Ratio (secondary flow to primary flow)	56
34.	Summary of Secondary Flow-Induced Vector Angle Ranges	57
35.	Vector Angle Range Variation with NPR	57
36.	Nozzle 1 Thrust Efficiencies (with secondary flow)	60
37.	Nozzle 2 Thrust Efficiencies (with secondary flow)	60
38.	Nozzle 3 Thrust Efficiencies (with secondary flow)	61
39.	Nozzle 4 Thrust Efficiencies (with secondary flow)	61
40.	Nozzle 1 Momentum Gains and Flow Momentum Ratios	64
41.	Nozzle 2 Momentum Gains and Flow Momentum Ratios	65

42.	Nozzle 3 Momentum Gains and Flow Momentum Ratios	66
43.	Nozzle 4 Momentum Gains and Flow Momentum Ratios	67
44.	Summary of Nozzle Centerline Pressures at Maximum Vector Angle Range (Average NPR = 40.5 ± 2.0)	69
45.	Summary of Nozzle Centerline Pressures at Maximum Vector Angle Range (Average NPR = 39.6 ± 2.1)	70
46.	Summary of Nozzle Centerline Pressures at Maximum Vector Angle Range (Average NPR = 39.0 ± 1.8)	72
47.	Secondary Flow Response Time Delays	75
48.	Nozzle 1 Side Force Oscilloscope Traces Test Cases 1-3	78
49.	Nozzle 1 Side Force Oscilloscope Traces Test Cases 4-6	79
50.	Nozzle 1 External Flow Schlieren Photographs	84
51.	Nozzle 1 Side to Axial Force Ratio Prediction Results	89
52.	Nozzle 2 Side to Axial Force Ratio Prediction Results	89
53.	Nozzle 3 Side to Axial Force Ratio Prediction Results	90
54.	Nozzle 4 Side to Axial Force Ratio Prediction Results	90
55.	Nozzle 1 Side to Axial Force Ratio Prediction Results with Modified Green/McCullough Model	93
56.	Nozzle 2 Side to Axial Force Ratio Prediction Results with Modified Green/McCullough Model	93
57.	Nozzle 3 Side to Axial Force Ratio Prediction Results with Modified Green/McCullough Model	94
58.	Nozzle 4 Side to Axial Force Ratio Prediction Results with Modified Green/McCullough Model	94

59.	Oblique Shock Formation in Nozzle Diverging Section	98
60.	Comparison of Loss Model and Measured Total Force Values for Nozzle 1	102
61.	Comparison of Loss Model and Measured Total Force Values for Nozzle 2	102
62.	Comparison of Loss Model and Measured Total Force Values for Nozzle 3	103
63.	Comparison of Loss Model and Measured Total Force Values for Nozzle 4	103
64.	Nozzle Design Details and Dimensions	108
65.	VKI Wind Tunnel Apparatus	109
66.	VKI Six Component Force Balance	110
67.	Nozzle Mass Flow Measurements	125
68.	Static Pressure Profiles for Test Number 890125.07	128
69.	Static Pressure Profiles for Test Number 890131.21	129
70.	Static Pressure Profiles for Test Number 890201.39	130
71.	Static Pressure Profiles for Test Number 890207.06	131
72.	Static Pressure Profiles for Test Number 890126.32	132
73.	Static Pressure Profiles for Test Number 890131.25	133
74.	Static Pressure Profiles for Test Number 890131.26	134
75.	Static Pressure Profiles for Test Number 890131.27	135
76.	Static Pressure Profiles for Test Number 890202.48	136
77.	Static Pressure Profiles for Test Number 890202.49	137
78.	Static Pressure Profiles for Test Number 890202.50	138

79.	Static Pressure Profiles for Test Number 890202.09	139
80.	Static Pressure Profiles for Test Number 890202.10	140
81.	Static Pressure Profiles for Test Number 890202.11	141
82.	Static Pressure Profiles for Test Number 890207.20	142
83.	Static Pressure Profiles for Test Number 890207.21	143
84.	Static Pressure Profiles for Test Number 890207.22	144

List of Tables

Table	Page
1. Nozzle Thrust Efficiencies with No Secondary Flow	48
2. Vector Angle Measured from Angle Produced by Both Secondary Flows	56
3. Best Vector Angle Range Values for Nozzles Tested	58
4. Nozzle Thrust Efficiencies with Secondary Flow	62
5. Nozzle Flow Vectoring Response Time Test Conditions	77
6. Nozzle 1 Flow Vectoring Response Times and Frequencies	81
7. Summary of Nozzle Best Vector Range Performance .	82
8. Average Error from Actual Results for Green/McCullough Side to Axial Force Prediction Model	92
9. Average Ratio of Total Force Calculated Using the Shock Loss Model to Measured Total Force . .	101

List of Acronyms

AFIT	Air Force Institute of Technology
BLTVC	Boundary Layer Thrust Vector Control
CEI	Commodore Extension Interface
CJTVC	Confined Jet Thrust Vector Control
MFR	Mass Flow Ratio (secondary to primary flows)
NPR	Nozzle Pressure Ratio (ratio of primary supply pressure to ambient pressure)
SI	Secondary Injection
SITVC	Secondary Injection Thrust Vector Control
TVC	Thrust Vector Control
VKI	von Karman Institute for Fluid Dynamics (Rhode-St-Genese, Belgium)

List of Symbols

<u>Symbol</u>	<u>Description</u>	<u>Units</u>
A	nozzle area	in ²
A _e	nozzle exit area	in ²
A _{SI}	nozzle area at secondary injection ports in diverging section	in ²
A _t	nozzle throat area	in ²
C ₁	Green/McCullough prediction model coefficient	*
C ₂	Green/McCullough prediction model constant	*
D _h	hydraulic diameter	in
f _R	response frequency for vectoring nozzle flow to switch direction	Hz
F _A	nozzle axial force	lbf
F _S	nozzle side force	lbf
F _T	nozzle total force	lbf
G _M	side force momentum gain	*
I _{sp}	specific impulse	s
L	length along a flat plate	in
m _i , m _s	secondary injection mass flow rate	lbm/s
m _p	primary mass flow rate	lbm/s
M _s	Mach number at flow separation	*
M ₁	Mach number upstream of an oblique shock	*

* non-dimensional quantity

M_2	Mach number downstream of an oblique shock	*
M_∞	Mach number of primary flow at secondary flow location	*
P_a	ambient static pressure	psia, bar
P_e	nozzle exit static pressure	psia, bar
P_1	static pressure upstream of an oblique shock	psia, bar
P_2	static pressure downstream of an oblique shock	psia, bar
P_{t1}	total pressure upstream of an oblique shock	psia, bar
P_{t2}	total pressure downstream of an oblique shock	psia, bar
ΔP_1	difference between secondary supply and exit static pressure	psia, bar
Re_{D_h}	hydraulic diameter-based Reynolds number	*
Re_L	length-based Reynolds number	*
R_M	secondary flow momentum to primary flow momentum ratio	*
t_A	delay time for secondary flow solenoid valve to open or close	ms
t_B	delay time for secondary supply line pressure to increase to steady state	ms
t_R	response time for vectored nozzle flow to switch direction	ms
T	static temperature	$^{\circ}R$
T_{t1}	total temperature of secondary flow	$^{\circ}R$

* non-dimensional quantity

$T_{t\infty}$	total temperature of primary flow at secondary flow port	$^{\circ}\text{R}$
u_{∞}	primary flow velocity for Reynolds number calculation	fps
V_e	nozzle flow exit velocity	fps
V_{ex}	effective primary exhaust velocity to vacuum	fps
V_i	secondary flow exhaust velocity	fps
V_{∞}	primary flow velocity at secondary flow port	fps
w_i	secondary injection weight flow rate	lbf/s
w_p	primary weight flow rate	lbf/s
W_t	nozzle throat width	in
x	distance from nozzle throat along nozzle centerline axis	in
x_s	distance where flow initially separates in the nozzle (measured from throat along nozzle centerline axis)	in
x/L	distance from nozzle throat along nozzle centerline axis normalized by length from nozzle throat to exit along same axis	*
α	angle between the secondary flow and primary flow axes	deg
α	nozzle half angle of divergence	deg
β	angle between a line normal to the nozzle wall at the secondary port and the primary axis	deg
β	oblique shock angle measured from flow turning angle	deg

* non-dimensional quantity

δ	flow turning direction due to oblique shock	deg
δ_t	turbulent boundary layer thickness	in
δ_1	turbulent displacement thickness	in
δ_2	turbulent momentum thickness	in
γ	ratio of specific heats	*
η_{SL}	total pressure ratio due to shock losses in nozzle	*
λ	loss coefficient for the radial divergence of streamlines in a nozzle	*
ν	kinematic viscosity	ft ² /s
σ	energy coefficient for Broadwell force ratio equation	*

* non-dimensional quantity

Abstract

An experimental investigation of two-dimensional confined jet thrust vector control nozzles was performed. Thrust vector control was accomplished by using secondary flow injection in the divergent section of the nozzle. Schlieren photographs and video tapes were used to study flow separation and internal shock structures. Nozzle performance parameters were determined for nozzle flow with and without secondary flows. These parameters included nozzle forces, vector angles, thrust efficiencies, and flow switching response times. Vector angles as great as 18 degrees with thrust efficiencies of 0.79 were measured. Several confined jet nozzles with variations in secondary flow port designs were tested and results were compared to each other. Converging-diverging nozzles of similar design to the confined jet nozzles were also tested and results were compared to the confined jet nozzle results.

Existing prediction models for nozzle side to axial force ratio were evaluated. A model for nozzle total forces based on shock losses that predicted values very close to actual results was developed.

TWO-DIMENSIONAL CONFINED JET THRUST VECTOR CONTROL:
OPERATING MECHANISMS AND PERFORMANCE

I. Introduction

Background

An important part of any airborne or space vehicle is its attitude and guidance control system. Most aircraft and missiles use aerodynamic surfaces to adjust their attitude and direction of flight. This type of control varies greatly with the speed and altitude of the vehicle and has the disadvantage of added drag. Changing the direction of a vehicle's thrust is a method of augmenting or even replacing aerodynamic control surfaces.

Possible methods of thrust vector control (TVC) for rocket engines can be divided into three groups. Group 1 are those nozzles which use direct mechanical interference with the exhaust gases such as jet vanes, spoilers, and jetavators. Group 2 systems require the movement of the whole thrust-producing apparatus such as swivel or gimballed nozzles. Both of these groups require high-temperature materials and elaborate seals. Group 3 systems use nonmechanical interference with exhaust gases such as gas bleeding or the secondary injection of gas into the nozzle

(4:2). Gas bleeding is simply the release of combustion gases through a channel at some angle to the centerline axis of the nozzle. Its effective side force is therefore limited to the momentum of the gas bleed flow. The secondary injection of gas into the nozzle produces a side force that is a combination of the secondary jet momentum and the interaction (dynamic and chemical) of the secondary jet with the primary axial flow (2:214). This interaction allows the side force to be greater than the momentum of the secondary jet.

Secondary Injection Thrust Vector Control (SITVC)

Boundary Layer Thrust Vector Control (BLTVC) is one type of SITVC. It uses an over-expanded, converging-diverging nozzle with control ports in the diverging section to allow ambient air as a secondary gas into the nozzle. When a port is opened, the pressure rise due to the ambient air augments the existing separation region in the nozzle. This causes the primary flow path to attach to the opposite wall where the pressure is lower. Figure 1 illustrates this flow mechanism. This type of TVC requires that the ambient pressure be greater than the pressure at the secondary port in the nozzle. BLTVC systems will therefore have altitude limitations to their operational envelope (8:1,2).

Confined Jet Thrust Vector Control (CJTVC) is a type of SITVC that may not have the altitude restrictions of BLTVC. It uses a reconverging section on a nozzle to contain the

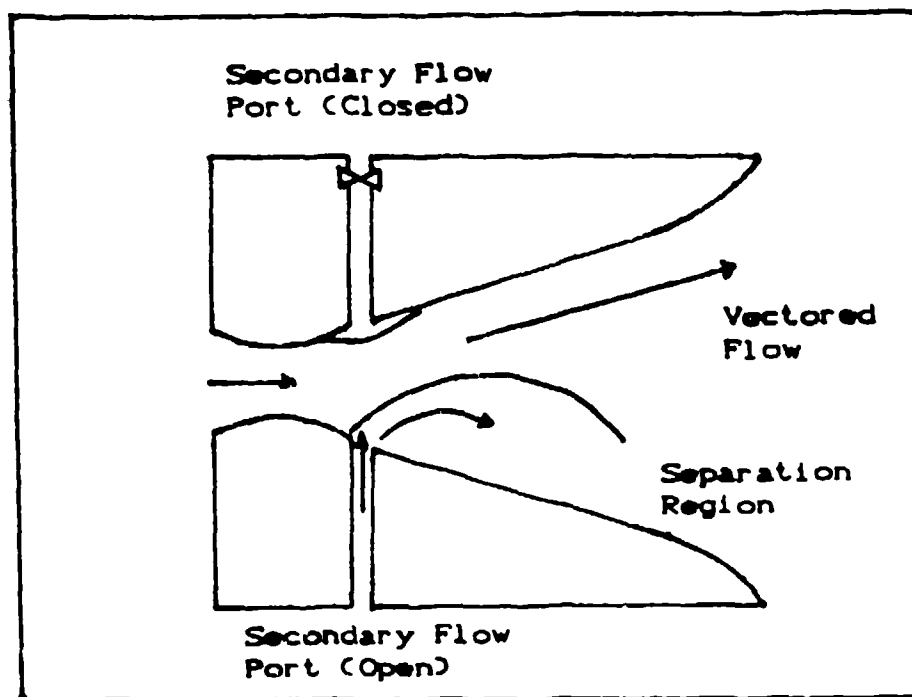


Fig 1 Boundary Layer Thrust Vector Control
(BLTVC) System

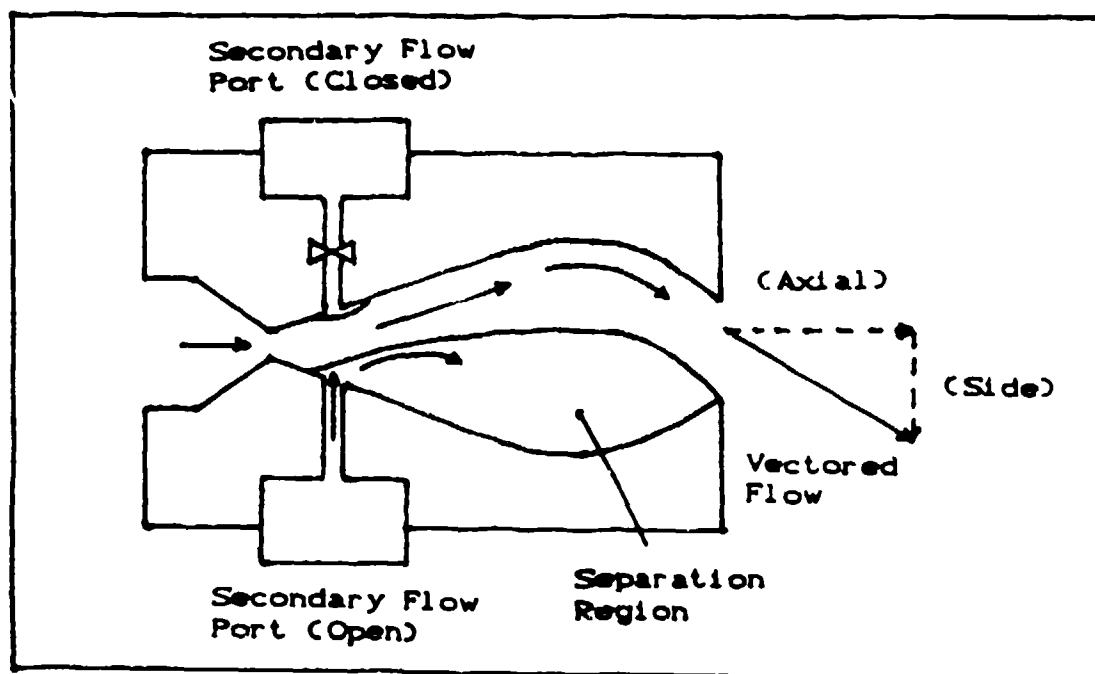


Fig 2 Confined Jet Thrust Vector Control (CJTVC) System

separated region, thereby insulating it from ambient conditions. Secondary flow enters the nozzle from some source and deflects the axial flow to the opposite wall, where it attaches. Figure 2 illustrates a typical CJTVC system. Besides its increased operational envelope, CJTVC usually has relatively small secondary mass flow rates. This means that the secondary flow supply storage requirement is relatively small and can be readily packaged for typical rocket TVC applications. In addition to the compressed secondary gas supply, small, fast-responding control valves are required for the system (8:8).

Previous CJTVC Work

Several CJTVC designs have been constructed and tested at the Air Force Institute of Technology (AFIT). Porzio designed and tested an axisymmetric CJTVC nozzle (12:7) variations of which other students tested. Cates designed and tested several two-dimensional CJTVC nozzle configurations, only one of which could be consistently vectored at his test conditions (5:47). Talda improved Cates design and developed several CJTVC configurations which could consistently vector. Talda's nozzle has efficiencies as high as 85%, with ± 20 degrees deflections with vectoring response times as low as 50 ms (16:104).

Goal and Objectives

The goal of this thesis is to continue the previous work in the design and testing of two-dimensional CJTVC nozzles. Emphasis is placed on studying existing designs to determine their thrust vector mechanisms in hopes of developing nozzle design optimization parameters. Specific objectives for reaching this goal are:

1. Use flow visualization techniques to determine flow separation points within the nozzles.
2. Use flow visualization techniques to study shock development and interaction within the nozzles.
3. Measure and analyze nozzle performance characteristics at varying operating conditions. These performance characteristics consist of side and axial force measurements, flow vector angles, nozzle thrust efficiencies, and side momentum gain. The momentum gain is the ratio of the measured side force to the momentum of the secondary flow. Operating conditions will be varied by changing the nozzle pressure ratio (NPR) and the secondary to primary mass flow ratio (MFR). NPR is the ratio of primary flow total pressure to ambient pressure. MFR is the ratio of the secondary mass flow rate to the primary mass flow rate.
4. Study nozzle vector switching characteristics, concentrating on determining switching response time and stable operating conditions. Switching response time is the time it takes for primary flow to vector measured from the

point when secondary flow is introduced.

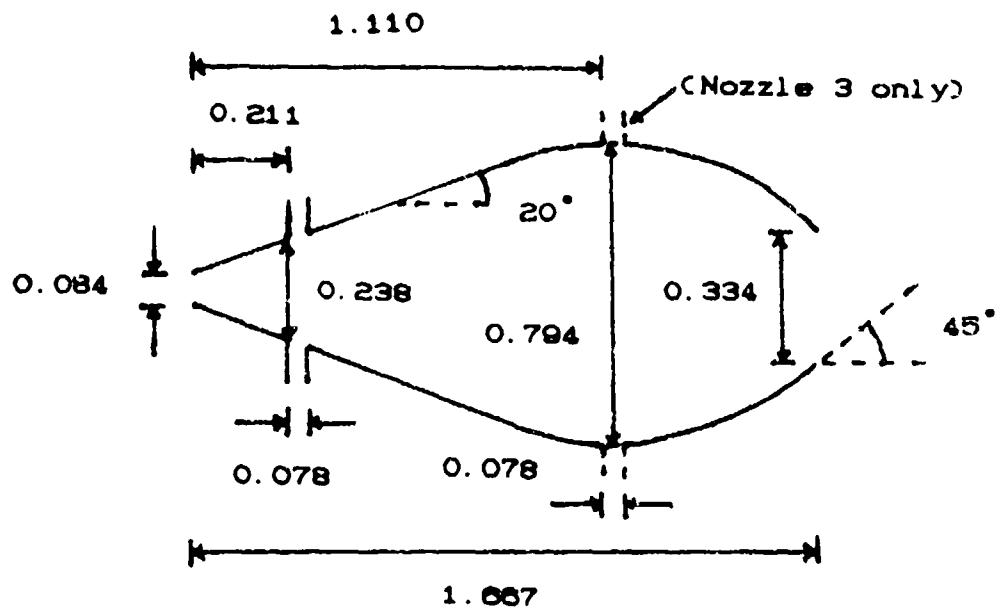
5. Develop prediction models for nozzle performance, particularly, a model that can predict the losses which occur in the nozzle. Evaluate several existing SITVC prediction models.

II. Experimental Apparatus

Nozzle Design

Talda's LM configuration had the best vectoring performance of all the two-dimensional CJTVC nozzles reviewed. It is a modification to Cates best performance design where sharp linear walls are replaced by smooth curved walls in the reconverging section (16:12-16.32). Therefore, it was used as the basic nozzle design for this study. Talda's LM nozzle was tested at a maximum nozzle pressure ratio (the ratio of primary flow total pressure to ambient static pressure) of approximately 15. Typical solid rockets have nozzle pressure ratios (NPR) ranging from 50-1000 (7:40). Testing a nozzle at these higher NPRs requires either extremely high primary pressures or extremely low back pressures. For safety and convenience, this study used reduced back pressure chambers to increase test NPRs. A one-third scale (linear dimensions) version of Talda's design was used as the basis for all nozzles tested (16:13). The reduced size nozzle was chosen in order to reduce mass flow rate and thereby decrease the evacuation requirements of the reduced back pressure chambers. Figure 3 illustrates the nozzle design and contains relevant nozzle geometry data.

A prototype scaled-down nozzle was constructed and tested in a blowdown wind tunnel. These tests confirmed the vectoring ability of the nozzle and provided some flow



Height of
Nozzle Channel = 0.25 in

$$\frac{A_e}{A_t} = 4.0$$

$$A_t = 0.021 \text{ in}^2$$

$$A_{SI} = 0.060 \text{ in}^2$$

$$A_{MAX} = 0.199 \text{ in}^2$$

$$A_e = 0.084 \text{ in}^2$$

Fig 3 Basic Test Nozzle Design and Geometry Data

(All dimensions given in inches)

visualization information. Four variations of the Talda design were manufactured for testing:

Nozzle 0: Smooth wall configurations (no secondary ports)

Nozzle 1: Two secondary ports with flow perpendicular to primary flow axis; ports located three throat widths from nozzle throat

Nozzle 2: Same as nozzle 1 except secondary flow is perpendicular to nozzle wall at secondary port location

Nozzle 3: Four SI ports with flow perpendicular to primary flow axis; two ports located three throat widths from nozzle throat; two ports located at maximum nozzle area.

In addition to these four CJTVC nozzles, two converging-diverging configurations were tested.

Nozzle 4: Exit to throat area ratio of 9.5 (based on the maximum area to throat area ratio of the Talda nozzle design)

Nozzle 5: Exit to throat area ratio of 4.0 (based on the exit to throat area ratio of the Talda nozzle design)

Figure 4 provides a comparison among all six test nozzles.

Test Model Design

All previous CJTVC studies at AFIT tested the nozzles using static test stands with the nozzles attached to a force measurement load cell. Since installed performance of

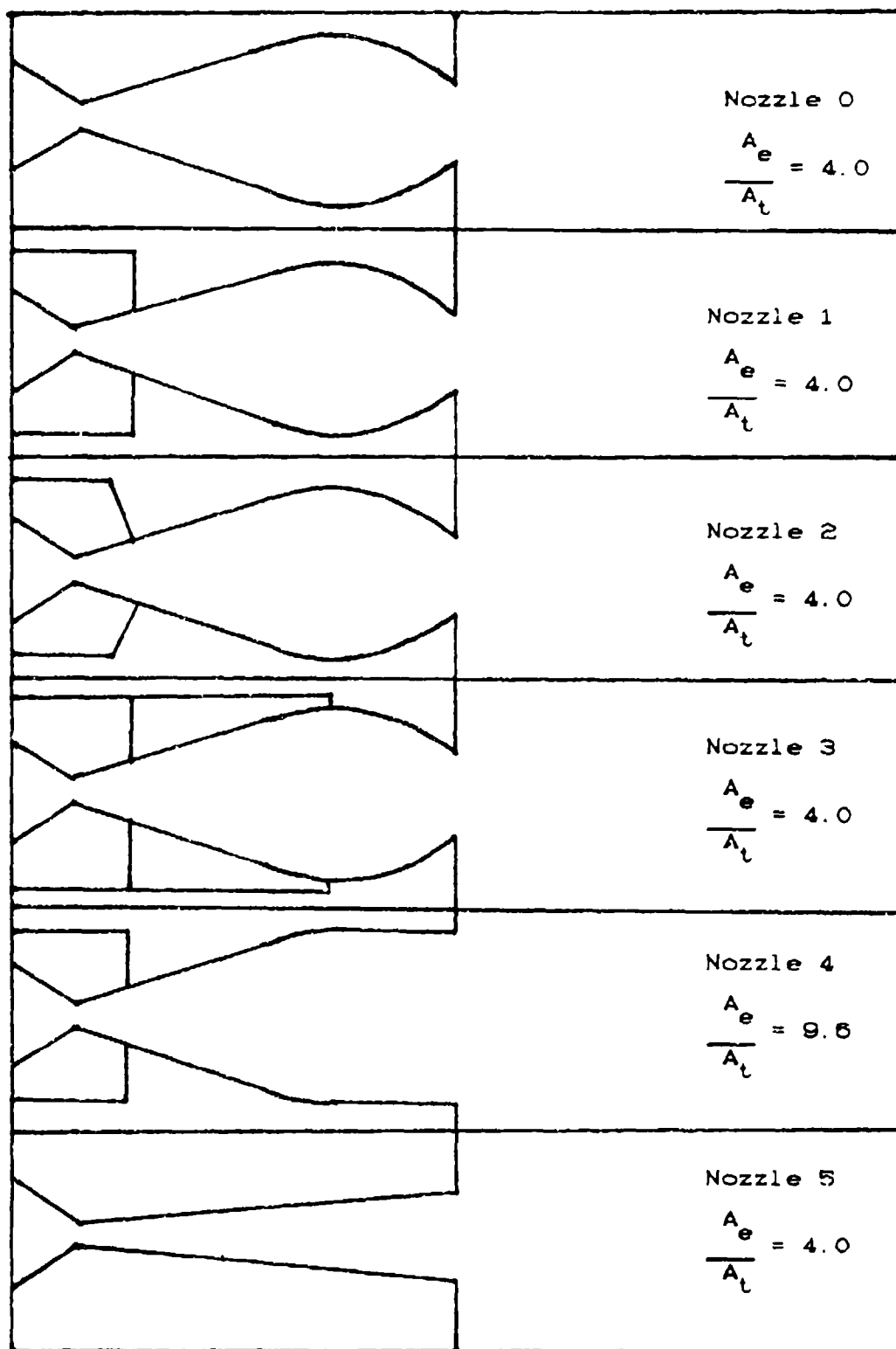


Fig 4 Test Nozzle Configurations

a TVC nozzle is important in evaluating its practical applications, a wind tunnel model capable of supporting the test nozzles was designed, fabricated, and tested. Figure 5 illustrates this design. The design point of the model was to operate in a Mach 2.2 wind tunnel. The main components of the model are listed in the following paragraphs.

1. Cylindrical main body with a 30° half-angle nose cone to properly deflect oblique shocks away from the test area. Body is hollow with enough space to accommodate a model S scanivalve (48 pressure ports).

2. Interchangeable rear section of main body that can accommodate either a nozzle test assembly with static pressure measurement ports or a nozzle test assembly for schlieren photographs. Because its cross section does not match the cylindrical main body, the schlieren assembly cannot be used in the supersonic free stream.

3. Nozzle test assembly with 36 static pressure measurement ports. The pressures at these ports were measured using a scanivalve connected to an ENDEVCO differential pressure transducer. Figure 6 shows the components of the assembly, including the distribution of the pressure measurement ports across the nozzle.

4. A rearward-swept support strut that interfaces to a six-component force balance. Its cross section is a modified diamond airfoil with a 16° half-angle leading and trailing edge to properly deflect oblique shocks away from the test area.

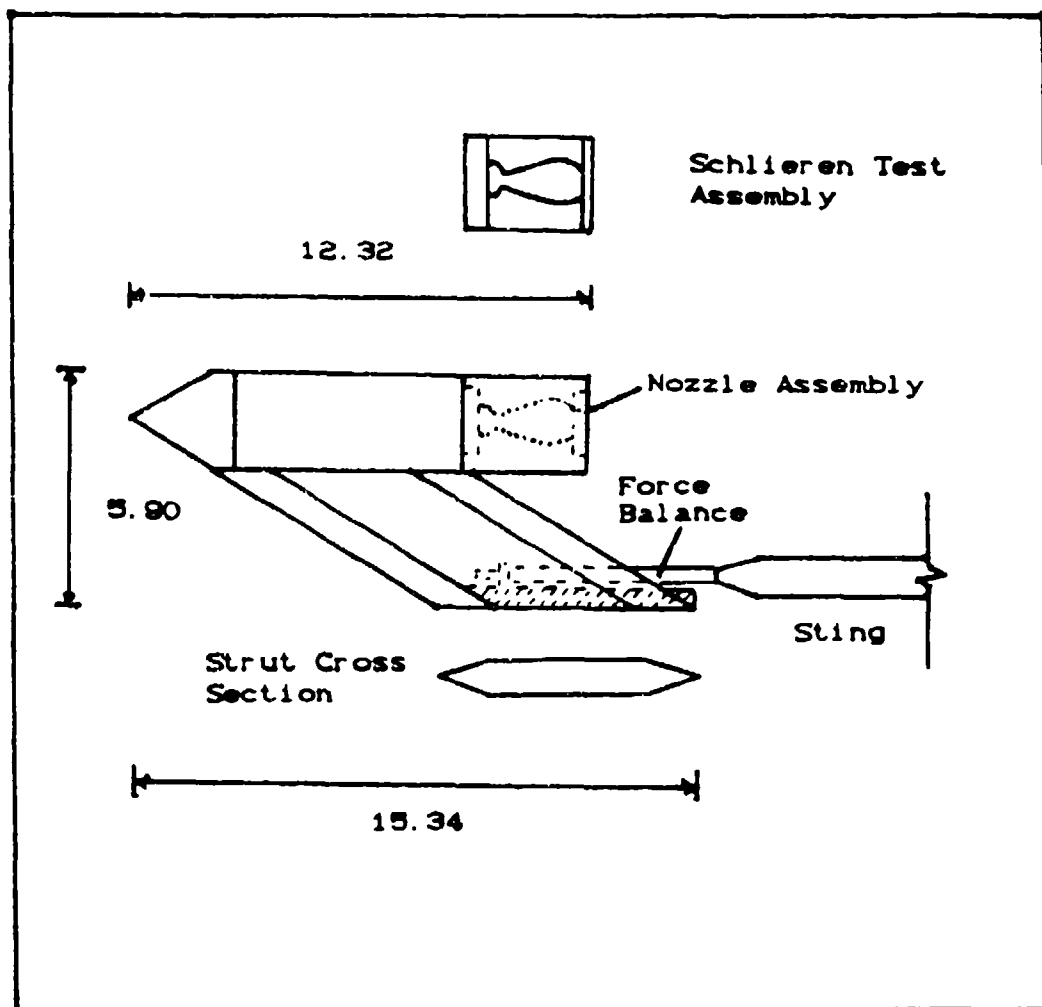


Fig 5 Wind Tunnel Model
(All dimensions in inches)

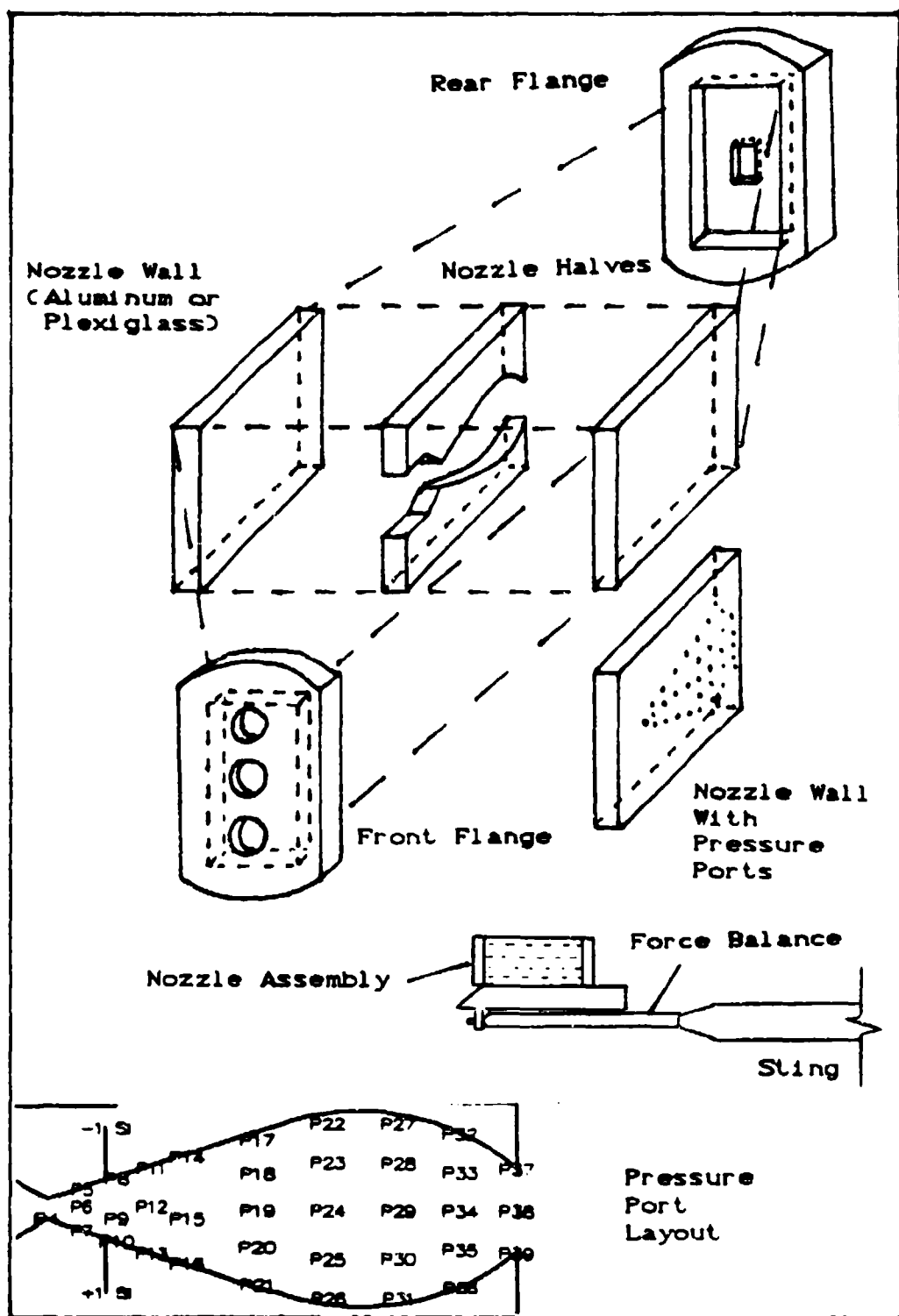


Fig 6 Nozzle Test Assembly

Appendix A contains more detailed drawings and dimensions of the test model.

Test Facilities

The primary test facility for this study was the S-1 supersonic/transonic wind tunnel located at the von Karman Institute of Fluid Dynamics (VKI), Rhode-St-Genese, Belgium. The S-1 wind tunnel is a continuous closed circuit facility driven by a 615 kW axial flow compressor. A 40 cm x 40 cm test section was used for testing where supersonic flows of Mach 2.0 or 2.25 and transonic flows between Mach 0.4 and 1.05 are possible. The test section contains a three-degree-of-freedom traversing mechanism for model support as well as variable incident mechanism. The tunnel is also equipped with a schlieren photograph system (18:23).

Data acquisition was performed using a variety of instruments. A summary of the main subsystems used in data acquisition follows:

1. Commodore Extension Interface (CEI) data acquisition system containing a 12-bit A/D converter with 16 single-ended input channels with a maximum conversion rate of 25 kHz. The CEI interfaced to a 8032 PET-Commodore computer which executed the appropriate data acquisition software.
2. VKI 6-component force balance with its supporting amplifiers, filters, wheatstone bridges, and CEI connection. Only the two normal force channels and the axial force

channel were used. Design details of the balance are included in Appendix A.

3. Model 48S3 scanivalve with its supporting DC motor drive, power supply, position indicator, and CEI connection.

4. ENDEVCO Model 8510B-50 piezoresistive pressure transducer with its supporting amplifier/filter. It is a differential pressure transducer with a range of 0-50 psig.

5. TEKTRONIX Model 2430 digital oscilloscope capable of simultaneous acquisition of two input channels. It has a maximum digitizing rate of 100 megasamples per second and a real-time useful storage bandwidth of 40 MHz.

6. Hewlett-Packard Model 3582A spectrum analyzer capable of single or dual channel sampling and digitizing.

7. Solenoid control panel for secondary injection valves capable of sending an acquisition trigger signal simultaneous to the valve open/close command to either the digital oscilloscope or spectrum analyzer.

8. ROTAMETER Model G1.1000 mass flow meter. Primary flow rates were measured using a steel float while secondary flow rates were measured using a plastic float.

Prior to testing at VKI, the wind tunnel model was static tested at facilities in building 454 of Wright Patterson AFB, Ohio. These were the same facilities used by Cates and Talda for their CJTVC nozzles. The tests confirmed the nozzles vectoring capability and structural integrity prior to shipment to VKI. Appendix A includes a drawing of the VKI tunnel and how the instrumentation was

integrated into it.

The test model met the weight and cross sectional area blockage requirements of the VKI tunnel. However, when placed on the tunnel sting, the model created a pitching moment at operating conditions that would damage the force balance. Therefore, force measurements were not possible with the wind tunnel model. Using a solid steel "dummy" balance (no strain gages), the model was able to support the schlieren apparatus for flow visualization tests. Force measurements were taken by mounting the nozzle assembly directly to the force balance as previously illustrated in Fig 6. Because of this arrangement, force measurements taken in a supersonic freestream were not possible.

III. Nozzle Operating Mechanisms Results

Separation Studies (no secondary injection)

CJTVC nozzles depend on the primary flow separating from one wall and becoming attached to the opposite wall for flow vectoring. Therefore, it is important to know where the flow will inherently separate in the nozzle. The distance along the nozzle axis to where the flow separates from the walls for nozzles 0,1,3 and 4 was measured from enlarged schlieren photographs taken at increasing NPRs with no secondary flow. This distance to the point of flow separation is labeled x_s . Nozzle 2 was not considered since its configuration with no secondary flow is identical to nozzle 1. Figures 7 through 10 are composites of the schlieren photographs used to measure the values of x_s . They illustrate the nozzle flow structure at increasing values of NPR. The clear walls required for the schlieren nozzle assembly were made of 0.25 inch plexiglass, not optical glass. Therefore, some inherent refraction of the images was evident when the enlarged photographs were examined, which degraded the accuracy of the measurements.

Figure 11 is a summary of all x_s values measured. The nozzle-normalized length to flow separation is simply x_s/L , where L is the length from the nozzle throat to the nozzle exit along the centerline axis. The two horizontal lines indicate the location of the first secondary port (not

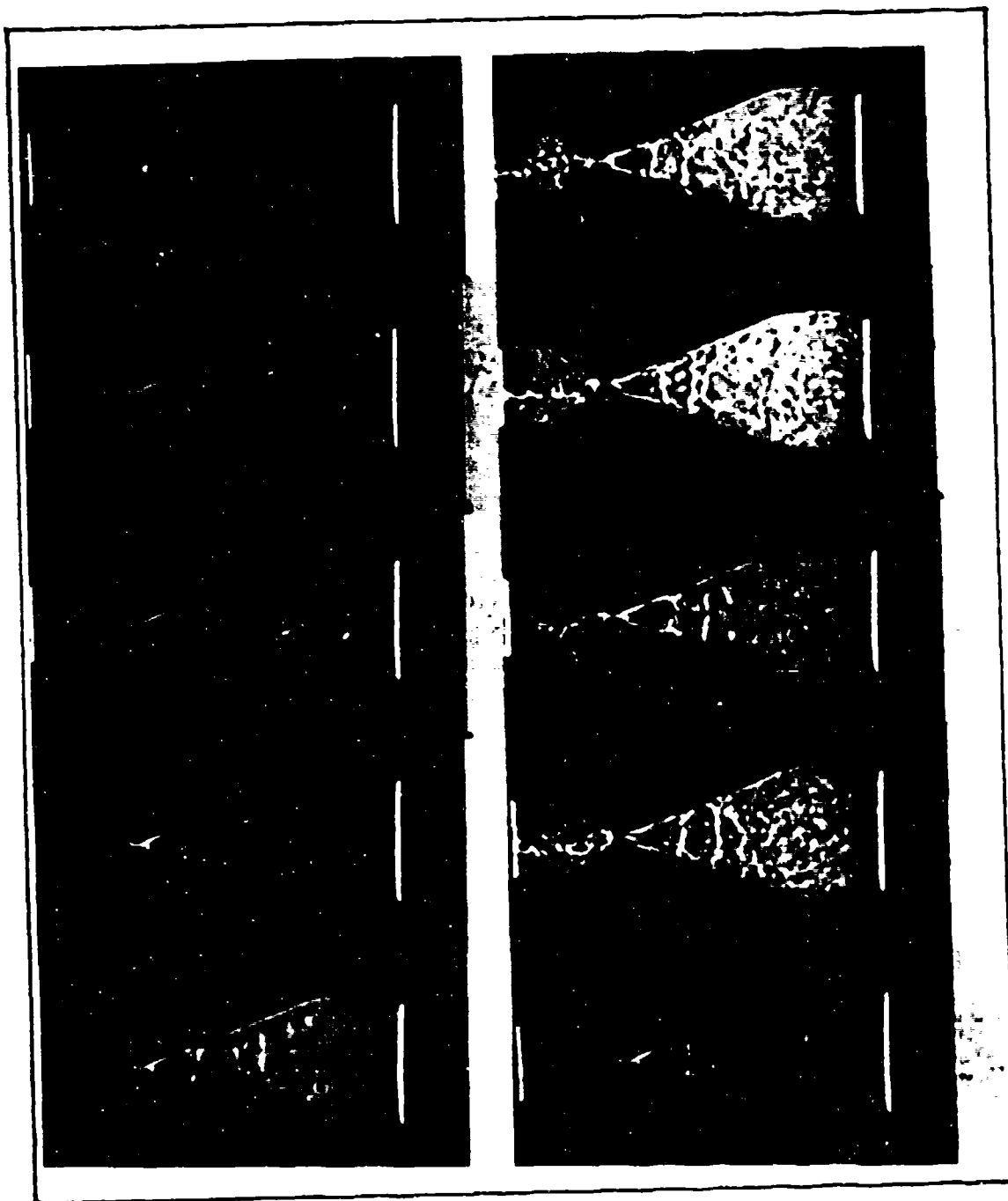


Fig 7 Nozzle O Separation Schlieren Photographs
(Nozzle pressure ratios in order from upper left hand to
lower right hand photograph: 10.3, 11.6, 13.0, 14.2, 15.5,
17.8, 19.7, 24.6, 29.6, 34.5)

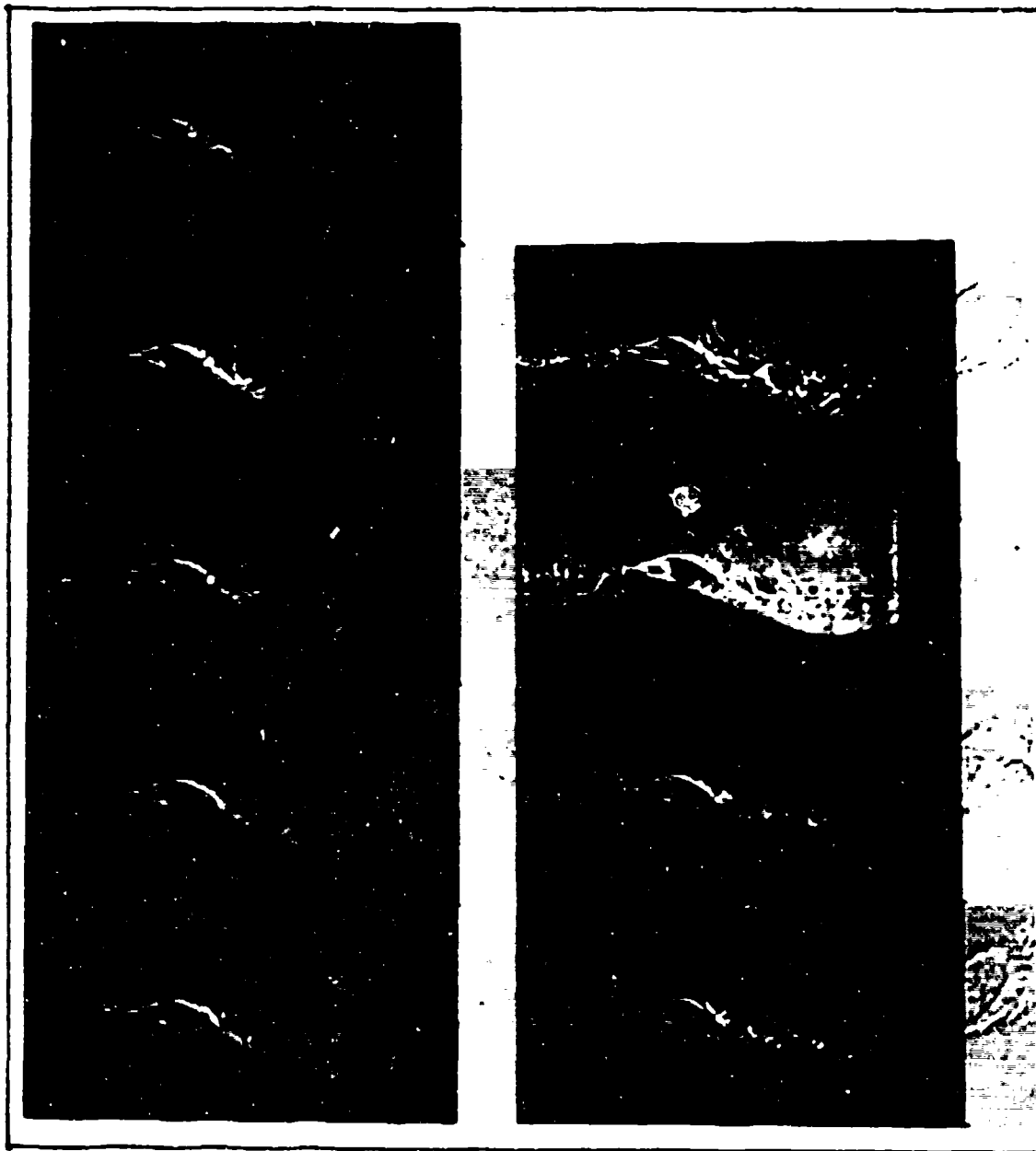


Fig 8 Nozzle 1 Separation Schlieren Photographs
(Nozzle pressure ratios in order from upper left hand to
lower right hand photograph: 10.3, 12.0, 14.7, 16.1,
18.6, 20.8, 26.3, 31.8, 38.2)

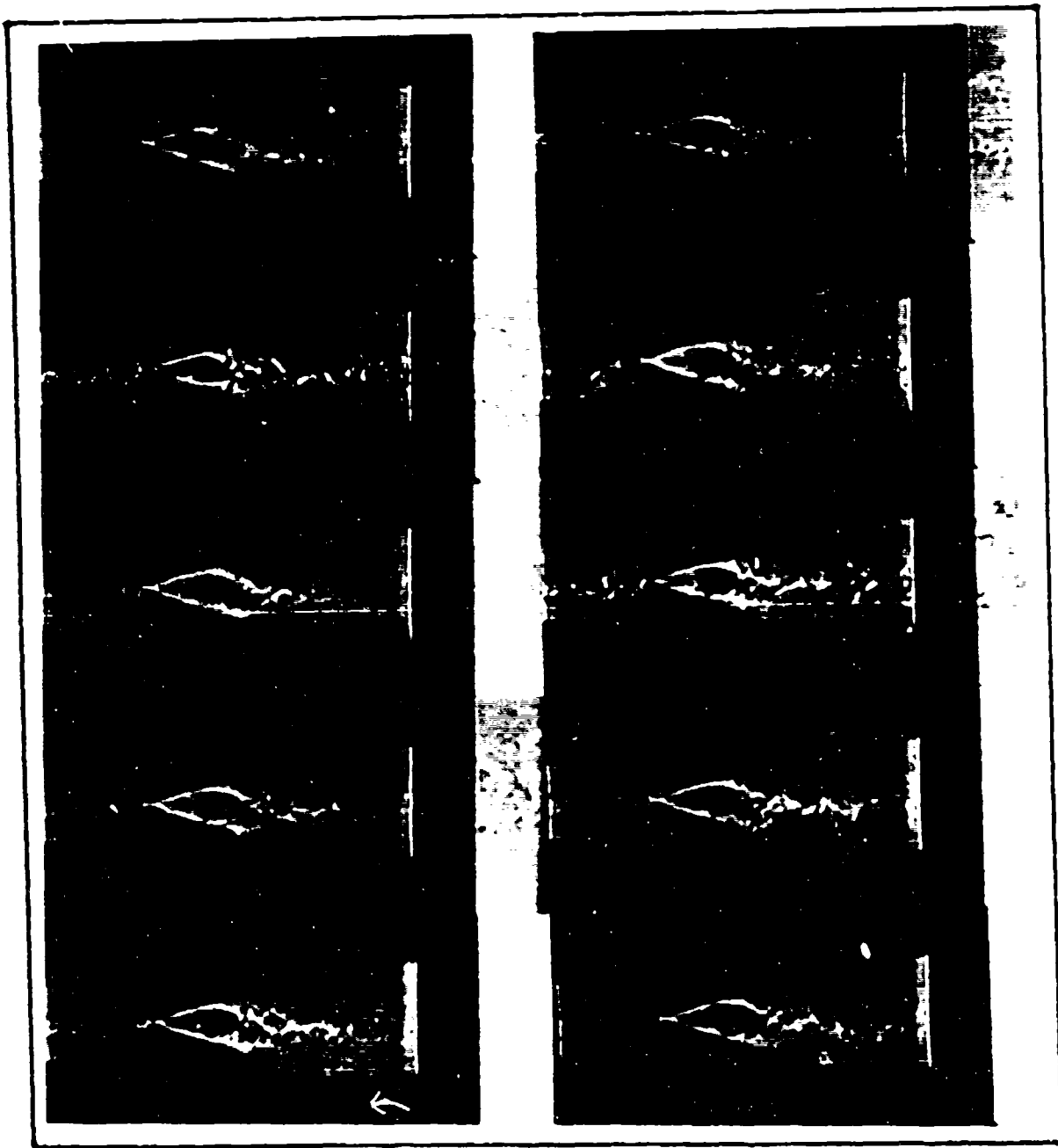


Fig 9 Nozzle 3 Separation Schlieren Photographs
(Nozzle pressure ratios in order from upper left hand to
lower right hand photograph: 15.4, 17.2, 19.0, 21.1,
22.7, 25.6, 28.4, 35.5, 42.5, 49.6)

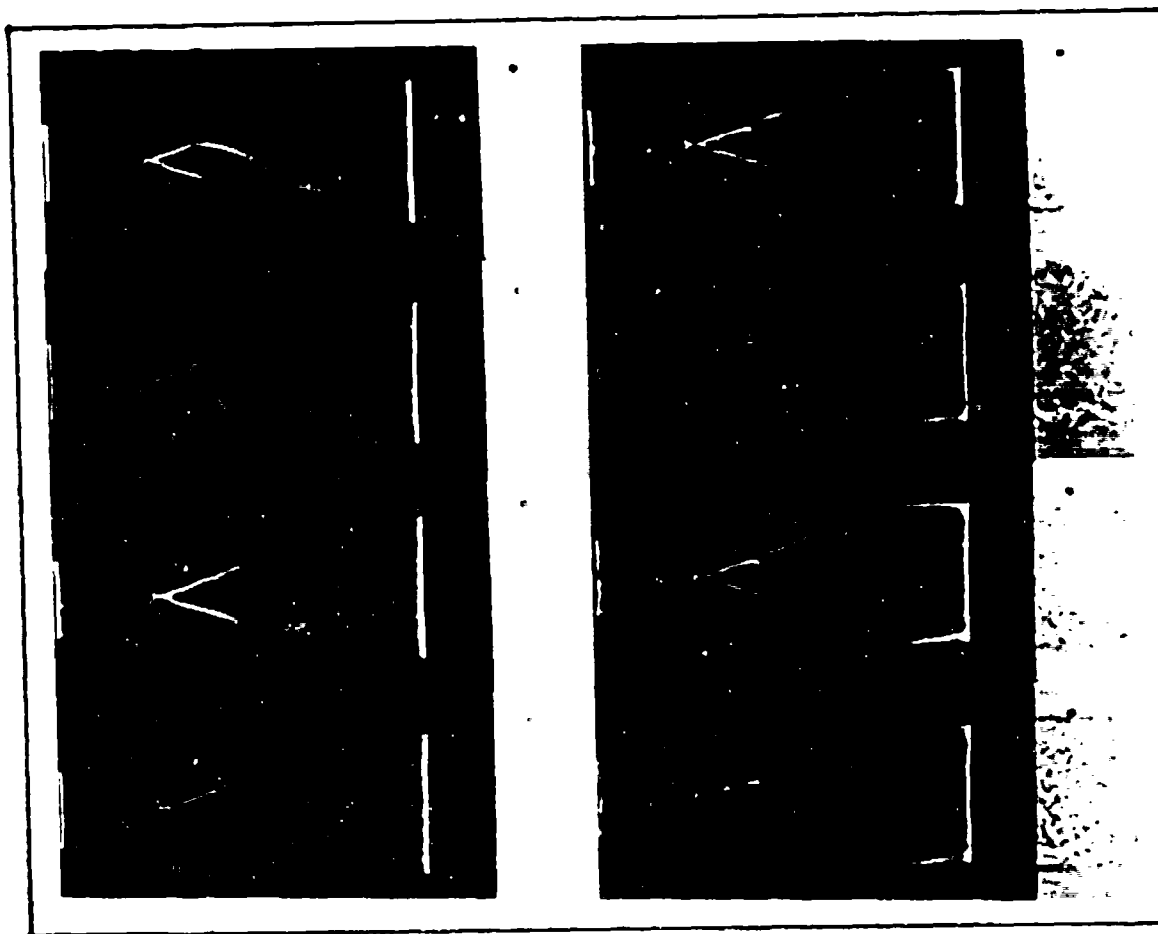


Fig 10 Nozzle 4 Separation Schlieren Photographs
(Nozzle pressure ratios in order from upper left hand to
lower right hand photograph: 19.7, 21.4, 23.0, 24.6,
32.5, 40.3, 48.1, 55.7)

CJTVC NOZZLE SEPARATION TESTS

SUMMARY OF NORMALIZED VALUES

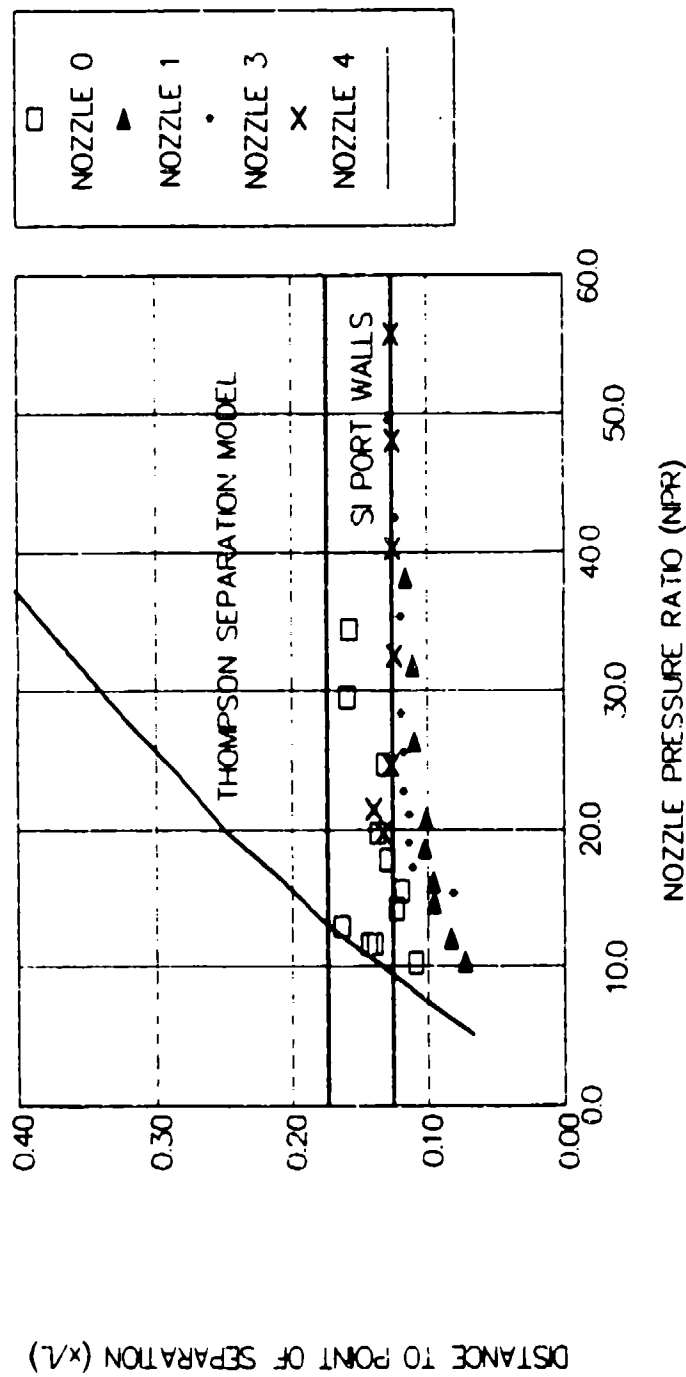


Fig 11 Summary of Normalized Separation
Lengths in Test Nozzles

applicable for nozzle 0). The solid line labeled "Thompson Separation Model" identifies separation points predicted by Thompson's model for separation in nozzles caused by adverse pressure gradients (17:1-8). Appendix B contains the appropriate equations and sample calculations. The distance to points of flow separation in nozzles 1, 3, and 4 with secondary ports tend to be very close to the secondary ports. Nozzle 0, which has no secondary ports, has x_s/L values slightly higher than those nozzles with secondary ports.

The proximity of x_s/L for nozzles with secondary ports to the beginning of these secondary ports indicates that the separation may be shock-induced. If the presence of the secondary ports in the flow do cause oblique shocks to form, as the photographs indicate, separation may occur slightly before this shock (2:217). This is consistent with the trends shown in Fig 10, including the divergence of the measured values from the Thompson model (which only deals with separation due to adverse pressure gradients). This divergence is consistent with Cate's conclusions concerning the Thompson model (5:47).

Nozzle 0 appears to have a combination of separation mechanisms. At NPRs up to approximately 13, the separation follows the Thompson model and therefore may be caused by adverse pressure gradient separation. At higher NPRs, normal shocks start to appear in the nozzle cavity and the separation appears to be caused by these shocks. Further

details of shock structures are discussed later.

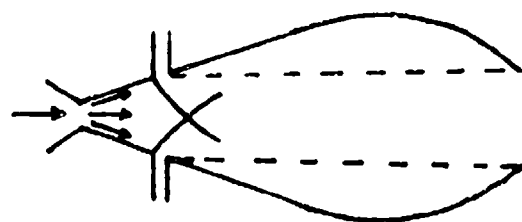
Having flow separation induced by the presence of the secondary ports is advantageous since then the point of separation will always be known. Also, it ensures that the secondary flow will be introduced into the separation region of the flow which is important for vectored flow (8:2).

The location of the point of separation may also be influenced by the flow turning requirements of the nozzle. The ratio of nozzle exit area to the area at the secondary port location is 1.42 for all CJTVC test nozzles. The oblique shocks (which causes separation) observed may be required to turn the flow towards the nozzle exit as Fig 12 illustrates. Further discussion of nozzle shock structures and flow turning requirements follow.

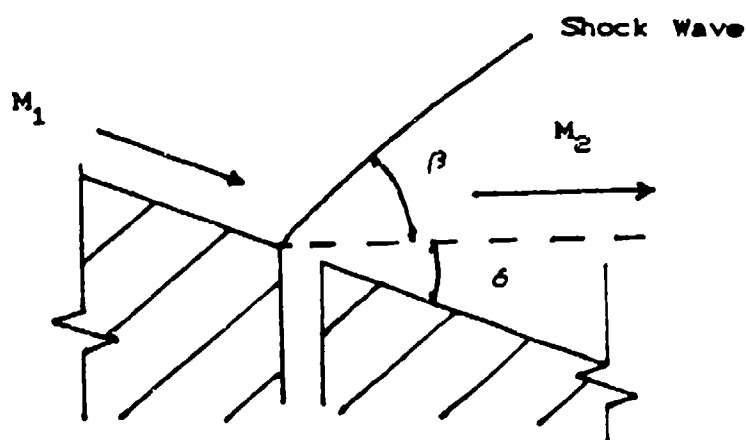
Shock Structures (no secondary injection)

The internal shock structures are different for each nozzle tested. By studying these structures, considerable insight is gained concerning the primary flow in the nozzles. The following paragraphs summarize the major shock and flow characteristics of each nozzle.

At low NPR, oblique shocks can be seen in the diverging portion of nozzle 0, as shown in Fig 7. These oblique shocks may be caused by the adverse pressure gradient separation (15:54). As the NPR increased, either normal shocks or Mach reflections are clearly evident. These may be caused by either an intersection of the oblique shocks



$$\frac{A_e}{A_{SI}} = 1.42$$



M_1 = Mach number before oblique shock

M_2 = Mach number after oblique shock

δ = flow turning angle

β = oblique shock angle with respect to δ

$(\beta + \delta)$ = oblique shock angle with respect to wall

Fig 12 Oblique Shock Flow Turning in Nozzles

for the Mach reflection case (6:481), or by normal shock formation due to increased over expansion (14:135). Both mechanisms will provide the observed axial flow as Fig 13 illustrates. Oblique shocks mach reflections turn the flow towards the nozzle exit. Normal shock formation will thicken the boundary layer and increase the separation region to form a path that keeps the primary flow axial. Mach line development will include slip lines that may also define the primary flow path (14:557,583). Since these shock structures are extremely complicated to analyze, it is impossible within the scope of this study to determine which mechanism causes the observed flow in nozzle 0.

In nozzle 1 (Fig 8), oblique shocks caused by the secondary ports are evident in all cases. These oblique shocks determine the flow turning direction as previously illustrated in Fig 12. Increasing values of the oblique shock angle, β , indicate increasing pressure rises across the shock. Therefore, any difference between oblique shock angles for the upper and lower nozzles walls also means there is a difference in static pressures. These pressure differences cause the separation region behind the upper shock to enlarge and the flow to attach to the lower wall in all cases. This biased flow is consistent with the bistable nature of this nozzle configuration, which will be discussed later.

Nozzle 3 (Fig 9) displays the secondary port-induced oblique shock structure similar to nozzle 1, but has axial

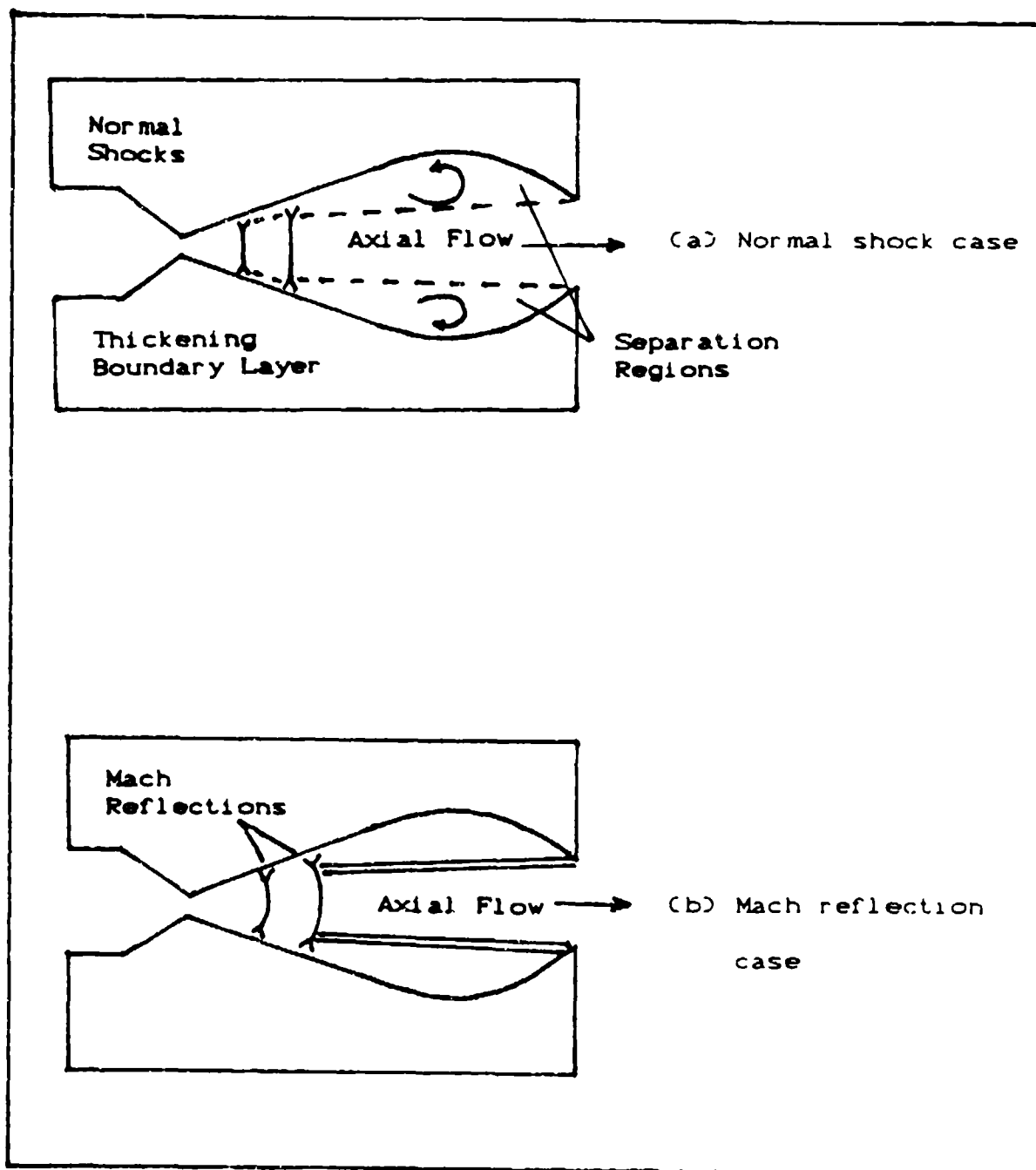


Fig 13 Shock and Flow Structures for Nozzle 0

Primary Flow

flow stability similar to nozzle 0. Figure 14 illustrates why nozzle 3 is not bistable. Part (a) shows the nozzle as it appears in Fig 9. Subsonic separation regions behind the oblique shocks provide a path for the supersonic nozzle flow. If this supersonic flow tries to attach to either nozzle wall, the secondary port located at the nozzle maximum area will induce an oblique shock. Video tape flow visualization results (discussed in detail later) show that these shocks form with or without secondary flow. The shock will include a separated region before and after it (2:217) that will not allow the flow to attach. Therefore, the presence of the additional secondary ports cause nozzle 3 to have stable axial flow.

Nozzle 4 (Fig 10) shows the same oblique shock structure in the diverging section as nozzles 1 and 3. It has stable axial flow like nozzle 3, but for different reasons. Since this nozzle does not have the reconverging section prior to its exit, any separation region caused by shocks will not be entrained as it is in the CJTVC design. At higher NPRs, small separation regions appear just inside the nozzle exit. These may be caused by the reflection of the secondary port-induced oblique shocks as illustrated in Fig 15. At lower NPRs, the shock angle may be of sufficient magnitude to cause the shock to intersect the separation region. At higher NPRs, the shock angle is decreased and the shock reflection is possible.

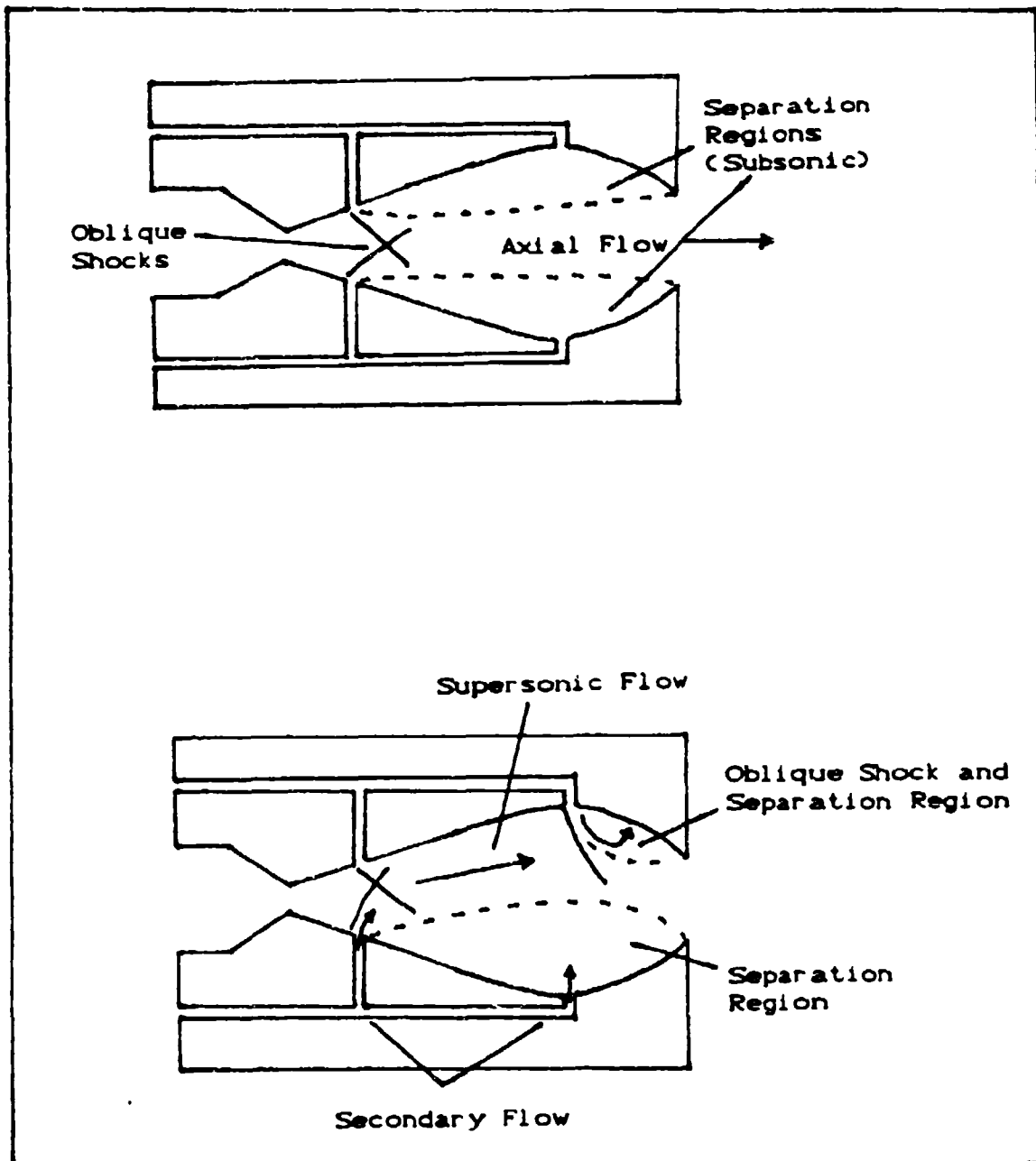


Fig 14 Shock and Flow Structures for Nozzle 3

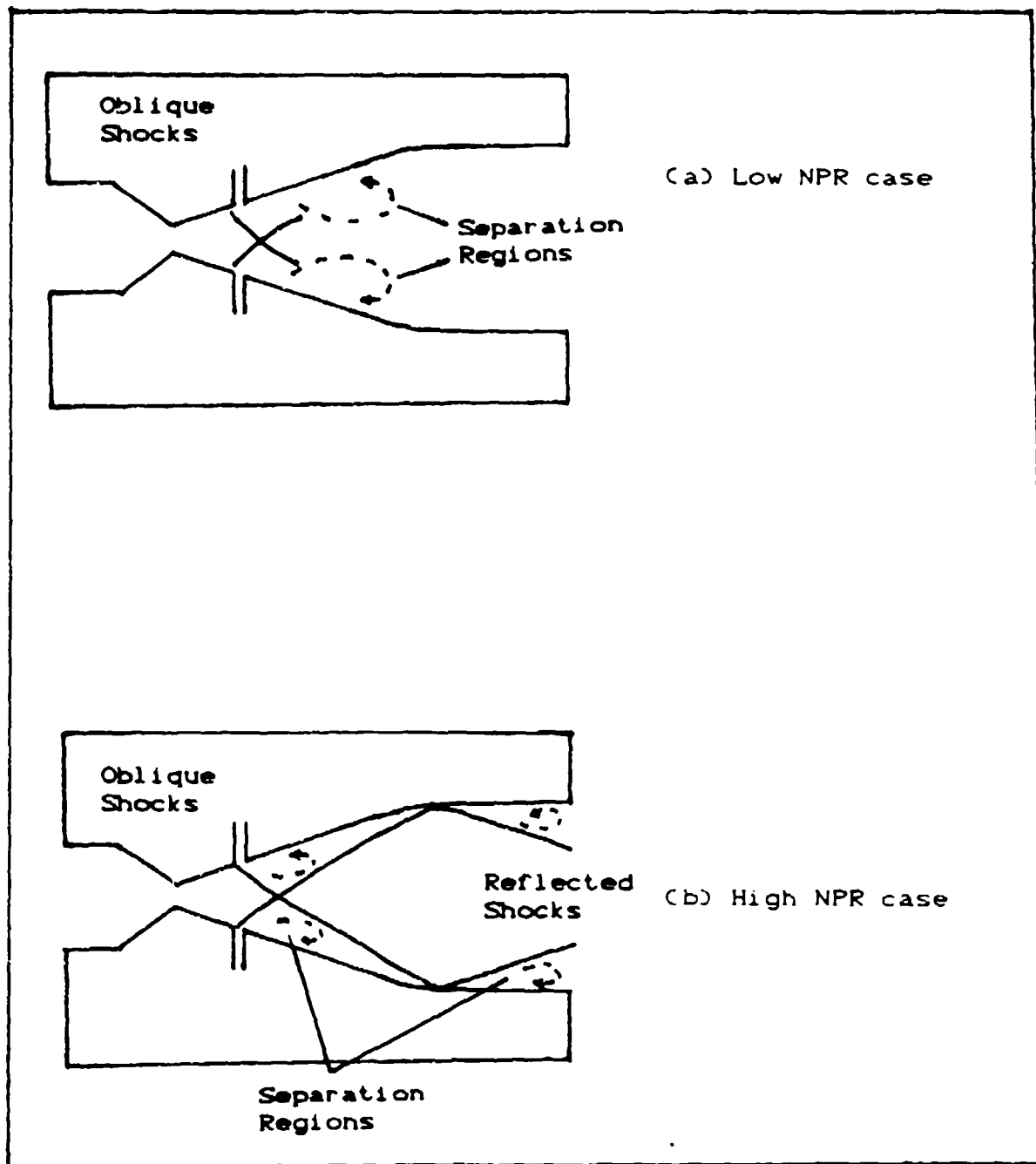


Fig 15 Shock and Flow Structures for Nozzle 4

Flow Visualization Observations

In addition to the separation schlieren photographs, video tapes of schlieren photography were recorded. Approximately two hours of video tape was recorded in the AFIT blowdown wind tunnel which allowed testing at reduced ambient pressure using the prototype nozzle at NPRs between 4 and 23. It had one nozzle half with one port that directed secondary flow perpendicular to the primary flow and one half with a port that directed secondary flow perpendicular to the nozzle wall. An additional 40 minutes of video tape was recorded at the VKI S-1 tunnel using nozzles 0,1,2, and 3 with NPRs between 33 and 41. This was accomplished by focusing a video camera capable of macro photography on the schlieren image formed on a frosted glass plate. Several important observations are summarized below.

The bistable nature of nozzles 1 and 2 was evident from the video tapes. When primary flow was introduced into either nozzle, the flow immediately became biased towards one wall. This bias was more pronounced at lower NPRs where the flow seemed to be more unstable. When secondary flow adequate for vectoring was introduced, the flow immediately attached to the wall opposite to the operating secondary port. In order to produce axial flow, both secondary flows were required.

Figure 16 illustrates shock structures found in the video tapes for vectored and axial flow cases. In the vectored case, the secondary flow raises the pressure behind

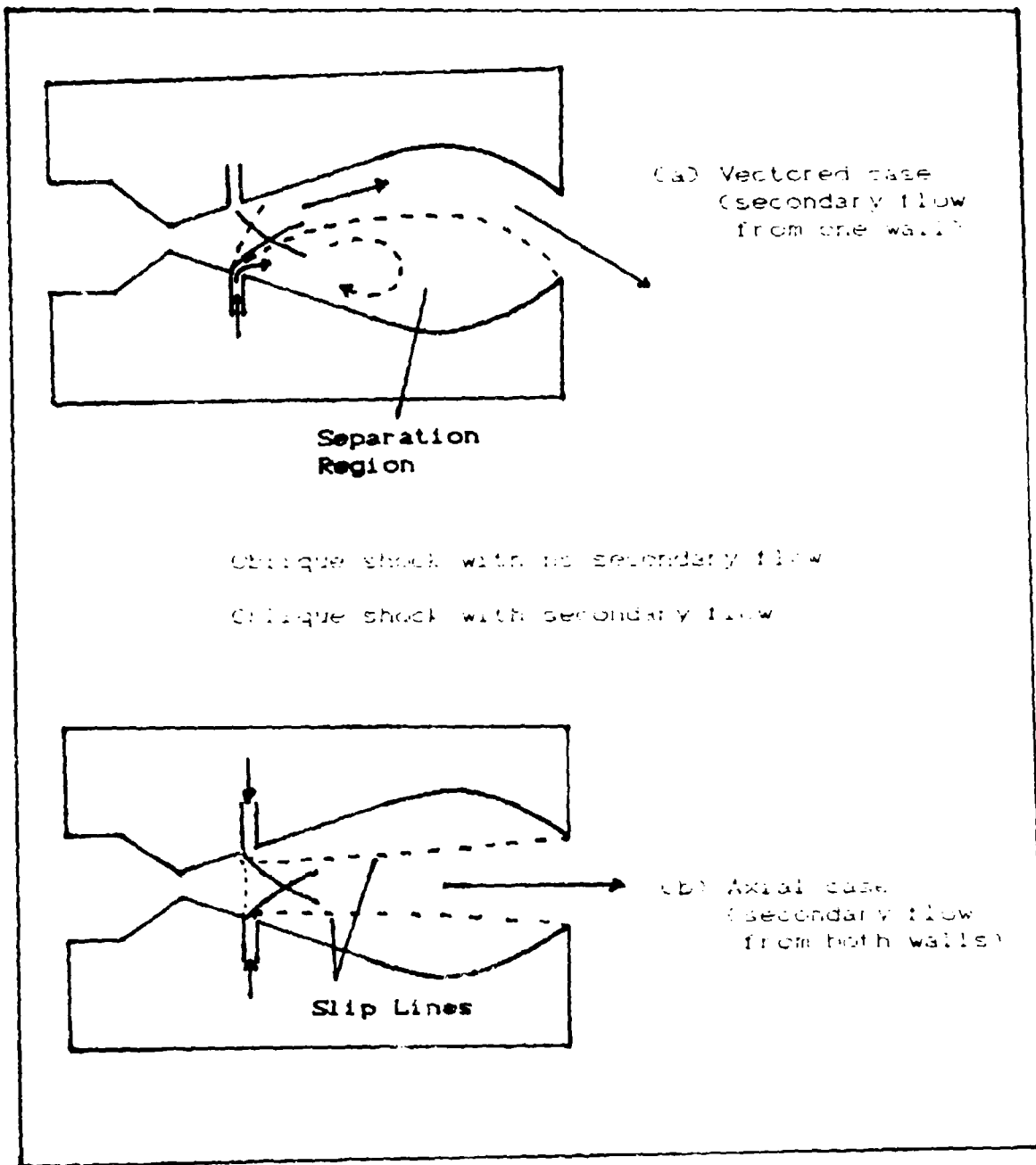


FIG 16 Vectoring and Axial Flow for Nozzles 1 and 2

its oblique shock and thereby increases the shock angle. This increase in pressure on one nozzle half causes flow to attach to the other nozzle half. At the same time, the secondary flow adds mass to the separation region which is entrained by the shear layer caused by the oblique shock. The combination of these effects create a path for the nozzle flow. For the case of axial flow, a Mach reflection is observed at the secondary flow location when both secondary ports have equal flow. This is due to the oblique shock angles being increased to where their intersection forms a Mach reflection to satisfy flow conditions (20:392,393). The combination of slip line development and increased regions of separated flow behind the shocks due to secondary flow create a path for the nozzle axial flow. Static photos of this observation are not available due to malfunctions in the schlieren apparatus.

An interesting transient phenomenon was recorded accidentally when a failure in the primary flow supply dryer allowed some water to enter the nozzle. As the nozzle primary flow began, water droplets traced a vortex path opposite the wall where the flow attached. Figure 17 (a) is a sketch of the path which was observed on several occasions. A possible mechanism for the vortex formation is illustrated in Fig 17 (b) and(c). Two-dimensional vortex pairs have been proven to form when fluid is impulsively started through the sharp edges of a channel opening (1:111). What occurs next is not clear; either the flow

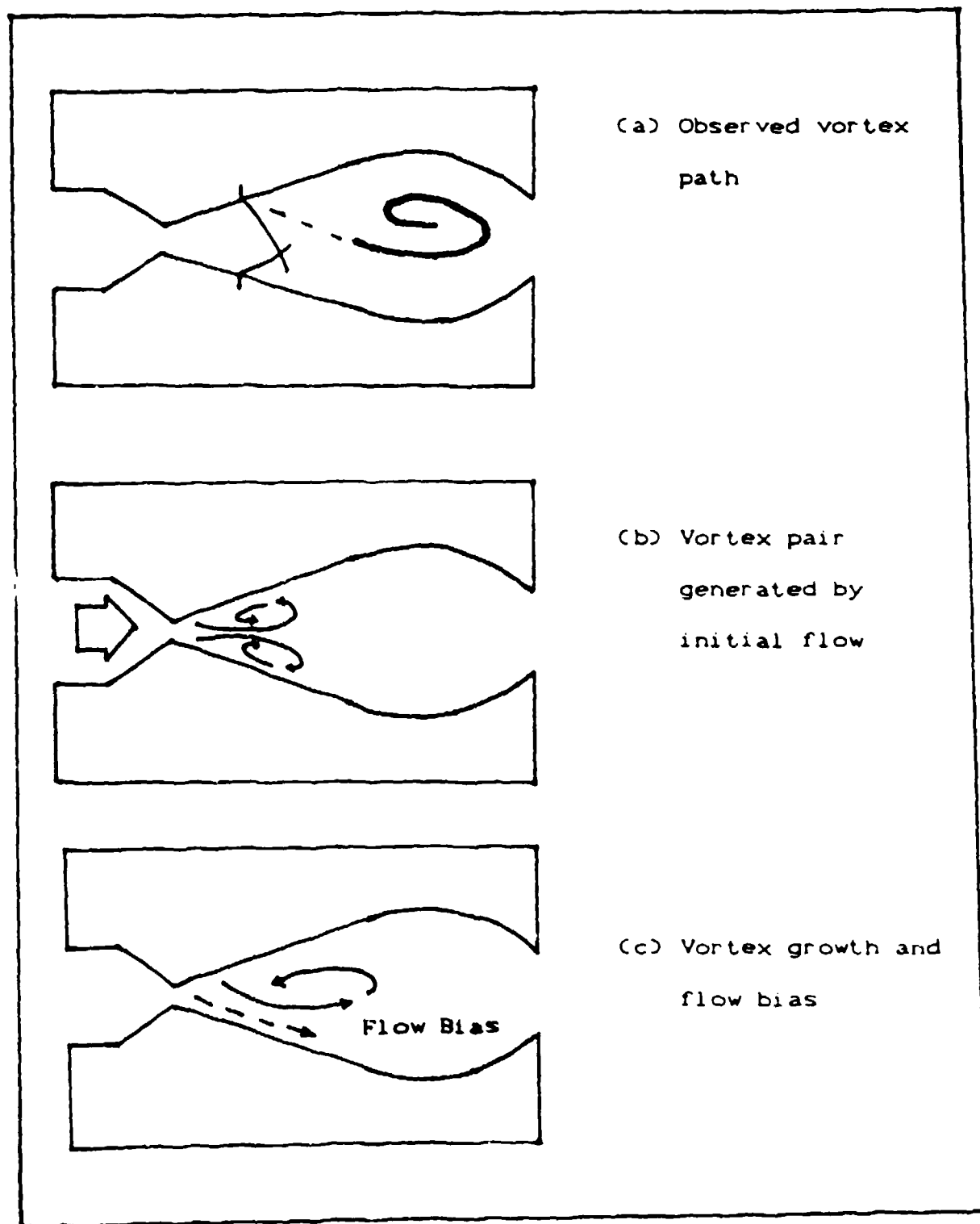


Fig 17 Vortex Formation in Nozzles

becomes biased to one wall causing the vortex opposite it to increase, or some inequality between the vortex pair causes the flow bias. A slight misalignment of the nozzle halves may cause one vortex to begin before the other, creating such a bias. The entire start up mechanism of the nozzle was too fast to determine if the observed vortex trace was the cause or the effect of the flow bias. Future studies using a high speed camera may answer this question.

IV. Nozzle Performance Results

Performance with No Secondary Flow

In order to properly evaluate nozzle vectoring performance, it is important to evaluate its performance with only primary flow first. From this, any inherent angular bias in the flow can be determined and taken into account when evaluating vectored performance. Also, effects of vectored flow on nozzle efficiencies can be evaluated.

The VKI 6-component force balance was used to measure nozzle side and axial forces. From these values, total force and vector angles were calculated using simple trigonometric relations. Test NPRs were obtained by varying primary pressure between 1.2 and 3.5 bar absolute in a reduced back pressure which varied between 0.07 and 0.08 bar absolute.

Thrust Force and Vector Angle

Figures 18 through 22 summarize the force and vector angle data for nozzles 0,1,3,4, and 5. Nozzle 2 was not tested since its configuration with no secondary flow is identical to nozzle 1. Each figure has two sets of data which represent the results of two separate test runs.

Nozzles 0,1, and 3 have approximately the same values of measured axial and total forces. Nozzle 4 values are slightly higher and nozzle 5 has the highest values for measured thrust. An examination of the static pressures

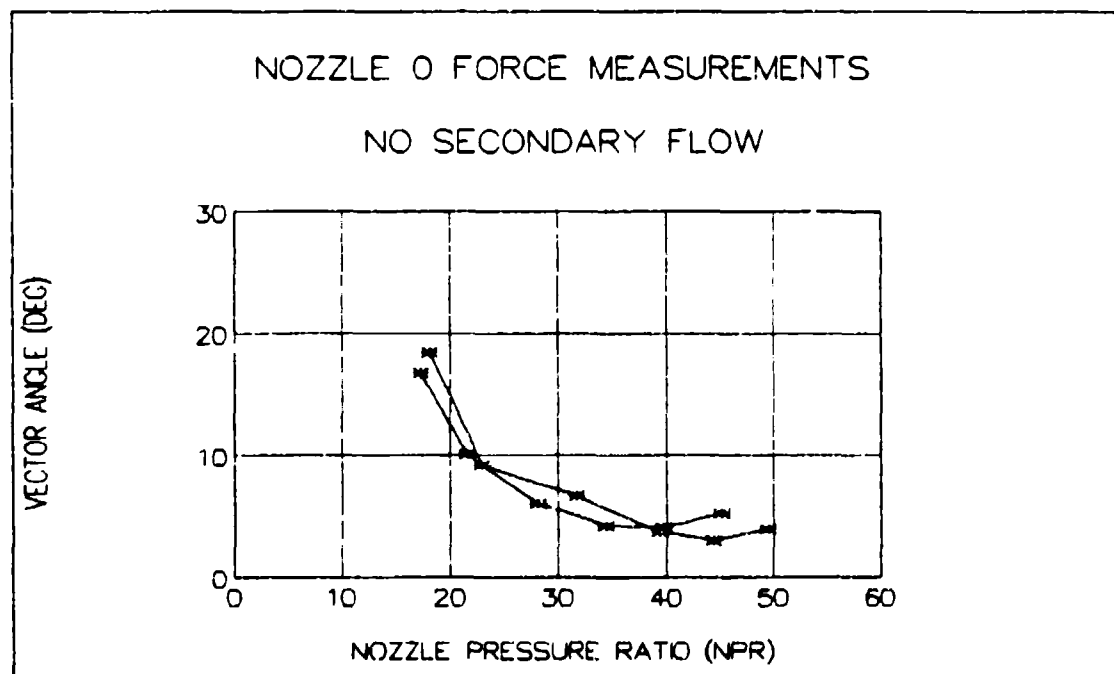
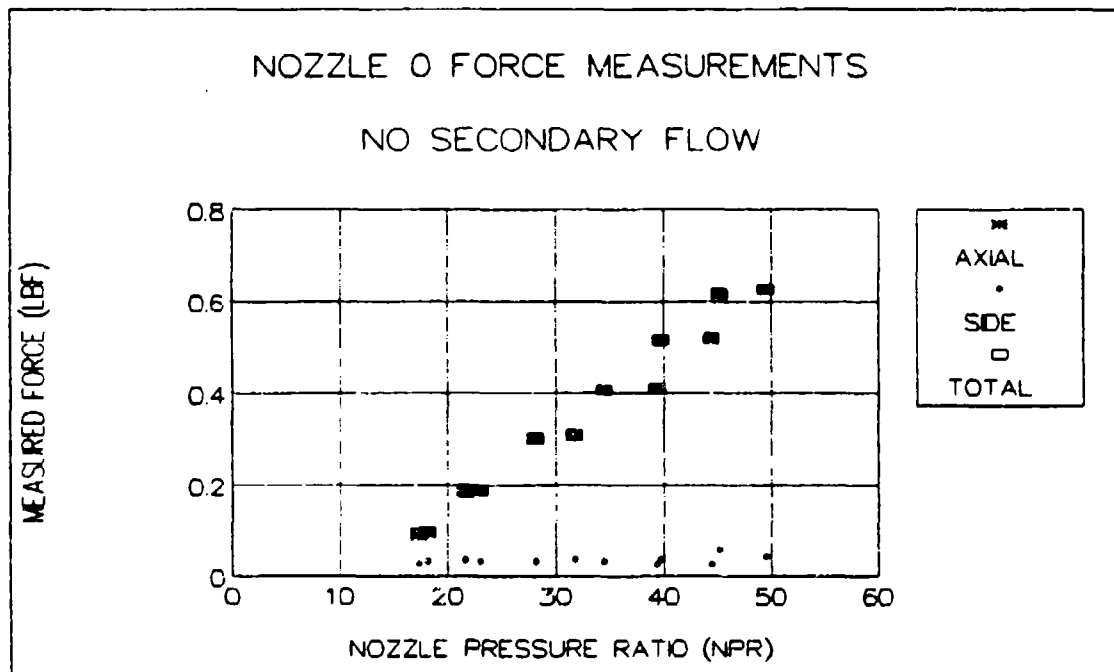


Fig 18 Nozzle 0 Forces and Vector Angles

(no secondary flow)

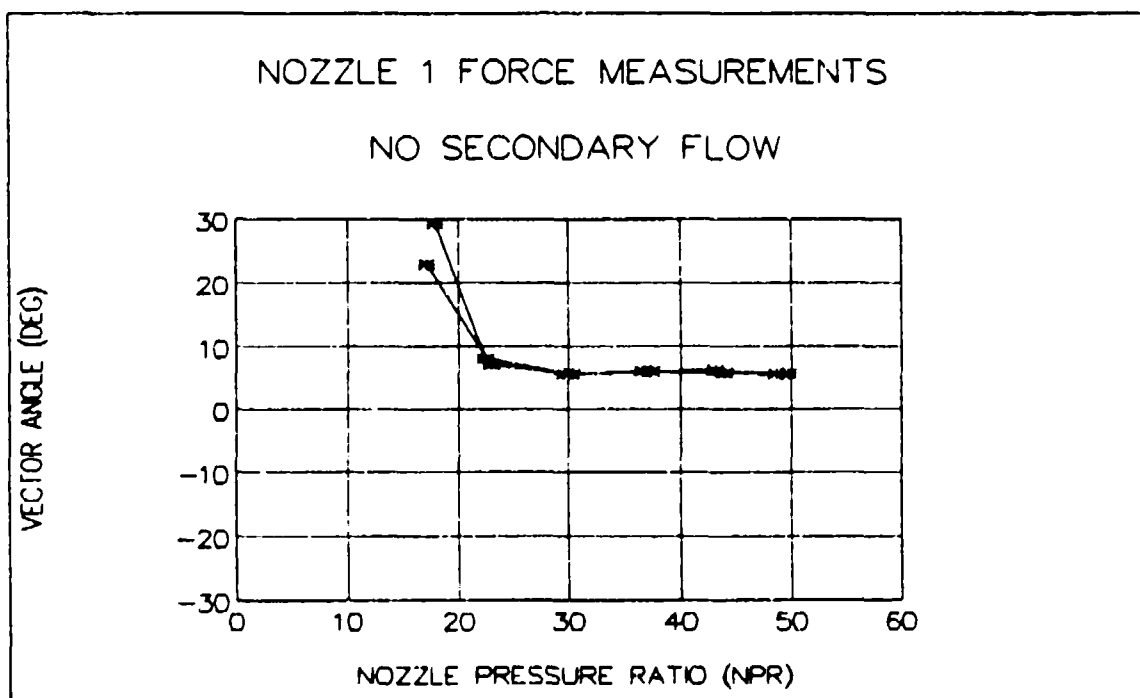
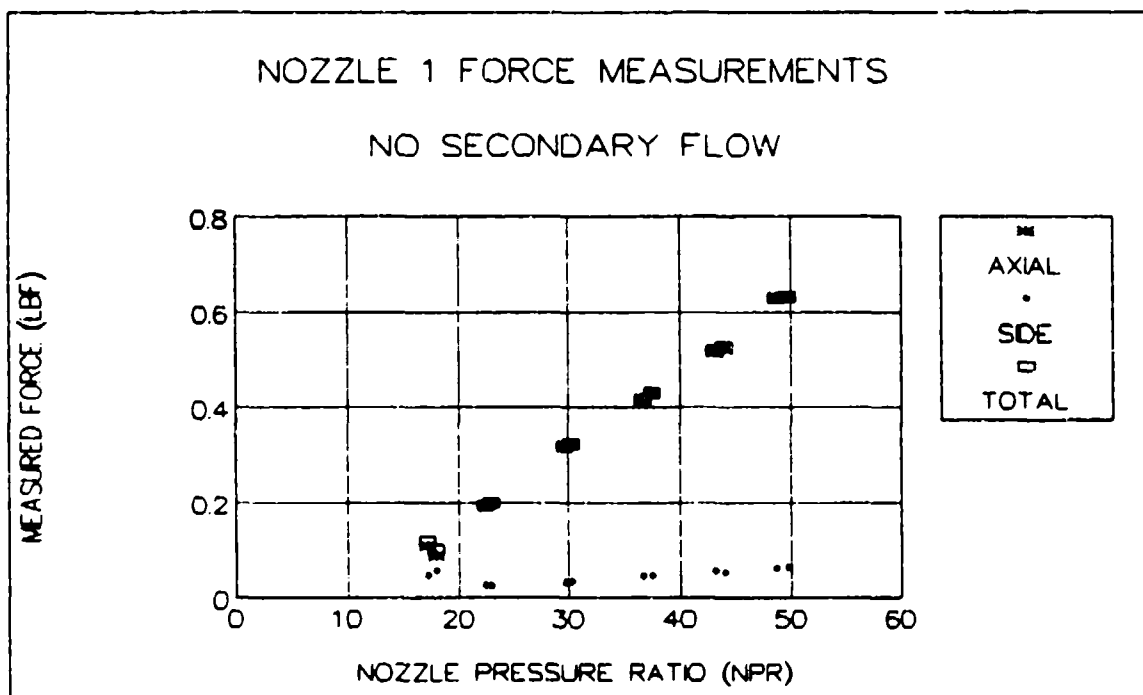


Fig 19 Nozzle 1 Forces and Vector Angles
(no secondary flow)

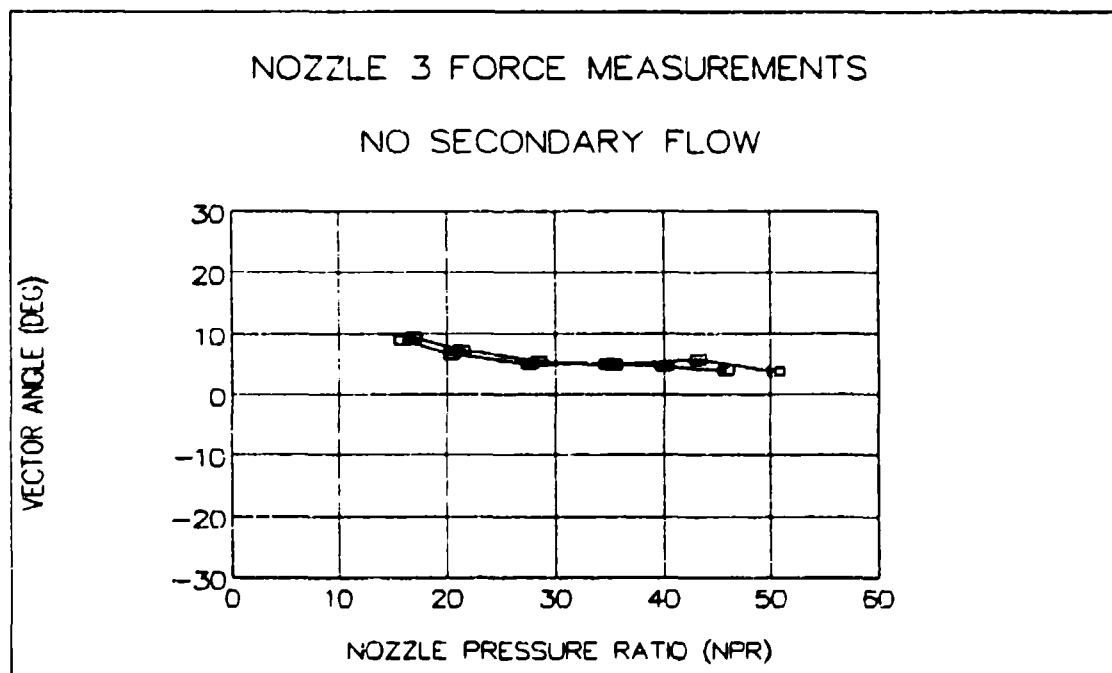
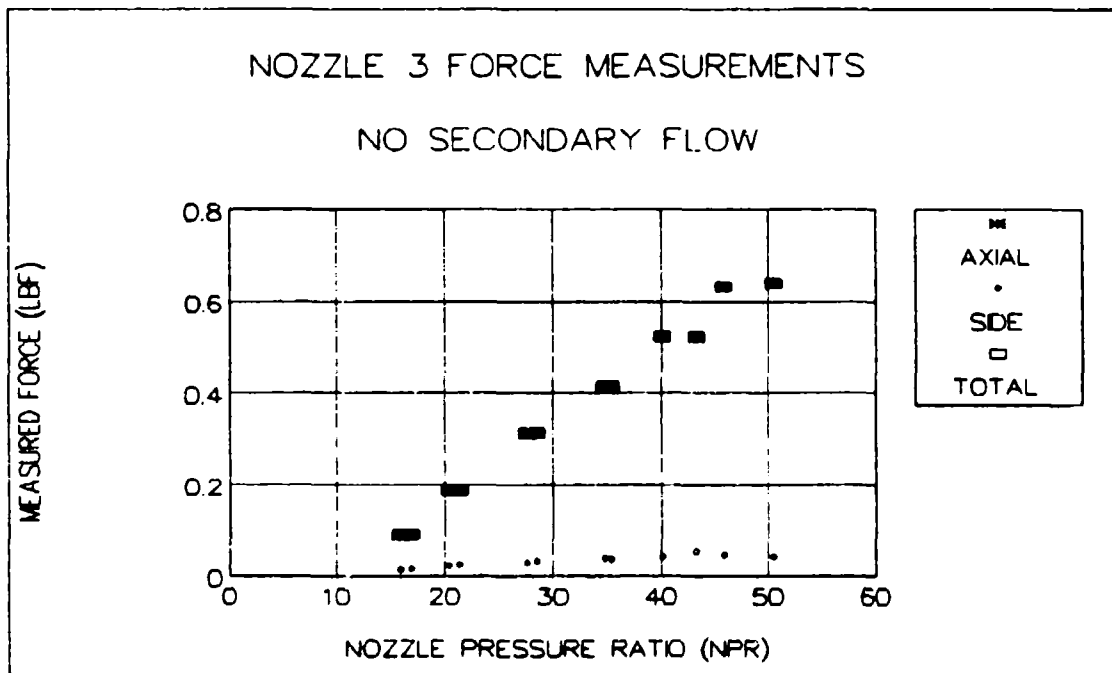


Fig 20 Nozzle 3 Forces and Vector Angles
(no secondary flow)

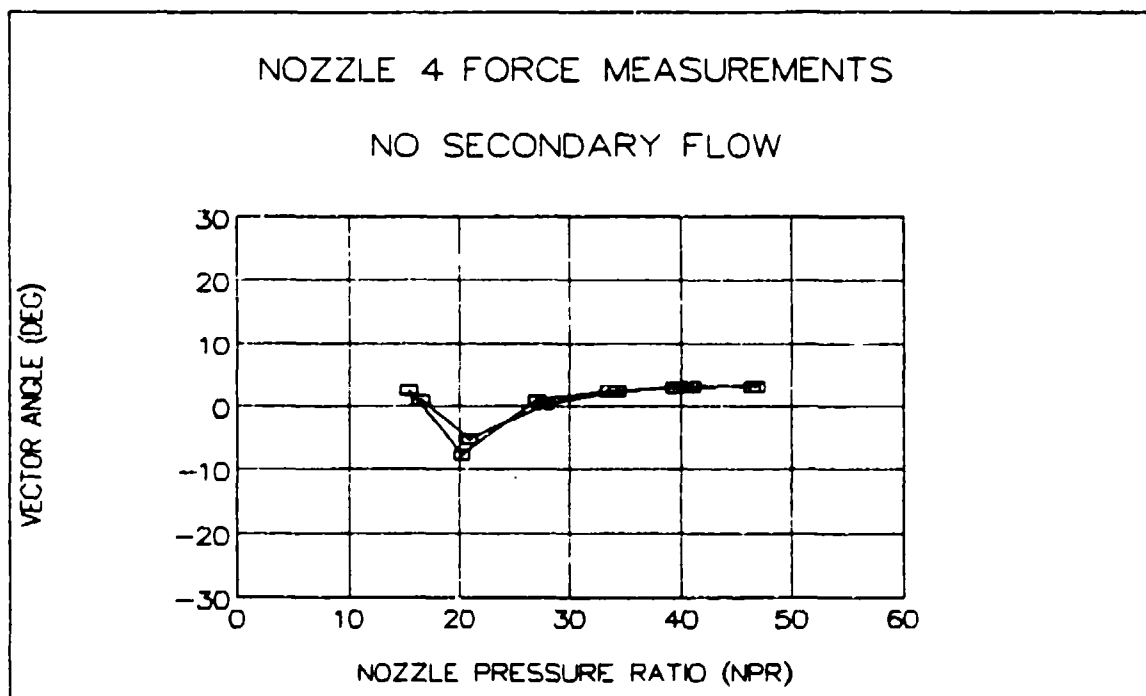
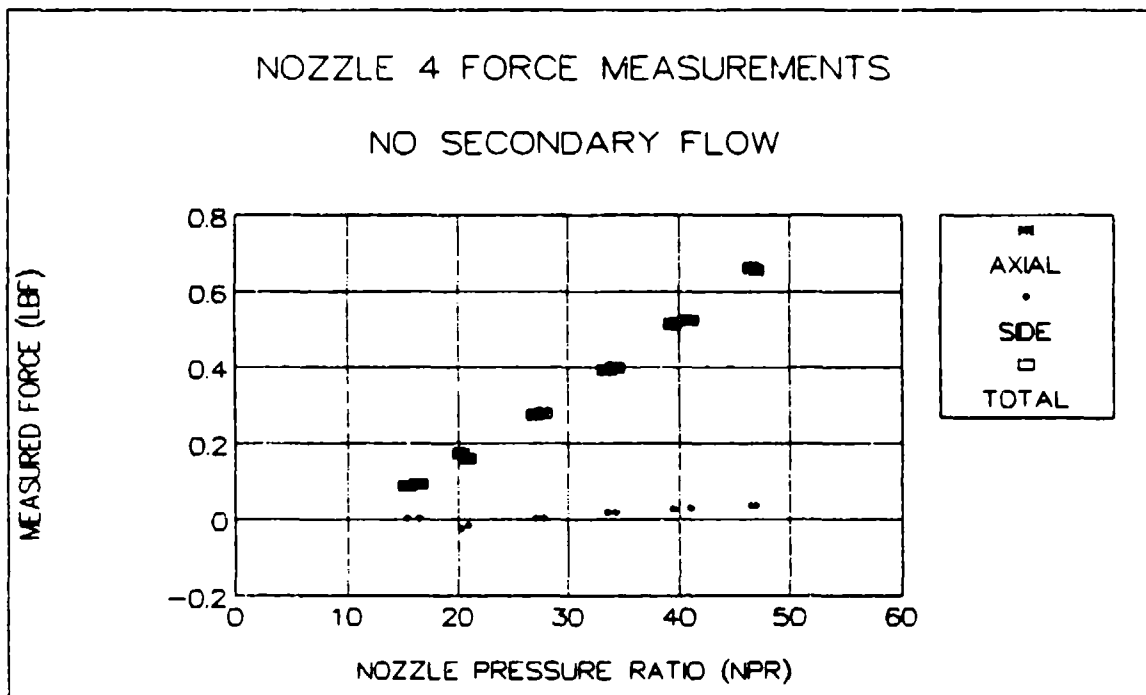


Fig 21 Nozzle 4 Forces and Vector Angles
(no secondary flow)

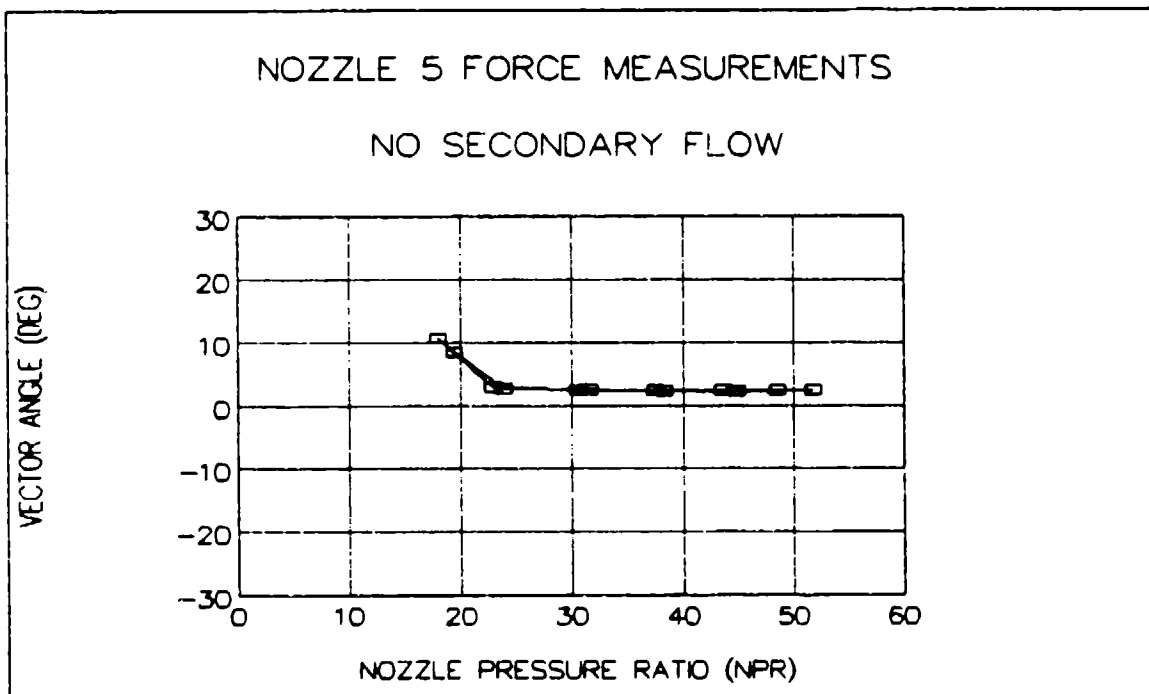
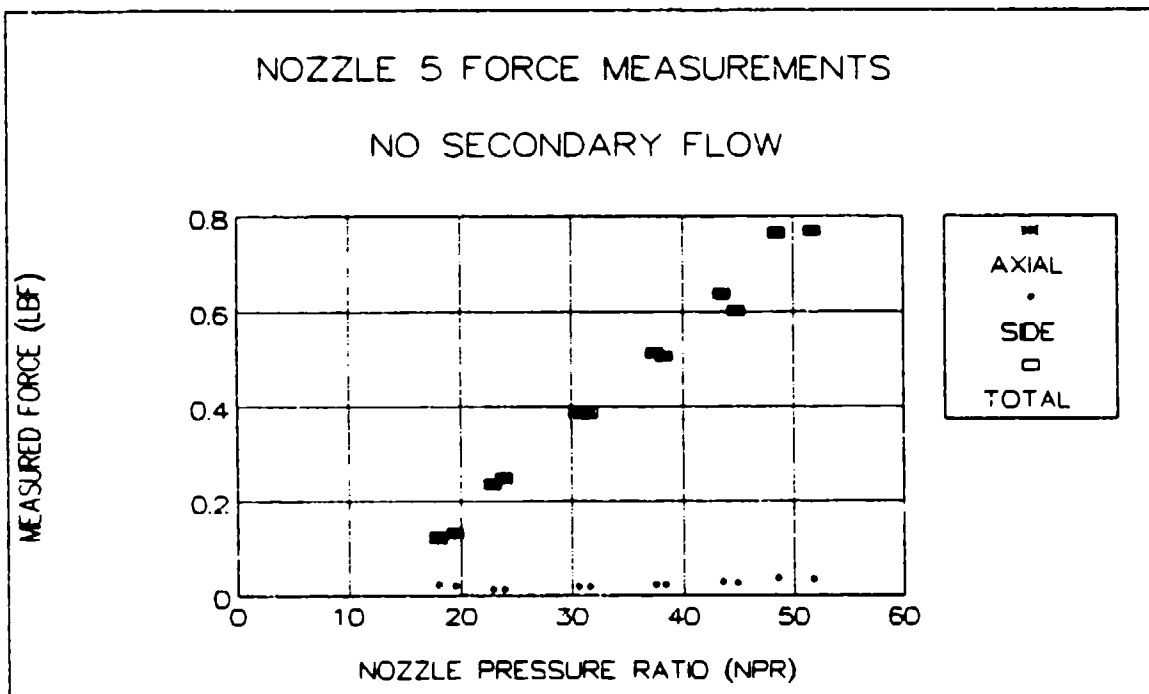


Fig 22 Nozzle 5 Forces and Vector Angles
 (no secondary flow)

inside each nozzle provides an explanation for the variations in measured force values. Figure 23 is a summary plot of the centerline static pressure values for all nozzles. These values were measured using a scanivalve connected to an ENDEVCO pressure transducer at the same conditions as the force measurements. Appendix D contains the individual pressure profiles for each nozzle used to create this summary. The average NPR of the tests is 42.4 ± 1.2 .

The pressure profiles for nozzles 0, 1, and 3 all show an abrupt pressure rise past the secondary port. This indicates that a shock or series of shocks are present. The pressure rise for nozzle 0 is greater than those for nozzles 1 and 3. The existence of normal shocks in nozzle 0 (with no secondary ports) and the existence of oblique shocks in nozzles 1 and 3 (with secondary ports) is consistent with the shock structures discussed in section III. This will also account for the pressure profiles since the static pressure rise across a normal shock is greater than the rise across an oblique shock for a given initial Mach (6:578).

If the normal and oblique shocks caused the only pressure rises in the nozzles, one would expect nozzles 1 and 3 to have greater measured forces than nozzle 0 since their total pressure loss is less. However, the pressure profiles show additional pressure rises through the nozzle cavity for nozzles 1 and 3. The end result seems to be that the overall pressure losses in these nozzles are

SUMMARY OF NOZZLE CENTERLINE PRESSURES

NO SECONDARY INJECTION

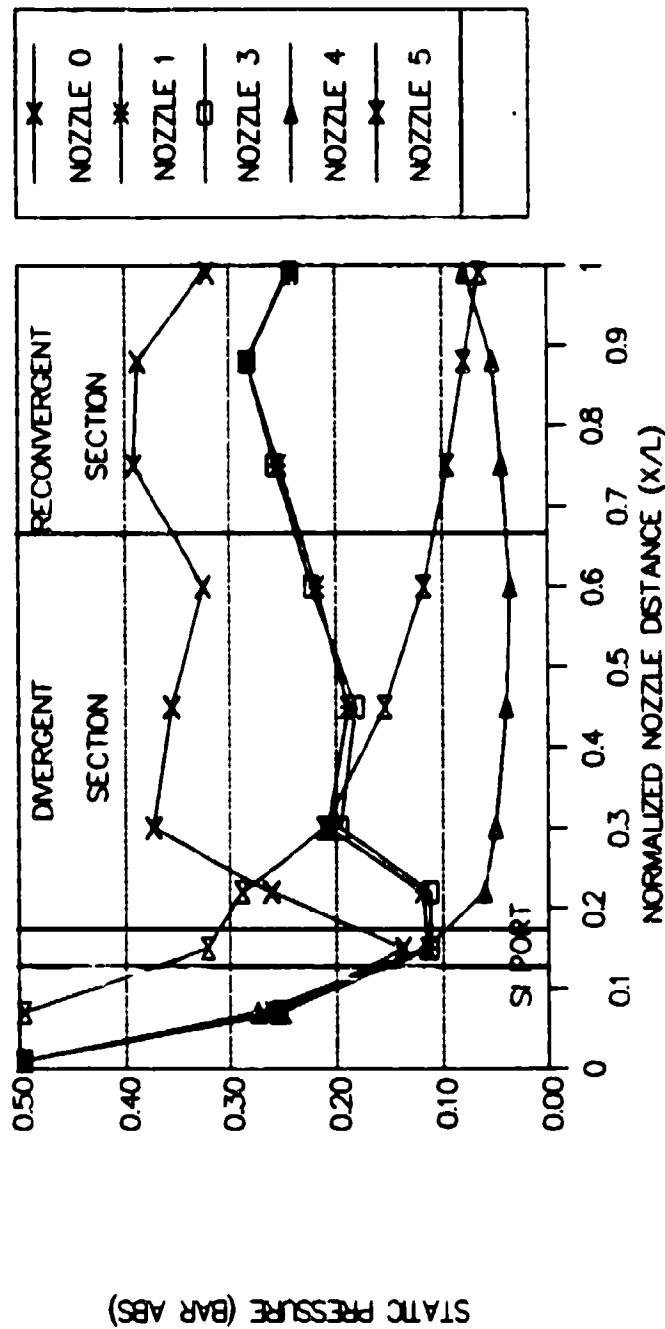


Fig 23 Summary of Nozzle Centerline Static

Pressures (Average NPR = 42.4 ± 1.2)

approximately the same.

The nozzle 4 pressure profile shows a rapid drop in pressure up to the secondary port and a subsequent gradual rise to the exit. This pressure drop indicates that the waves previously observed in Fig 10 were most likely expansion fans rather than shocks. This is consistent with the profile one might expect from an over-expanded, converging-diverging nozzle (7:160).

The profile for nozzle 5 shows a smooth decline in pressure with no pressure rises throughout the nozzle length. This indicates that no shocks were present in nozzle 5, and that it was not over-expanded. With no total pressure loss due to shocks, it is reasonable that nozzle 5 has the largest measured force.

The vector angles of all nozzles are very stable at NPRs greater than 30. While the angles are stable, they are also slightly offset from zero degrees, which is perfectly axial flow. Several possible causes of this slight offset for each nozzle are: (1) misalignment between nozzle halves, (2) manufacturing differences between nozzle halves, or (3) misalignment between the nozzle assembly and the force balance. Unfortunately, time did not allow for further investigation of these offsets.

Thrust Efficiencies

Thrust efficiency for each nozzle condition was determined by dividing the measured total thrust by the

ideal thrust. Ideal thrust calculations assumed isentropic flow expansion where the static pressure at the nozzle exit equals the ambient pressure. Also, ideal exit velocity was calculated using isentropic relations. Appendix B contains complete details of these equations and sample calculations.

Figures 24 through 28 show the thrust efficiencies at various NPRs for nozzles 0, 1, 3, 4, and 5. The measured total thrust values used to determine these are from the same data as Figures 18 through 22. Values for nozzles 0 and 3 are approximately the same, varying between 0.66 and 0.78. Efficiencies for nozzle 1 are slightly higher, varying between 0.74 and 0.87. There does not appear to be any obvious trend for efficiency versus NPR for these nozzles. Table 1 summarizes the maximum and minimum efficiency values for each nozzle along with its average efficiency and appropriate standard deviation. Nozzle 1 has the best average efficiency of all the nozzles with reconverging sections.

Nozzle 4 efficiencies tend to increase with increasing NPR. This is typical for converging-diverging nozzle behavior where at lower NPRs, the formation of shocks within the nozzle may occur. As the NPR increases, the shock is moved out of the nozzle and the efficiency increases due to the decrease in shock losses (6:160). Because of this trend of increasing efficiency, the average efficiency of nozzle 4 is not comparable to the more consistent values of nozzles 0, 1, and 3. However, its magnitude indicates that there is

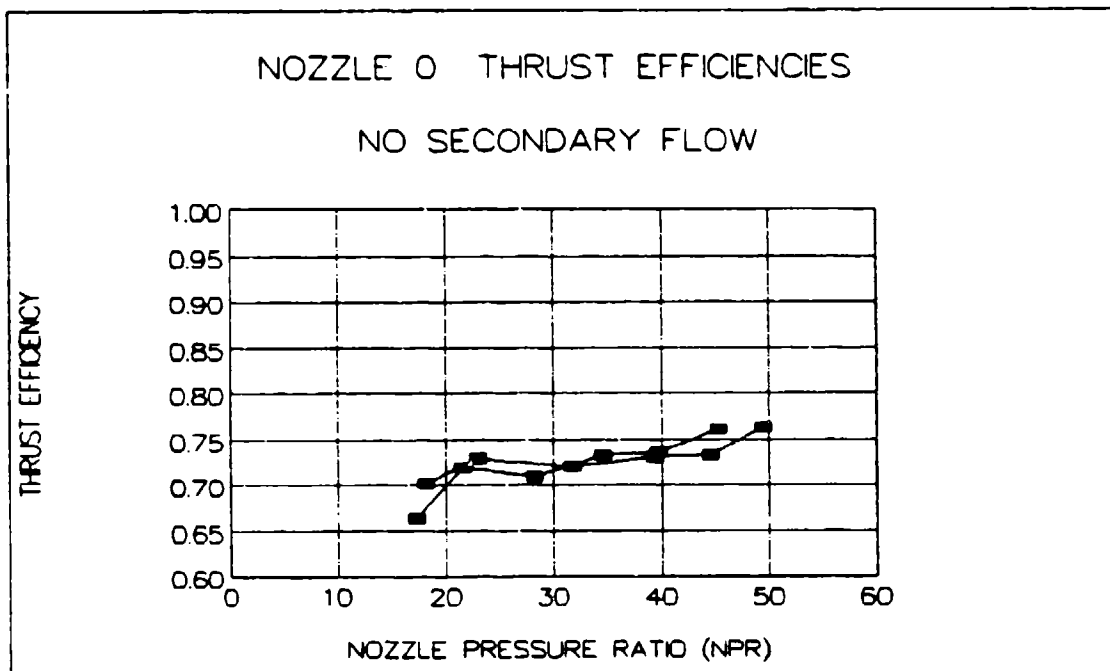


Fig 24 Nozzle 0 Thrust Efficiencies
(no secondary flow)

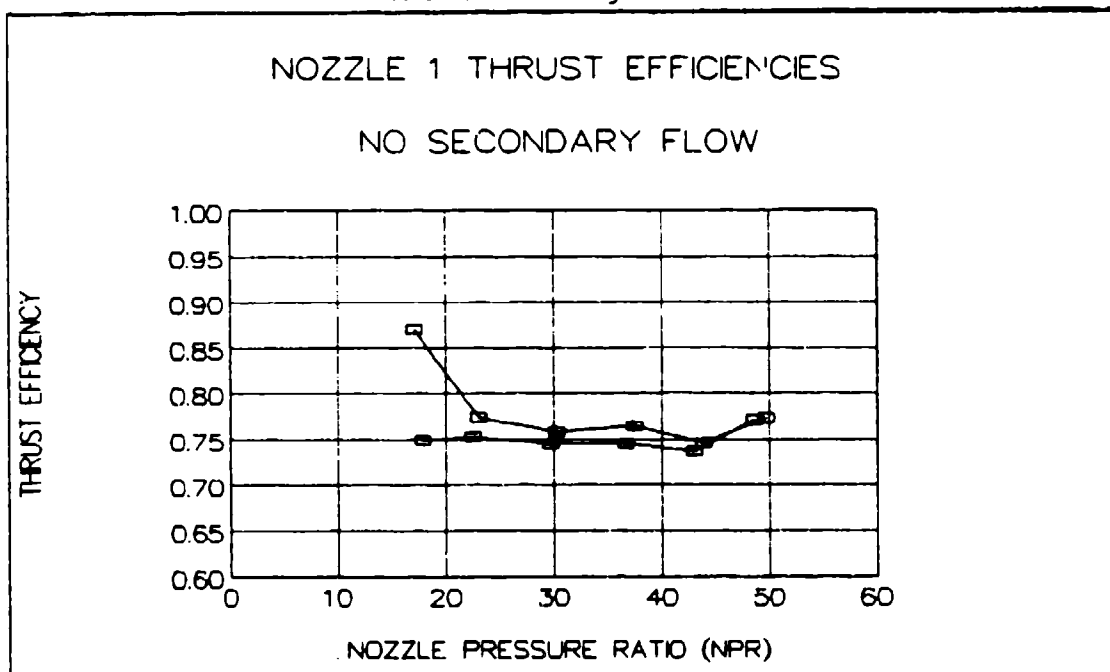


Fig 25 Nozzle 1 Thrust Efficiencies
(no secondary flow)

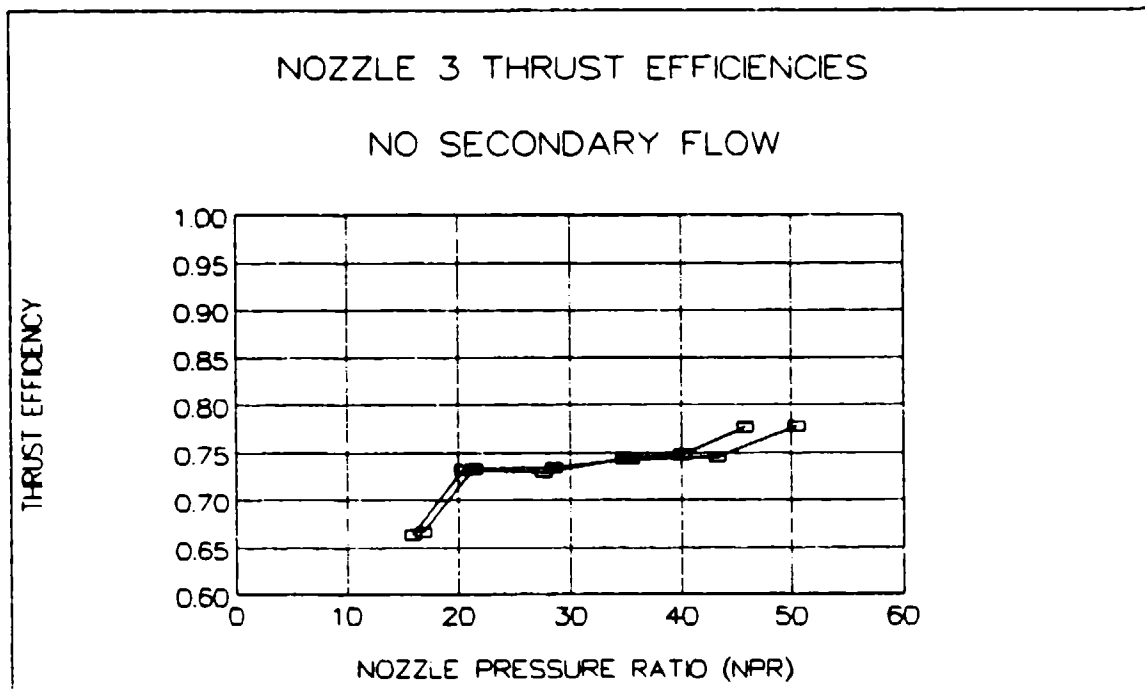


Fig 26 Nozzle 3 Thrust Efficiencies
(no secondary flow)

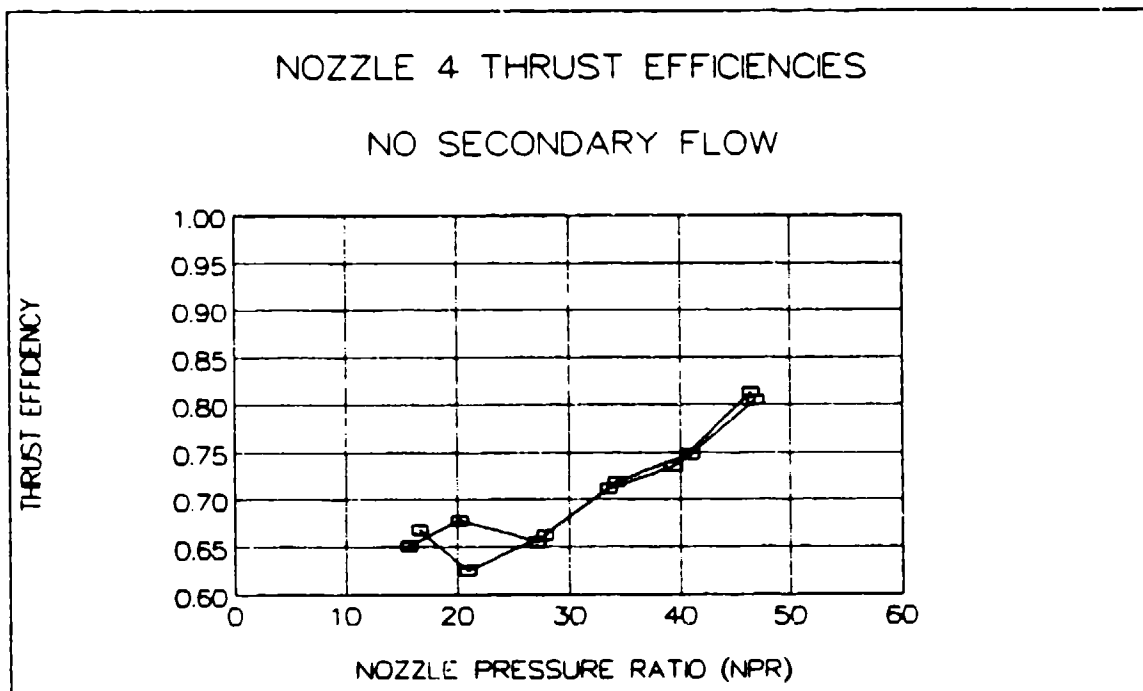


Fig 27 Nozzle 4 Thrust Efficiencies
(no secondary flow)

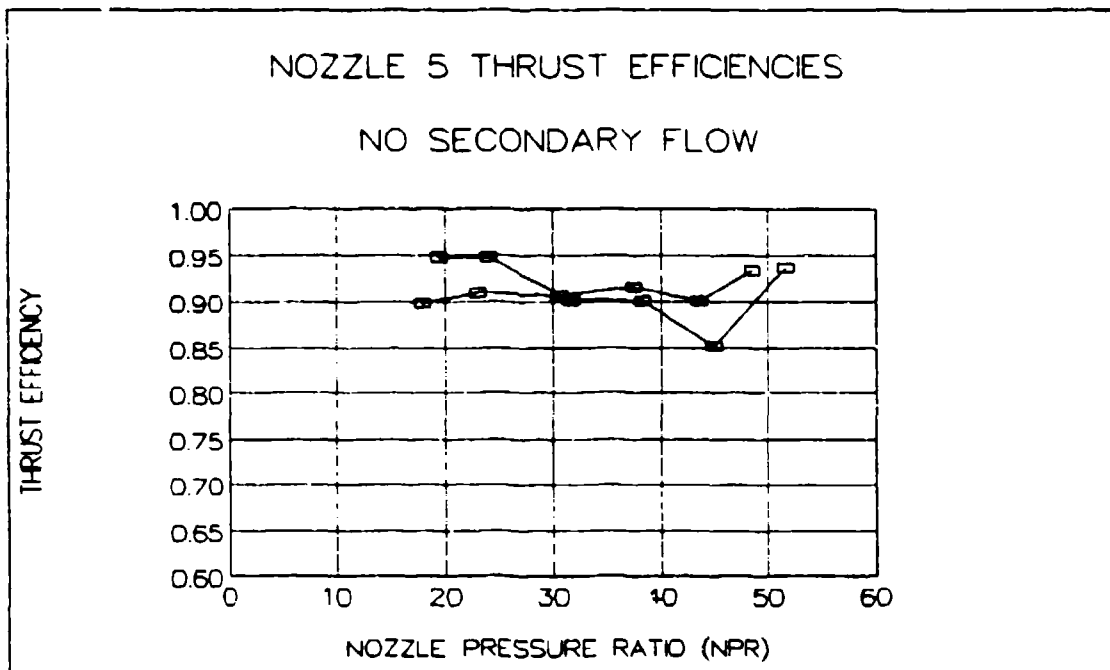


Fig 28 Nozzle 5 Thrust Efficiencies
(no secondary flow)

Table 1. Nozzle Thrust Efficiencies with No Secondary Flow

Nozzle	Minimum Efficiency	Maximum Efficiency	Average Efficiency
0	0.664	0.763	0.725±0.025
1	0.737	0.870	0.765±0.034
3	0.664	0.778	0.733±0.034
4	0.625	0.813	0.706±0.058
5	0.852	0.948	0.913±0.026

little efficiency penalty for adding the reconverging section to the converging-diverging design of nozzle 4. Nozzle 5 efficiencies are considerably greater than all other nozzles. Pressure data for nozzle 5 indicates that it does not suffer from shock losses.

Performance with Secondary Flow

Unless otherwise noted, all tests with secondary flow were performed with an applied primary pressure of 2.923 bar absolute at the nozzle entrance. This was the largest pressure that could be supplied consistently from the existing test facilities to the nozzle. The operating NPR varied slightly according to variations in the back pressure. Tests were performed by keeping the primary pressure constant and varying the mass flow ratio (MFR) of secondary to primary mass flow rates. Appendix C provides the pressure and mass flow values for all test conditions.

Vector Angles

Figures 29 through 32 summarize the vector angles obtained from varying amounts of secondary mass flow. The angles were derived from side and axial force measurements made with the VKI 6-component balance. The figures also show dimensionless side force versus secondary to primary pressure ratio. The following sign convention is used for identifying the location of the secondary flow ports: when viewed from the nozzle plate containing the static pressure

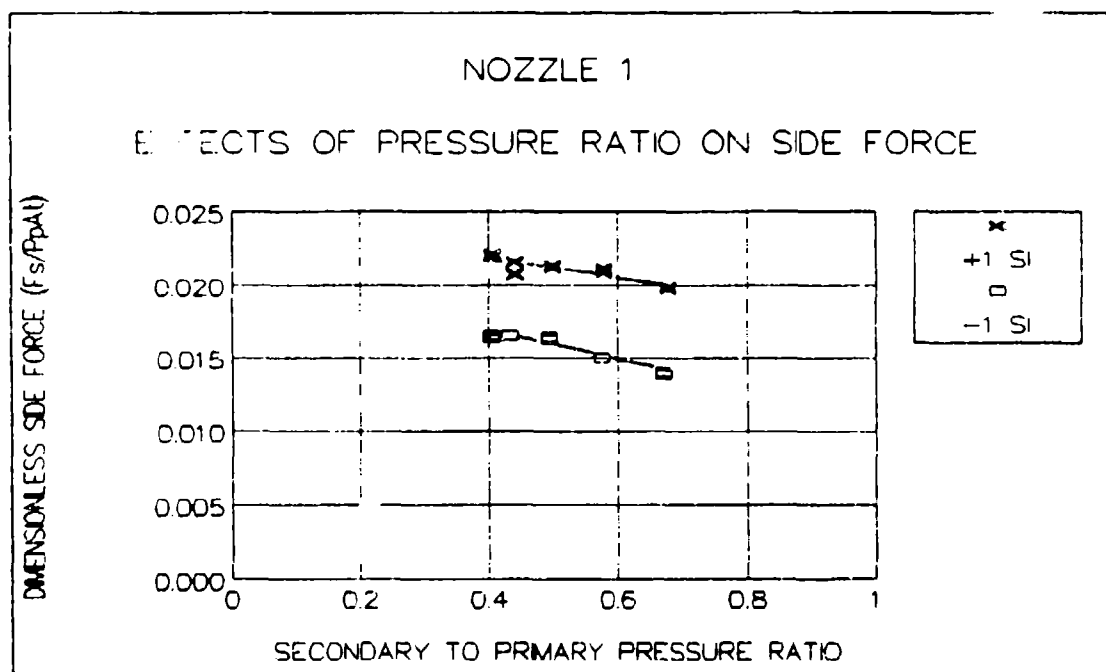
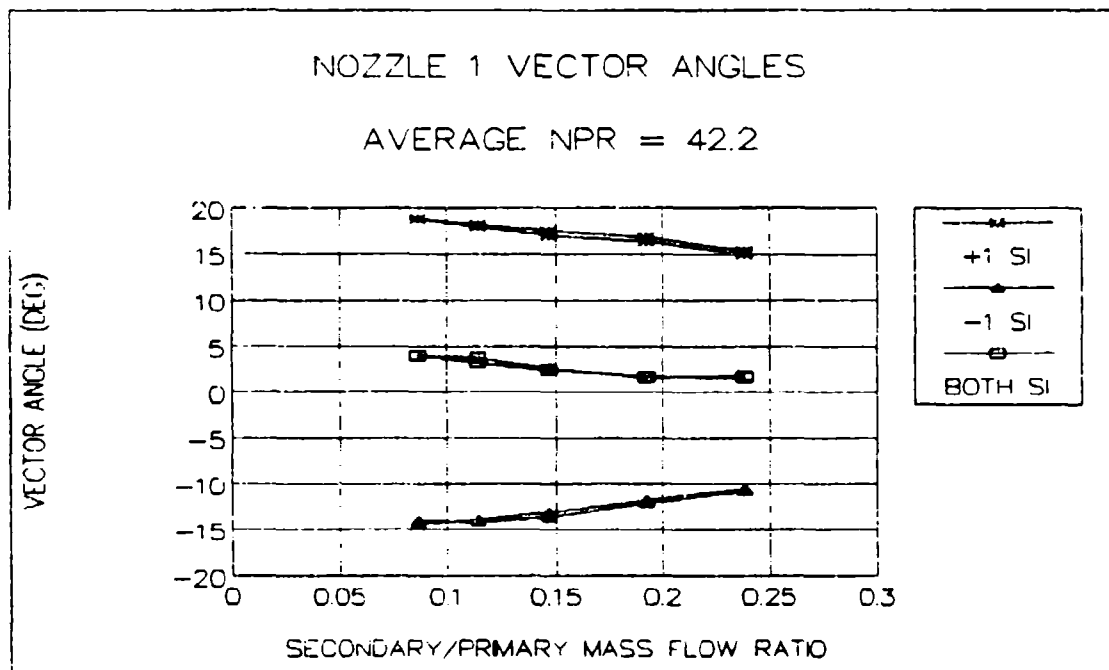


Fig 29 Nozzle 1 Vector Angle and Side Force Variations

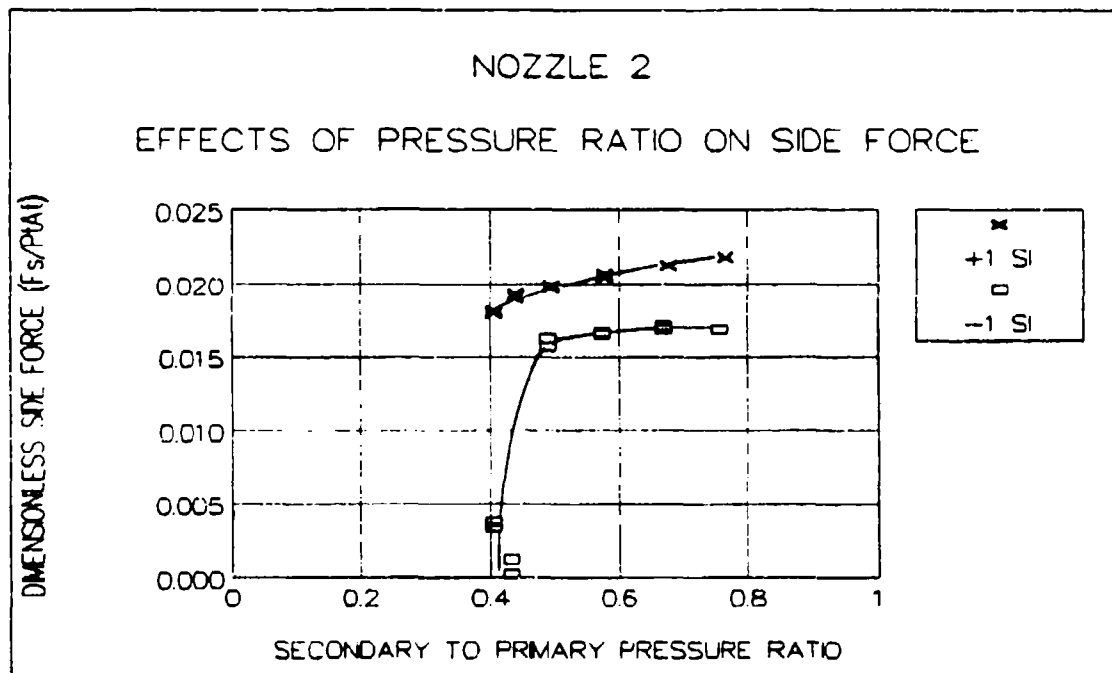
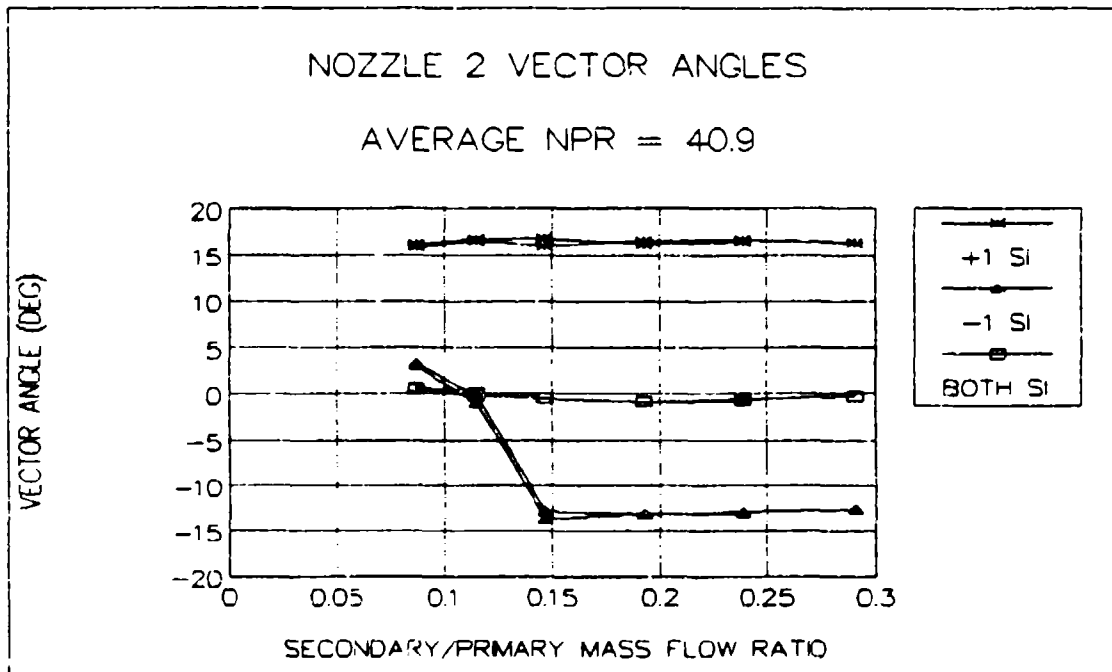


Fig 30 Nozzle 2 Vector Angle and Side Force Variations

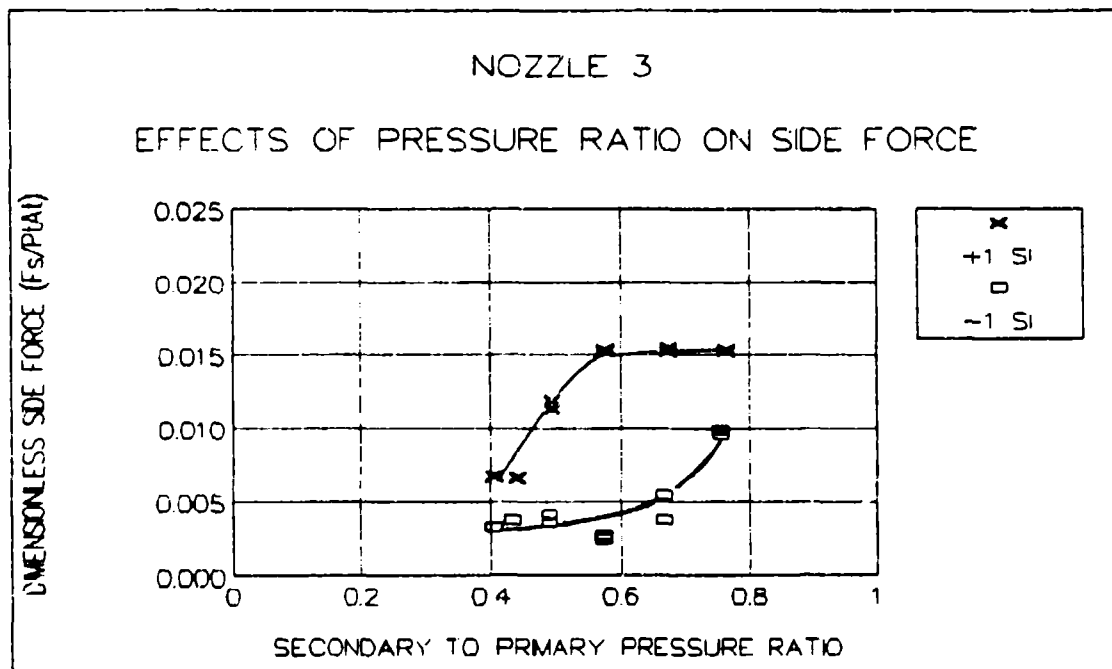
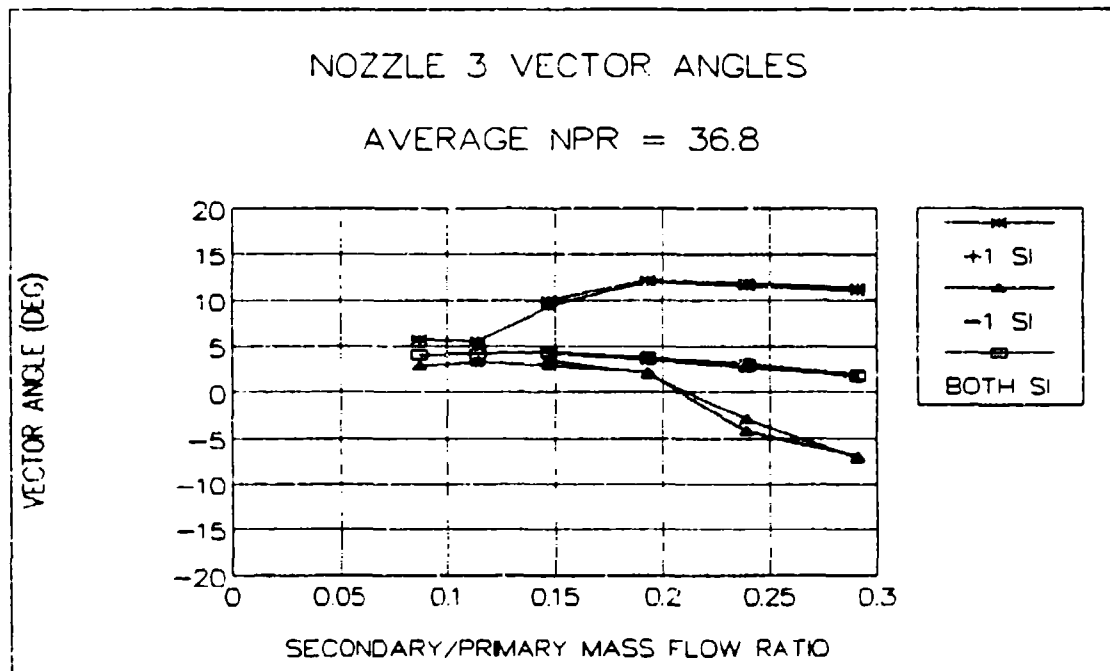


Fig 31 Nozzle 3 Vector Angle and Side Force Variations

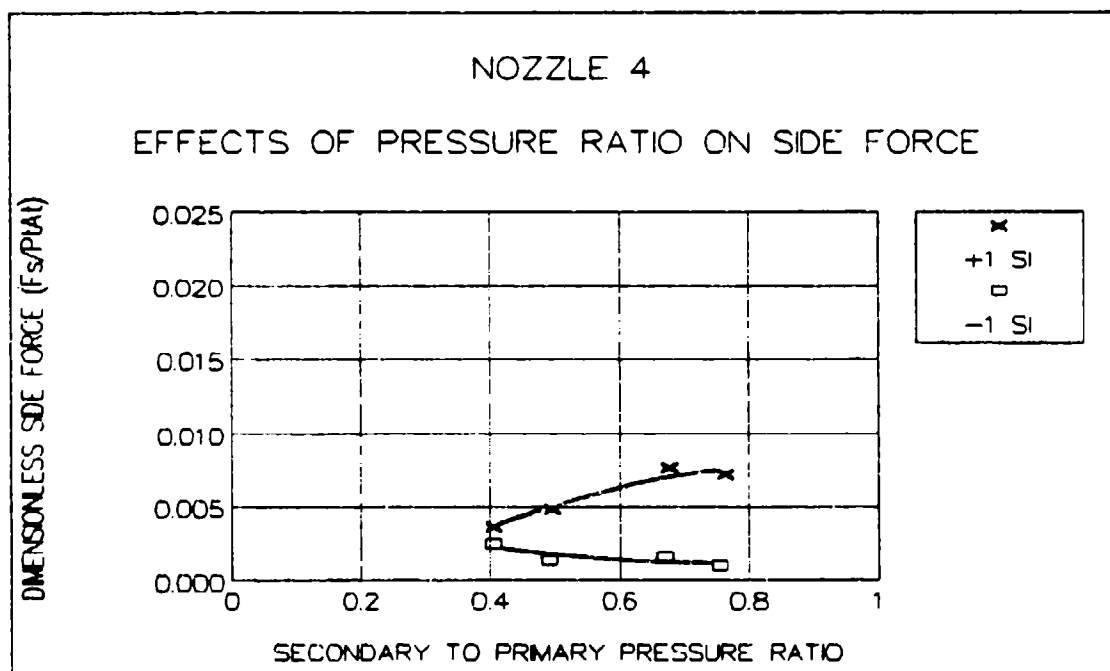
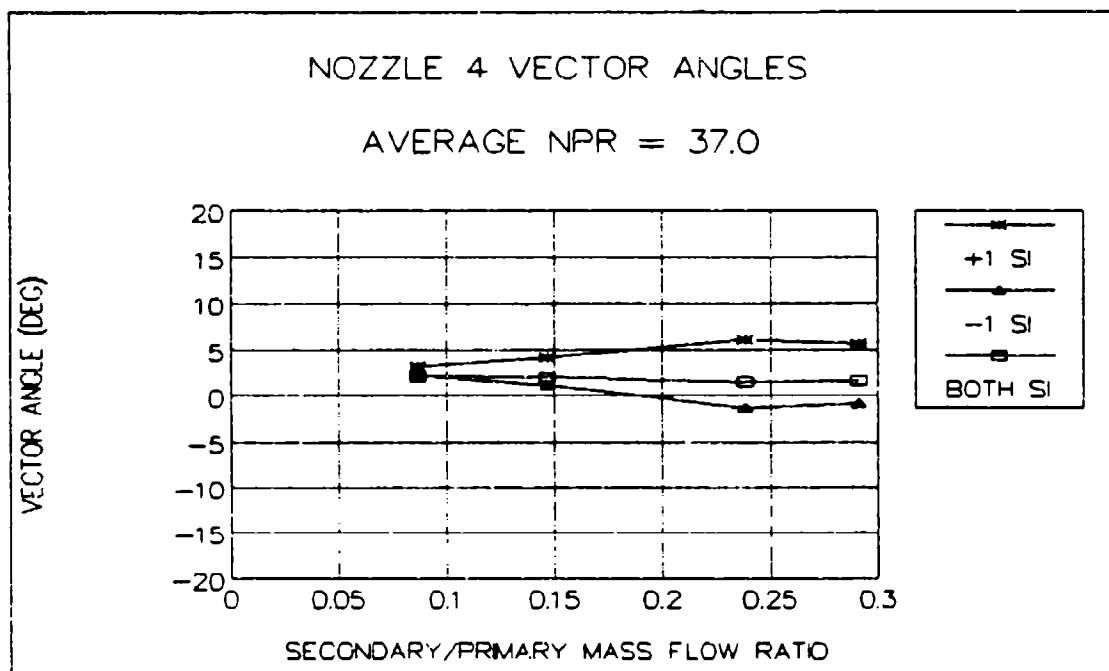


Fig 32 Nozzle 4 Vector Angle and Side Force Variations

ports. "+1 SI" is the upper wall secondary port and "-1 SI" is the lower wall port.

All vector angle plots show positive angle bias, that is, greater values of positive vector angles than negative vector angles. Some of this may be due to misalignment between the nozzle assembly and force balance, but the consistency of the bias direction indicates that it is more likely due to some slight variation in the nozzle test assembly itself.

Figure 29 shows that the nozzle 1 produces vectored thrust at all MFRs tested. The vector angles produced with secondary flow from one wall decrease slightly with increasing MFR. The axial flow produced using secondary flow from both walls has slightly less positive offset from zero degrees than the nozzle had with no secondary flow (Fig 19).

Figures 30 and 31 show that nozzle 2 and 3 have definite transition points between unvectored and vectored flow. However, these transition points do not occur at the same MFR for both vector directions, again indicating that some internal variations in the nozzles may account for this. When vectored flow is achieved, the vector angles produced remain essentially constant with increasing MFR. As with nozzle 1, the axial flow produced using secondary flow from both walls for nozzles 2 and 3 has less positive offset from zero degrees than the nozzles had with no secondary flow (Figs 19 and 20).

Figure 32 shows that nozzle 4 produced relatively small vector angles, even at high MFR. This illustrates the effectiveness of the reconverging section in producing vectored flow.

For all figures, the dimensionless side force values seem to level off as the secondary to primary pressure ratio increases. Nozzles 2 and 3 in particular show sharp side force value rise to a plateau, similar to trends found by Lambert and Franke (11:4). Figure 33 shows the relation between MFR and the secondary to primary pressure ratios used in Figs 29 through 32.

Table 2 summarizes the average vector angle resulting from secondary flow from one wall measured from the angle resulting from secondary flows from both walls. In most cases, the vector angle is biased to the positive direction.

Figure 34 is a summary of all data contained in Figs 29 through 32. It presents the data as vector ranges, which are simply the arithmetic difference between the two vector angles. Nozzle 1 has the best vector range values at MFRs below 0.147 while nozzle 2 has the best vector range values above that MFR. While nozzles 2, 3, and 4 all have increasing vector ranges with increasing MFR, the range of nozzle 1 vector angles decreases slightly with increasing MFR. The trend of nozzle 1 is consistent with the trends of Talda's data with a similar nozzle (16:58-60).

The MFR values which produced the best vector ranges at the flow conditions of a primary pressure of 2.923 bar

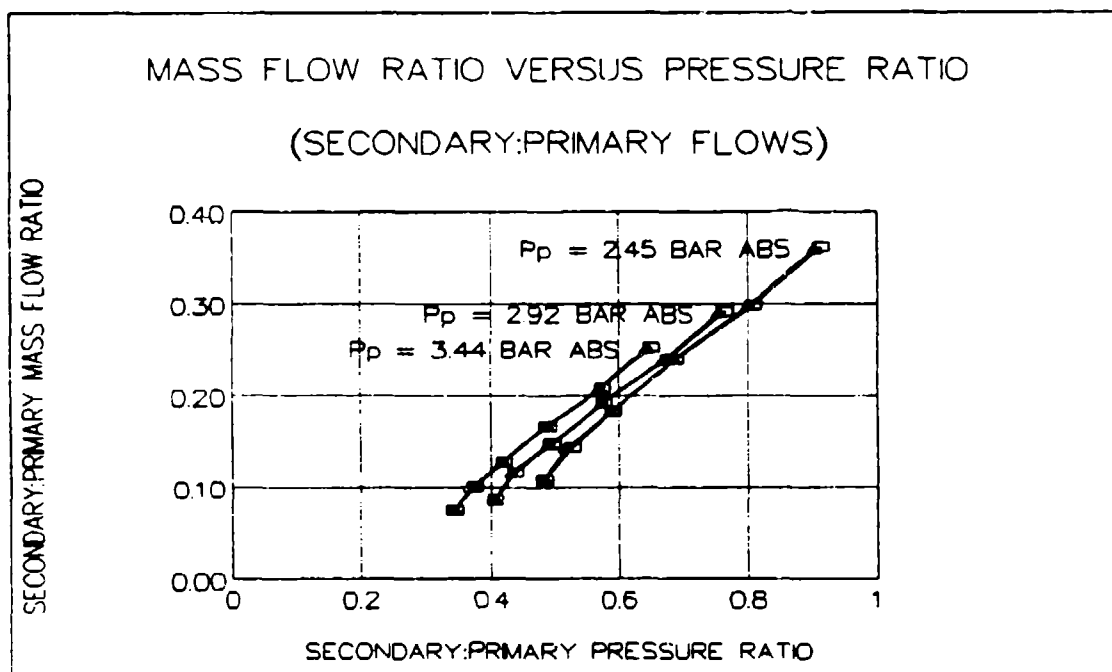


Fig 33 Mass Flow Ratio versus Pressure Ratio
(Secondary Flow to Primary Flow)

Table 2. Vector Angle Measured from Angle Produced by
Both Secondary Flows

MFR	VECTOR ANGLE			
	NOZZLE 1	NOZZLE 2	NOZZLE 3	NOZZLE 4
0.087	+14.9/-18.2	+15.5/+2.5	+1.7/-1.2	+1.1/+0.1
0.115	+14.7/-17.5	+16.7/-0.5	+1.4/-0.9	---
0.147	+14.9/-15.8	+16.9/-12.7	+5.4/-1.1	+2.1/-0.8
0.193	+14.9/-13.6	+17.2/-12.3	+8.5/-1.6	---
0.239	+13.5/-12.4	+17.2/-12.4	+8.9/-6.5	+4.6/-2.8
0.291	---	---	+9.4/-8.9	+4.0/-2.4

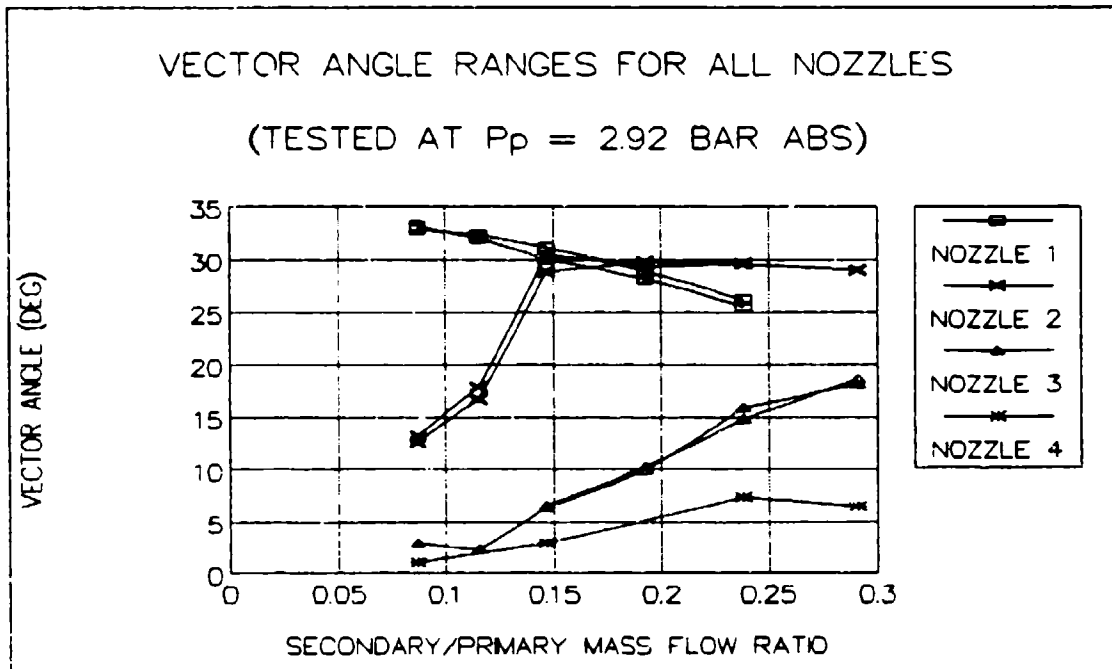


Fig 34 Summary of Secondary Flow-Induced Vector
Angle Ranges

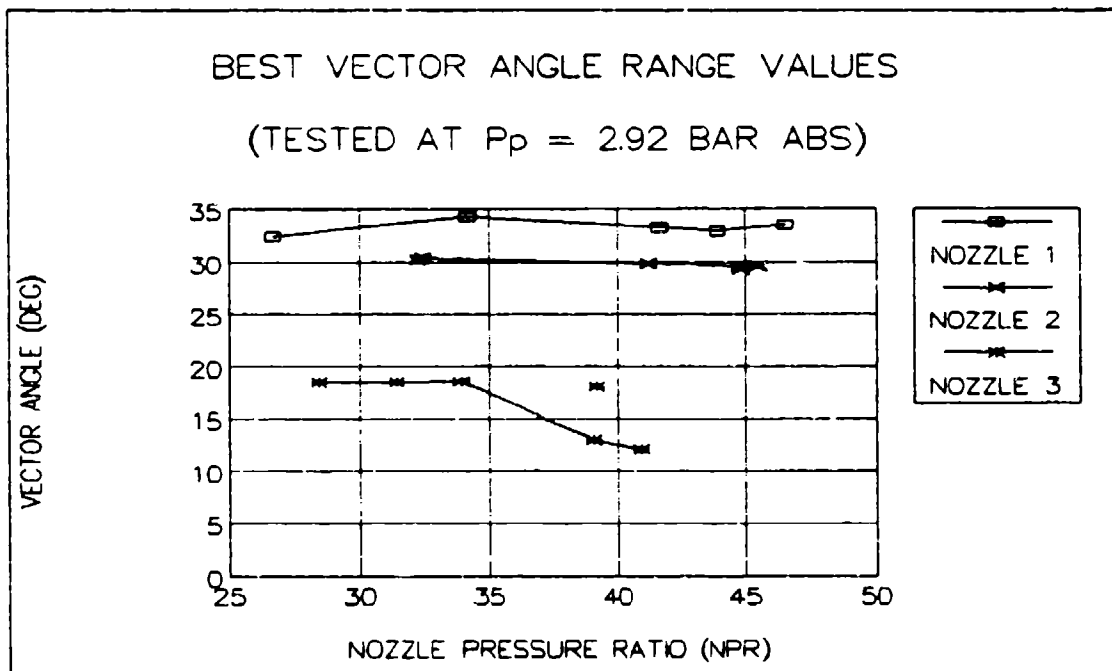


Fig 35 Vector Range Variation with NPR

absolute were selected for further testing. For this testing, the MFR value for the appropriate nozzle remained constant while the NPR varied. Table 3 lists the MFR values and their resulting best vector ranges for all nozzles.

Table 3. Best Vector Angle Range Values
for Nozzles Tested

Nozzle	MFR	Best Vector Range
1	0.087	33.1
2	0.193	29.5
3	0.291	18.3
4	0.239	7.4

Figure 35 summarizes the vector angle range variance with NPR. With varying NPR, all nozzles keep their relative position; nozzle 1 had the best vector range, followed by nozzle 2 and then nozzle 3. All nozzles show little range variation with varying NPR, except nozzle 3 which has decreased range with increasing NPR.

Thrust Efficiencies

Thrust efficiencies for flow with secondary injection were determined by the same methods used for flow with no secondary injection, except the ideal thrust was calculated by multiplying the isentropic exit velocity by the total mass flow rate (primary plus secondary). Figures 36 through

39 show the thrust efficiencies at various MFRs for nozzles 1,2,3, and 4. In some cases, the nozzles show a slight decrease in efficiency with increasing MFR. This decrease may be caused by increased nozzle losses as increasing MFR is accompanied by an increased ratio between secondary and primary pressures. This increased pressure ratio can lead to increased shock strengths and their resulting losses in the nozzle. In most cases, the thrust efficiencies varied less than 5% through the MFR range tested.

Table 4 shows the average thrust efficiencies for all nozzles at the three vectoring conditions. Nozzle 1 had the best efficiency with the no secondary flow case, and it has the best efficiencies for individual secondary flow injection cases. Nozzle 3, however, has the best efficiency when both secondary flow are used. The average efficiencies determined for these CJTVC nozzles are in excellent agreement with the efficiencies determined by Talda for vectored flow also using a circular secondary injection port (16:97).

Side Momentum Gains

As previously mentioned, the side momentum gain (G_M) is defined as the ratio of the measured side force to the momentum of the secondary jet flow. Obviously, large values of G_M are desirable since it reflects that a large side force is being produced by a small quantity secondary jet momentum. Since the side force is a result of primary and

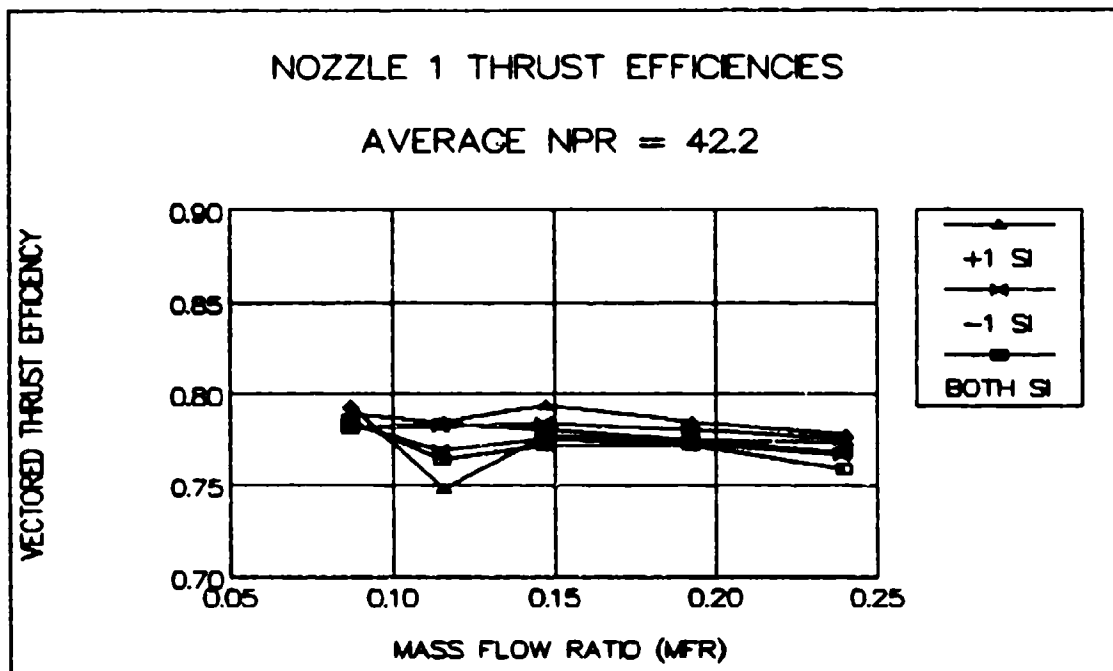


Fig 36 Nozzle 1 Thrust Efficiencies
(with secondary flow)

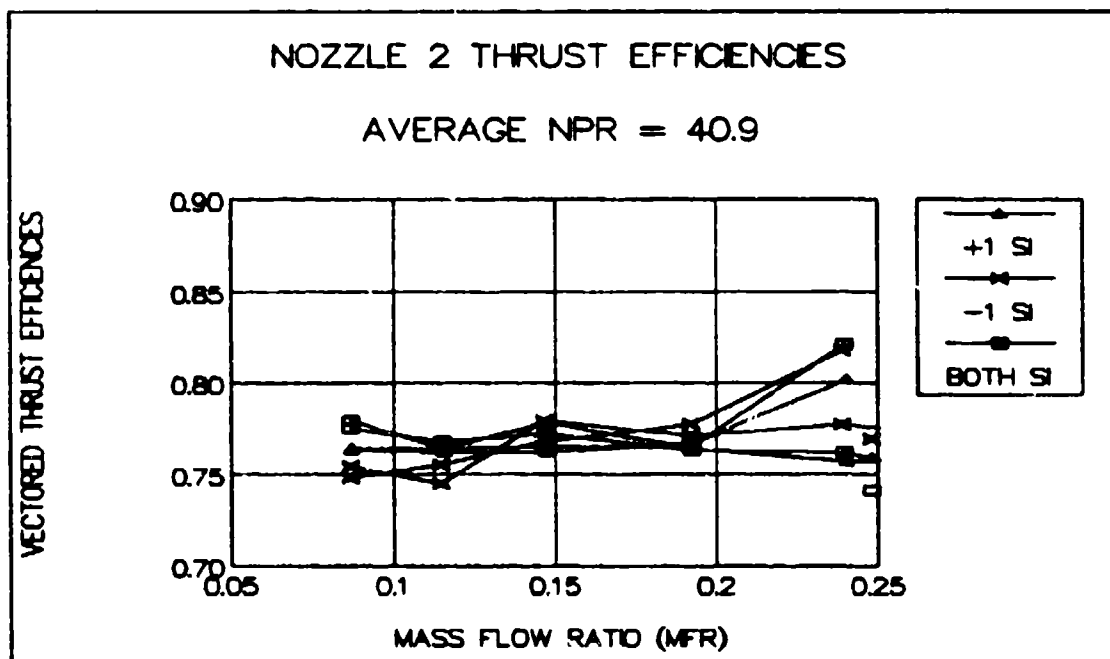


Fig 37 Nozzle 2 Thrust Efficiencies
(with secondary flow)

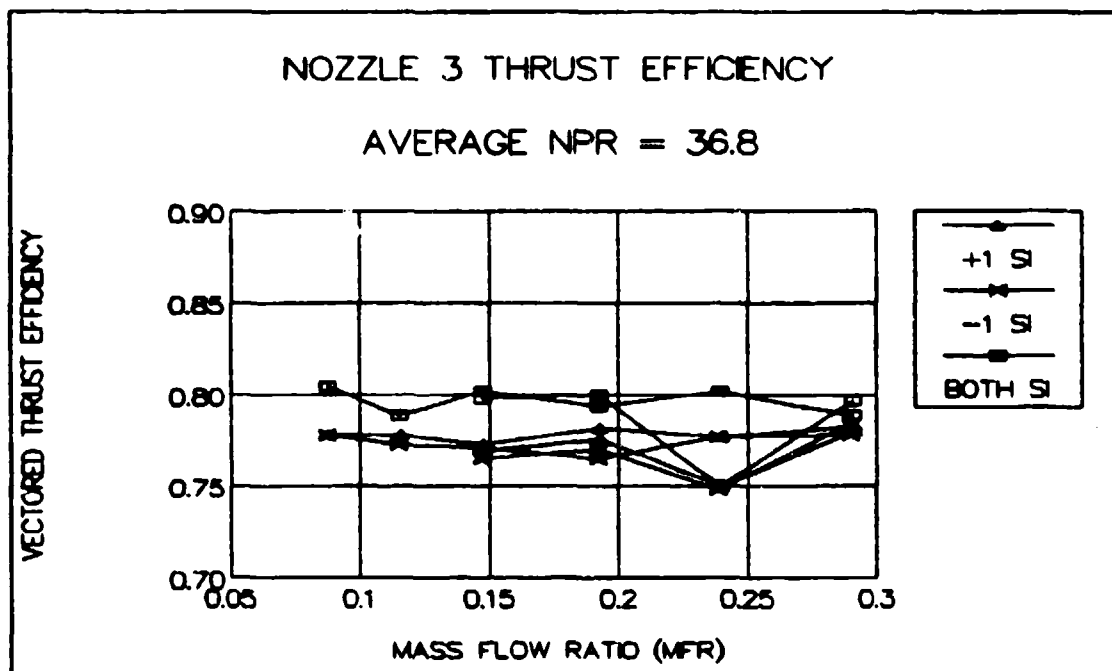


Fig 38 Nozzle 3 Thrust Efficiencies
(with secondary flow)

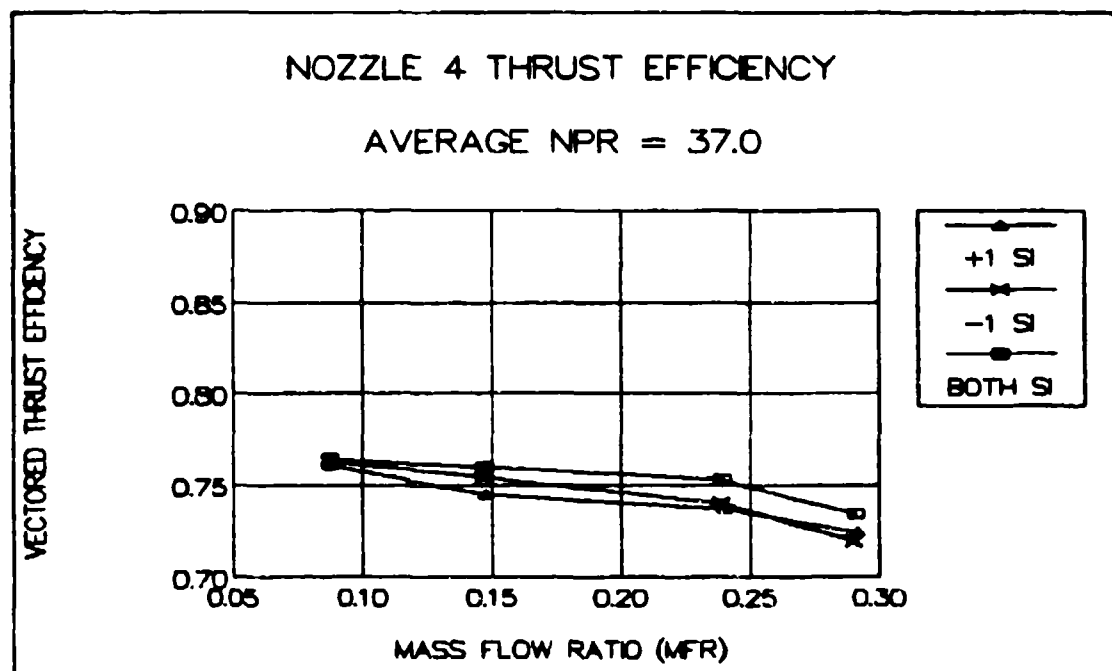


Fig 39 Nozzle 4 Thrust Efficiencies
(with secondary flow)

Table 4. Nozzle Thrust Efficiencies with Secondary Flow

NOZZLE	+1 SI	-1 SI	BOTH SI
1	0.780 \pm 0.013	0.778 \pm 0.0006	0.774 \pm 0.0009
2	0.767 \pm 0.012	0.769 \pm 0.019	0.770 \pm 0.018
3	0.775 \pm 0.009	0.771 \pm 0.010	0.793 \pm 0.015
4	0.742 \pm 0.013	0.744 \pm 0.017	0.753 \pm 0.012

secondary flow interactions, it is also of interest to consider the ratio of the secondary flow momentum to the primary flow momentum (R_M). Appendix B includes the equations and sample calculations for determining values of G_M and R_M .

Figures 40 through 43 show the values of G_M and R_M at varying MFR for nozzles 1, 2, 3, and 4. R_M increases linearly with increasing MFR, indicating that the secondary velocity is approximately constant.

If the vectored flow were dependent only on the momentum of the secondary flow, one would expect that G_M would increase with increasing R_M . However, the opposite is true for nozzles 1 and 2, indicating that something more than the "brute force" mechanism applies. The trends in Figs 40 and 41 agree with Talda's data that shows side force increasing to a maximum and then decreasing with further increases in MFR (16:54-56).

Nozzles 3 and 4 show very small values of G_M which remain essentially constant with increasing MFR. This is consistent with the poor vectoring performance of these nozzles. As discussed in section III, the existence of an additional secondary flow port on the curved wall of nozzle 3 may prevent the supersonic vectored flow from attaching, thereby leading to low G_M . The use of suction at this secondary port may allow for flow attachment, but that is beyond the scope of this study.

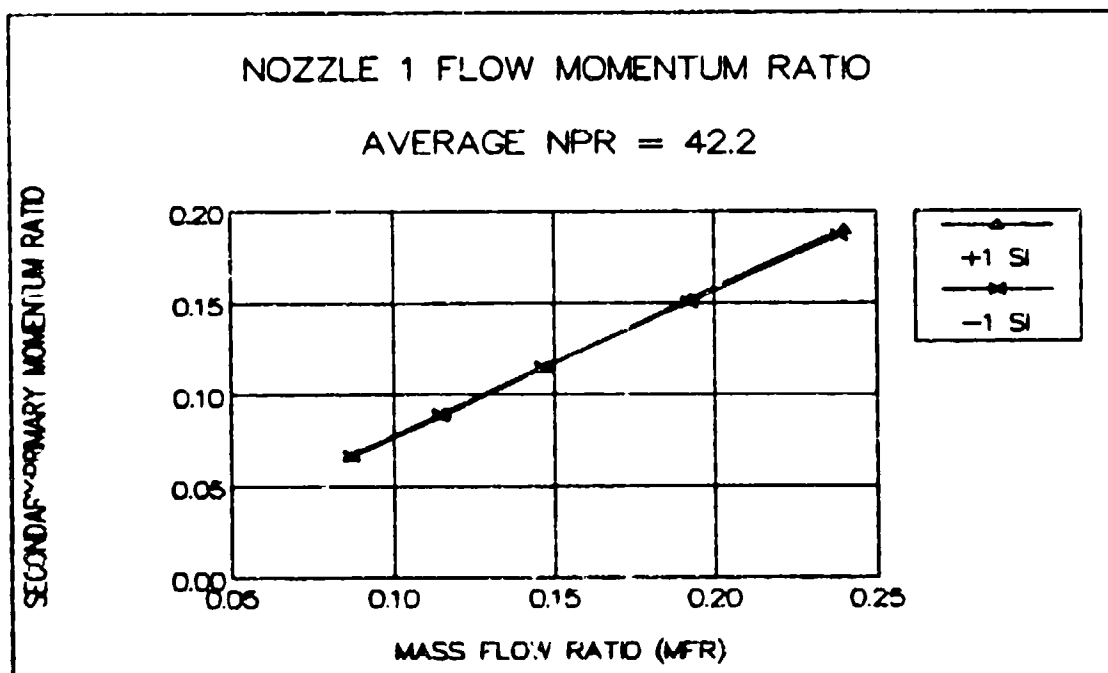
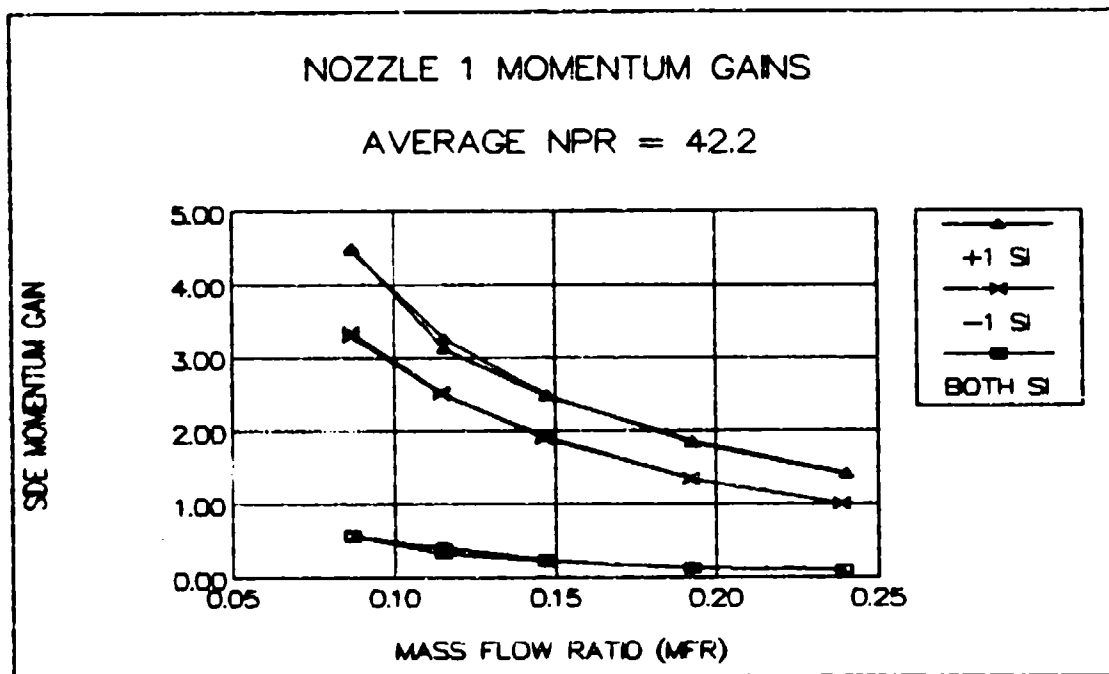


Fig 40 Nozzle 1 Momentum Gains and Flow
Momentum Ratios

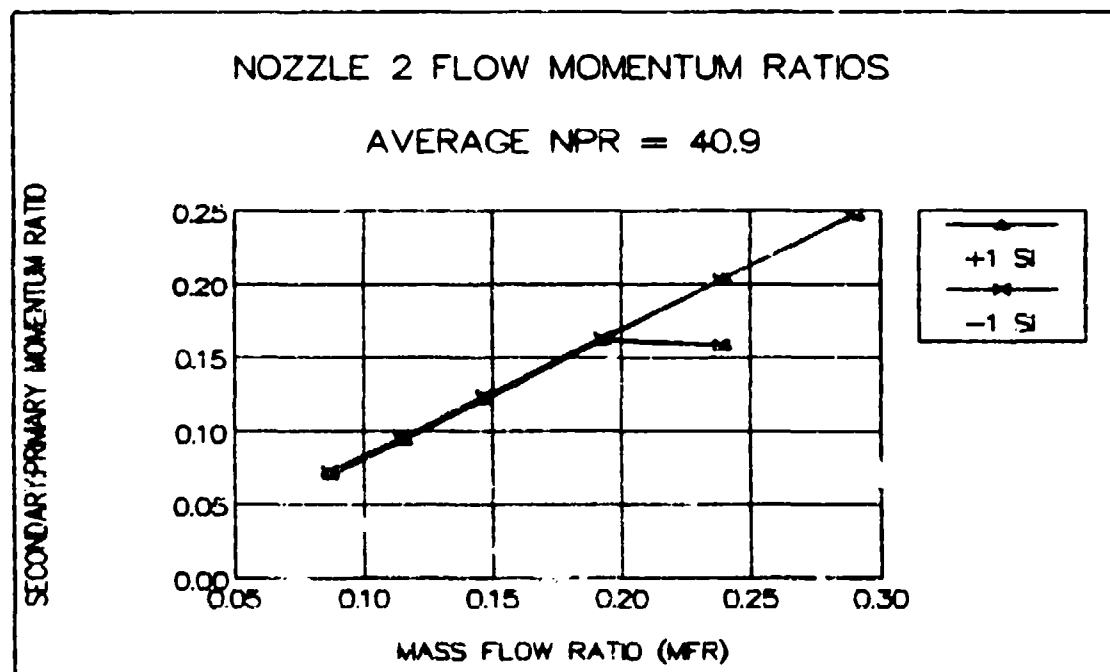
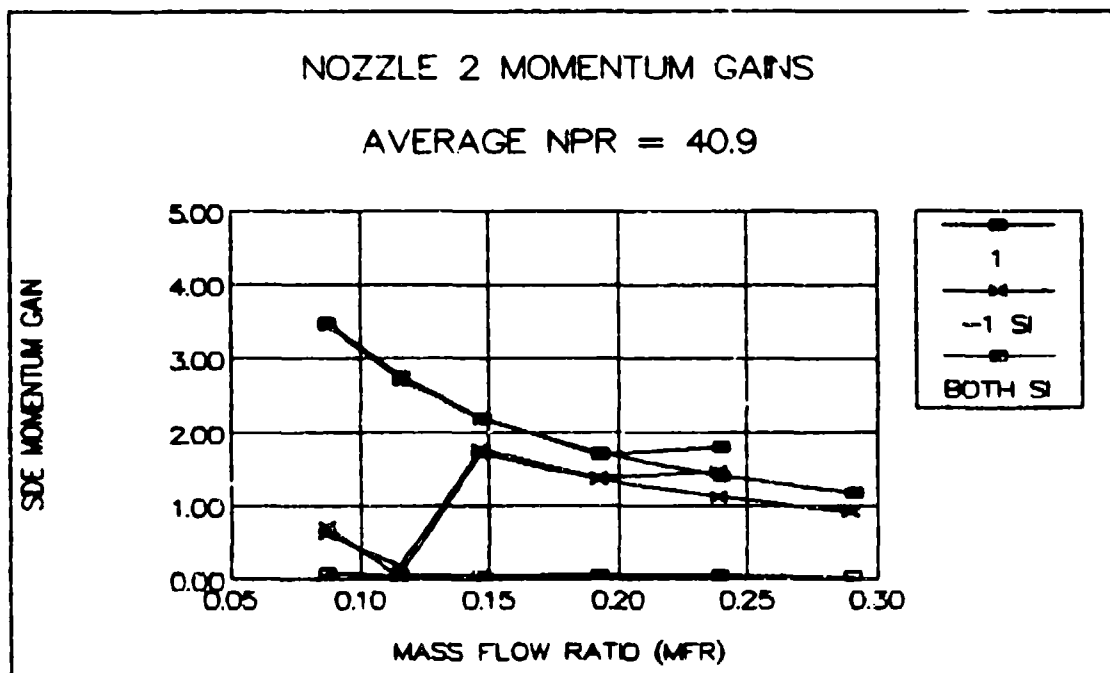


Fig 41 Nozzle 2 Momentum Gains and Flow
Momentum Ratios

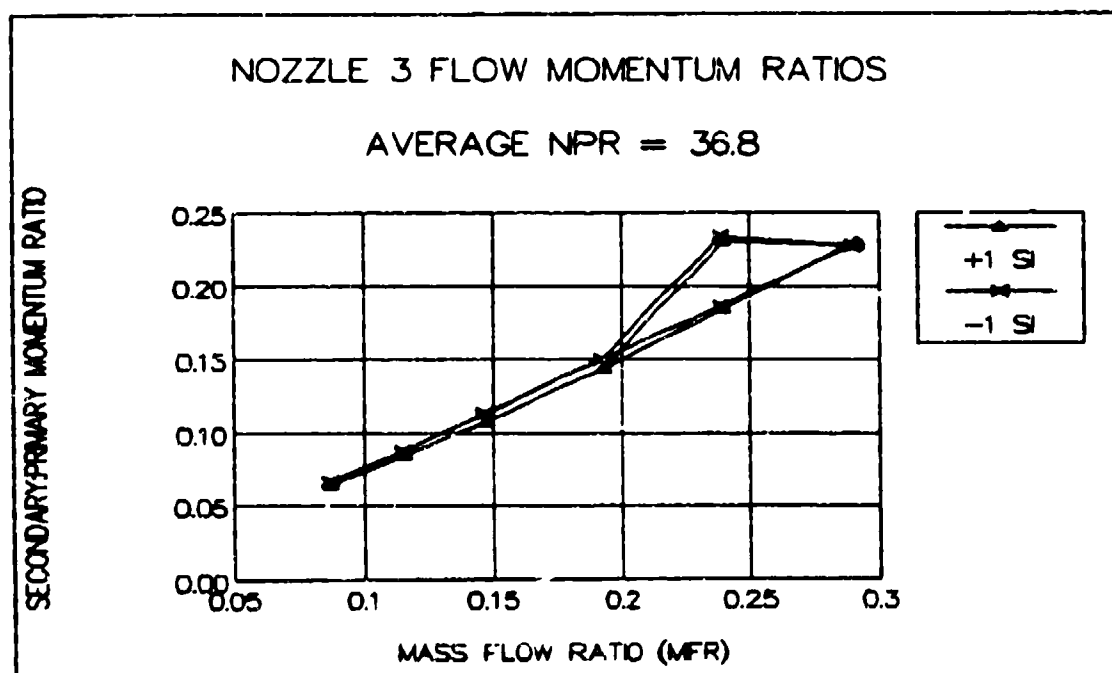
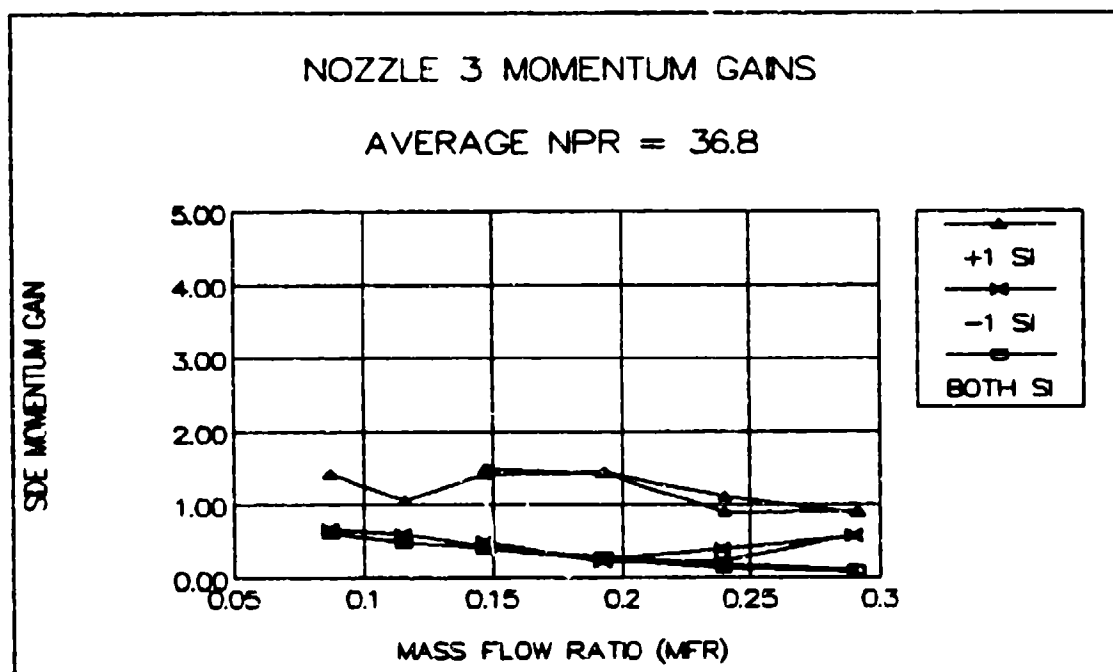


Fig 42 Nozzle 3 Momentum Gains and Flow
Momentum Ratios

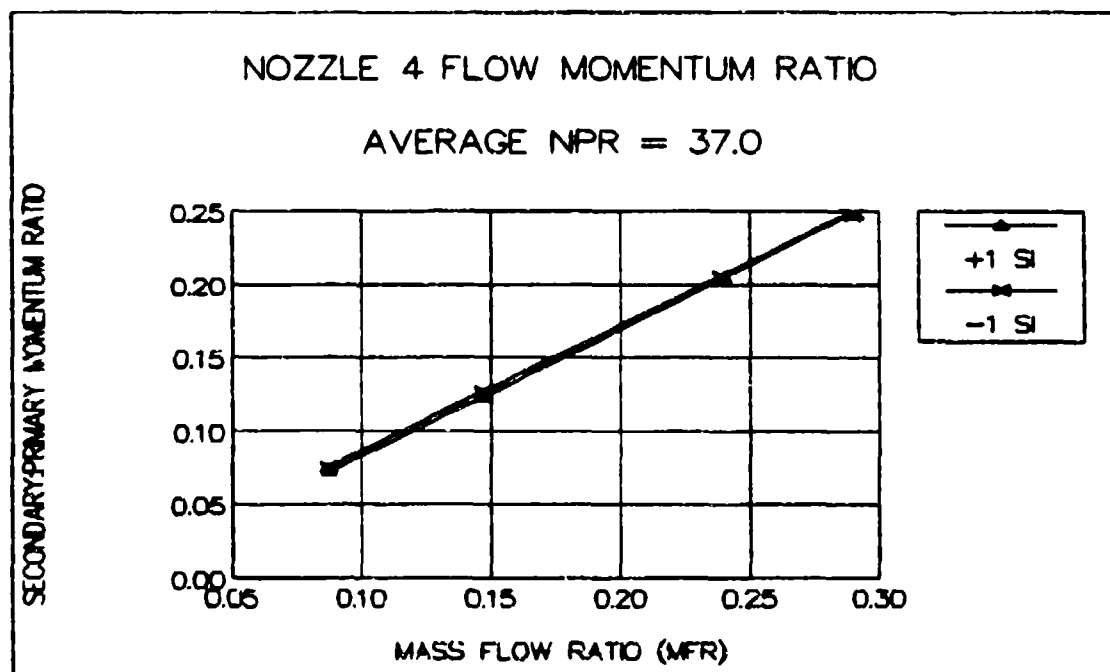
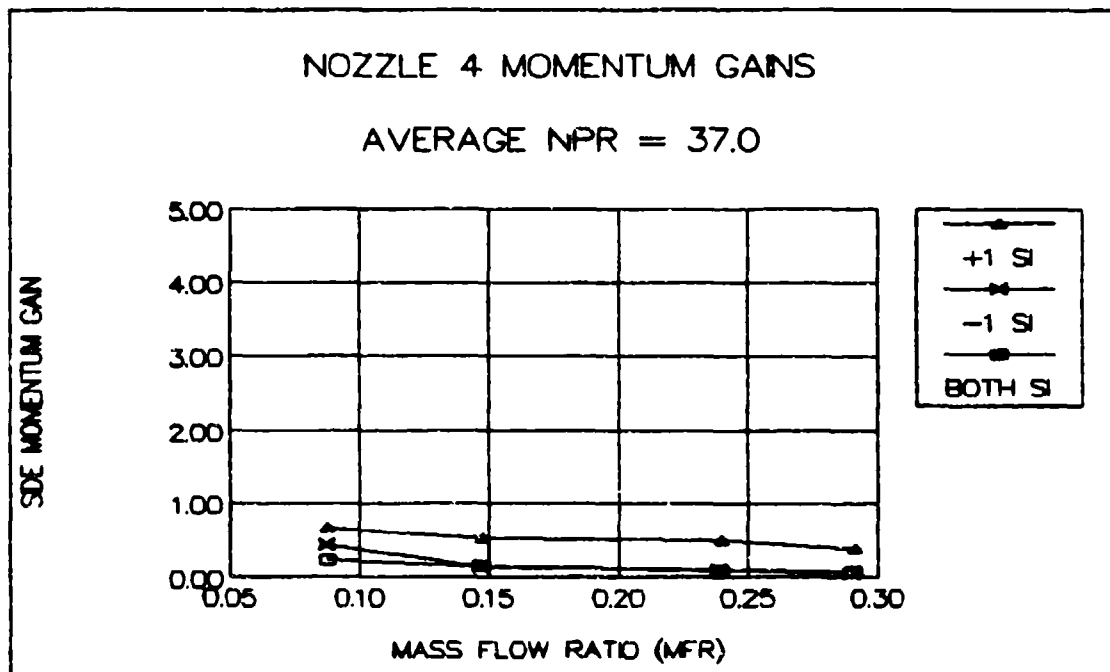


Fig 43 Nozzle 4 Momentum Gains and Flow
Momentum Ratios

Static Pressure Profiles

Figures 44 through 46 show the centerline static pressures for nozzles 1, 2, 3, and 4 measured at the best vector range condition for each nozzle as listed in Table 3. These figures can be compared with Fig 23 which provides the centerline static pressure profile for nozzles with no secondary flow.

Figures 44 and 45 are the pressure profiles for secondary flow from only one nozzle wall. As expected, these two figures are almost identical. The vectored flow profiles for nozzle 1 differ from its profile with no secondary flow, as illustrated in Fig 23. Both profiles show sharp pressure rise close to the secondary flow port, but the pressure rise for the vectored case occurs closer to the throat. The pressure values after the sharp rise drop slightly and then remain essentially constant until an expansion is required at the exit. The difference in the pressure rise location between the cases with and without secondary flow is consistent with the mechanism previously illustrated in Fig 16. The introduction of secondary flow raises the static pressure in the area behind the oblique shocks in the nozzle diverging section. This change in flow conditions causes the oblique shock angle to increase, which in turn causes the centerline pressure rise due to the shock to move closer to the throat, as observed. The nozzle 2 static pressure profile is similar to the nozzle 1 profile, except it has slightly higher values. The higher values

SUMMARY OF NOZZLE CENTERLINE PRESSURES

WITH SECONDARY INJECTION (+1 SI)

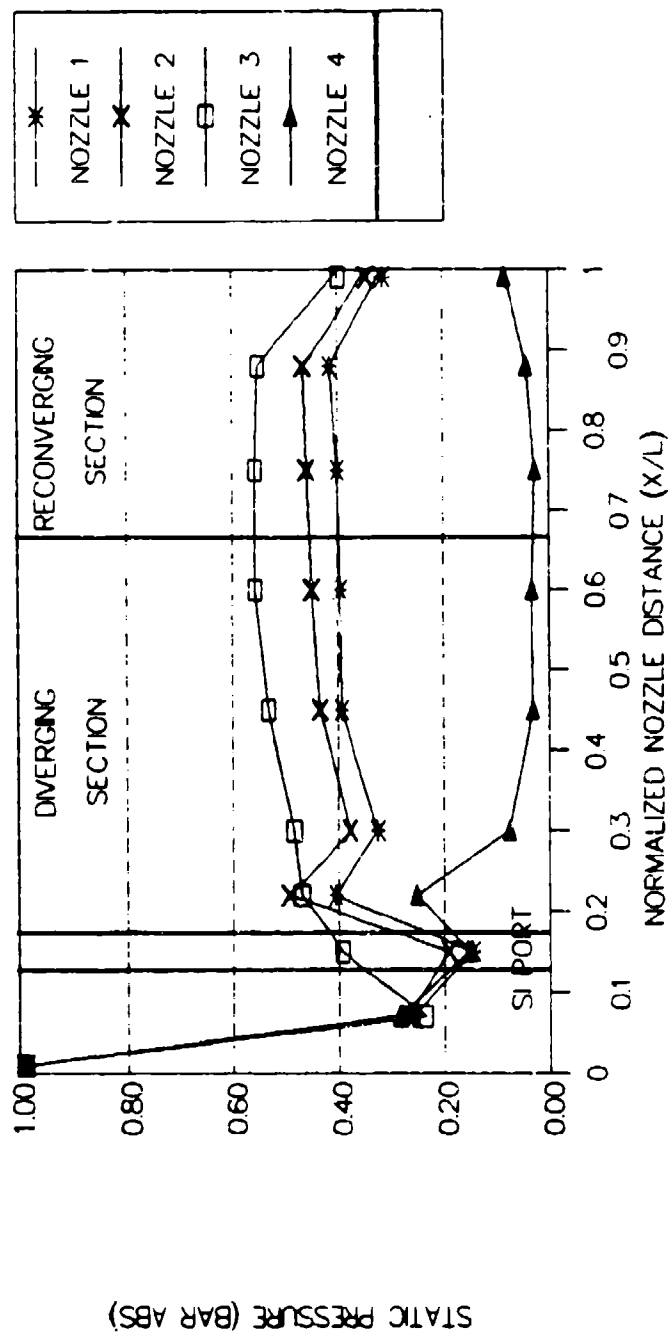


Fig 44 Summary of Nozzle Centerline Pressures at

Maximum Vector Angle Range (Average NPR = 40.5 ± 2.0)

SUMMARY OF NOZZLE CENTERLINE PRESSURES

WITH SECONDARY INJECTION (-1 SI)

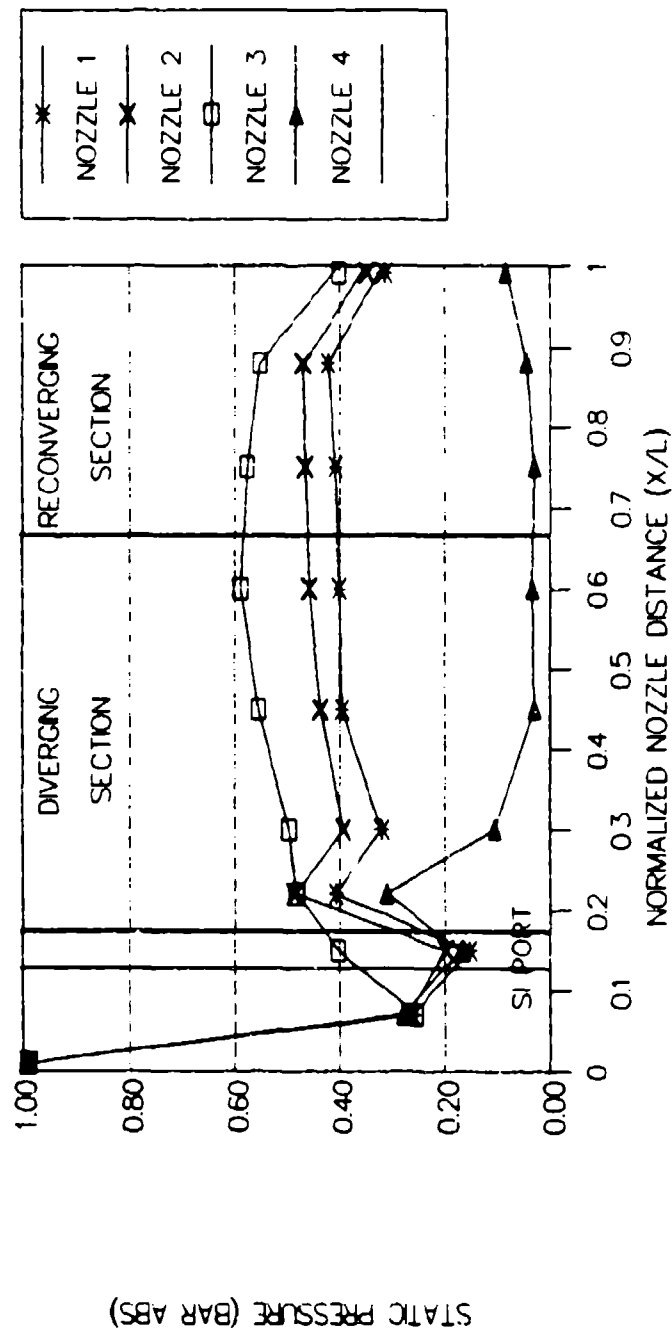


Fig 45 Summary of Nozzle Centerline Pressures at

Maximum Vector Angle Range (Average NPR = 39.6 ± 2.1)

reflect the higher secondary flow pressures required for the maximum vector range for nozzle 2.

For the case with no secondary flow, the profile for nozzle 3 was essentially the same as that for nozzle 1. With secondary flow, the profiles are different in that nozzle 3 has a more gradual pressure rise in the diverging section than nozzles 1 and 2. The nozzle 3 pressure profile also has slightly higher values than that for nozzle 2, which reflects its higher secondary flow pressure requirements for maximum vector range.

The pressure profiles with secondary flow for nozzle 4 show abrupt pressure rises similar to the rises in nozzles 1 and 2. These rises occur immediately downstream of the secondary flow ports. Since a similar pressure rise did not occur in the profile with no secondary flow, it appears that the introduction of secondary flow into nozzle 4 produces a shock.

Figure 46 shows the pressure profiles for when secondary flow is applied from both nozzle walls. The profiles with both secondary flows are similar to the profiles with single side secondary flows for all nozzles at x/L values between 0.3 and 1.0. The profiles for both secondary flows have higher pressure values, consistent with the resulting higher mass flow. Some changes are evident in the area around the secondary injection ports. When secondary flows from both walls are introduced, all nozzles have abrupt pressure rises which occur closer to the nozzle throat than they did for

SUMMARY OF NOZZLE CENTERLINE PRESSURES

WITH SECONDARY INJECTION (BOTH SI)

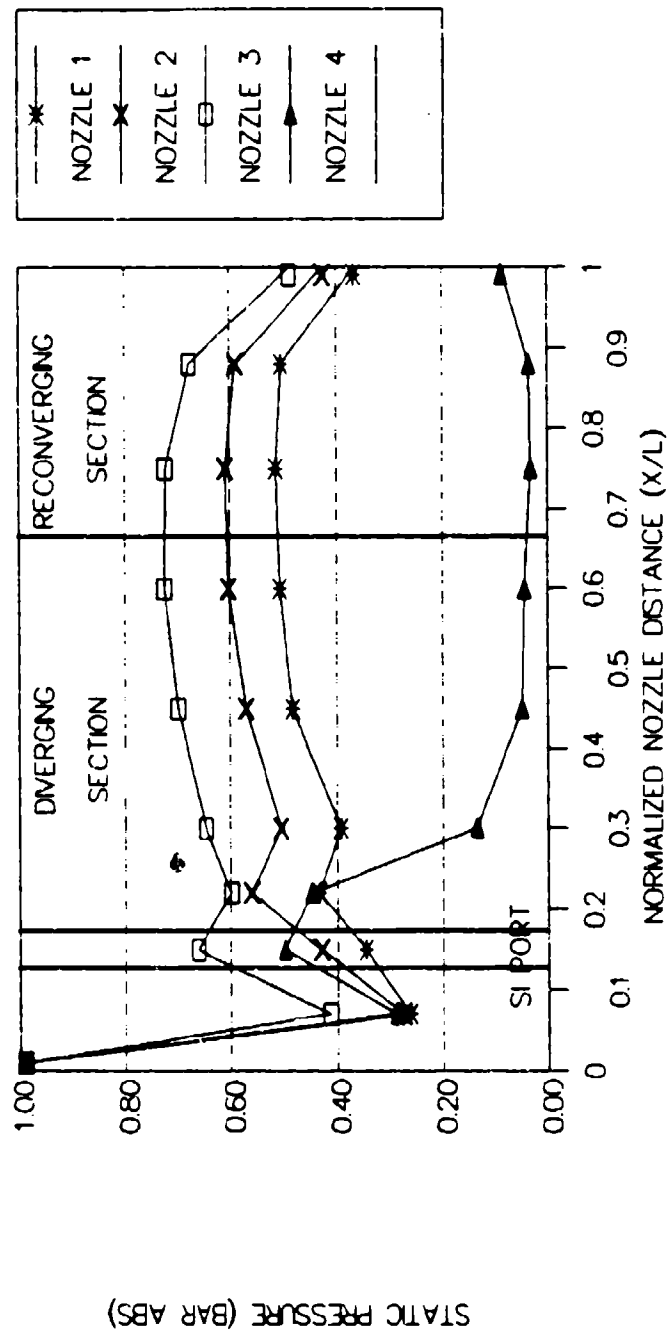


Fig 46 Summary of Nozzle Centerline Pressures at
Maximum Vector Angle Range (Average NPR = 39.0 ± 1.8)

the cases of secondary flow being introduced from only one wall. This is consistent with the formation of normal shock or Mach reflection in the diverging portion of the nozzle previously illustrated in Fig 16.

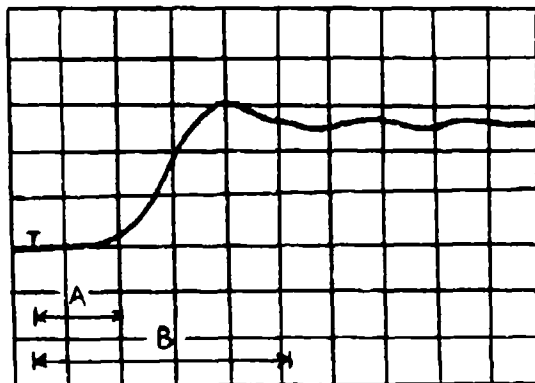
In summary, the centerline static pressure profiles for cases of secondary flow from either one or both nozzle walls confirm the previously discussed flow visualization observations.

Nozzle Switching Response

The force and vectoring angle performance of CJTVC nozzles have been discussed. If a thrust vectoring nozzle is to be used as some form of vehicle guidance, its switching response time must also be known. The switching response time is the time required for a change in secondary flow to create a change in the nozzle exit flow. These times were measured using a TEKTRONIX model 2430 digital oscilloscope, which simultaneously recorded voltage signals from both side force channels of the VKI 6-component force balance. The oscilloscope started recording data when an outside trigger signal was applied. This trigger signal was provided through the secondary flow solenoid valve controls. After the signal is applied and the data is recorded, the oscilloscope digitizes and displays the signal voltage versus time plot for analysis. Cursor movement on the oscilloscope provides the capability for accurate time measurements.

Although the oscilloscope trigger signal and the solenoid open or close command signal were simultaneously applied, some delay time existed until the secondary flow started or stopped flowing in the nozzle assembly. The delay time consists of the time required for the solenoid valve to open or close once it received the command and the time required for the appropriate flow change to occur in the secondary flow supply lines running to the secondary ports in the nozzle assembly. This delay time was measured by placing an ENDEVCO pressure transducer in the secondary supply line just prior to its entry into the nozzle assembly. The output signal of the transducer was recorded by the oscilloscope when the appropriate solenoid command was given. Figure 47 shows the oscilloscope traces recorded by a pen plotter for solenoid open and close commands. Two times were measured for each case. The first time (t_A) was the delay time for the solenoid valve to open or close, which was measured at the point where the transducer voltage slope started to change. The second time (t_B) was the delay time for the secondary pressure to reach steady state. It was measured at the point where the transducer voltage slope leveled off. For the valve open command, $t_A = 25.9$ ms and $t_B = 37.8$ ms, while the valve close command had $t_A = 37.8$ ms and $t_B = 79.8$ ms.

Switching response times were measured from the strain gage voltage signals of the two side force channels of the force balance. Appendix A contains information concerning

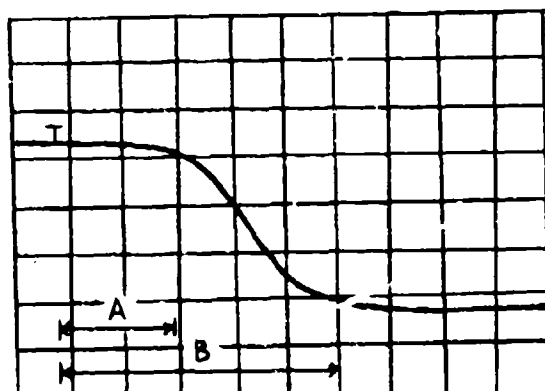


(a) Valve open command
delays

$$t_A = 25.9 \text{ ms}$$

$$t_B = 65.9 \text{ ms}$$

t_A = delay time for solenoid valve to open or close
 t_B = delay time for secondary supply line pressure to
 increase or decrease to steady state



(b) Valve close
command delays

$$t_A = 37.8 \text{ msec}$$

$$t_B = 79.8 \text{ msec}$$

Fig 47 Secondary Flow Response Time Delays

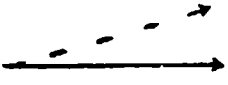
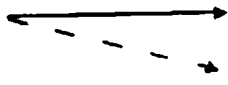

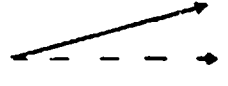


(y-axis divisions = 50 mV; x-axis divisions = 20 ms)

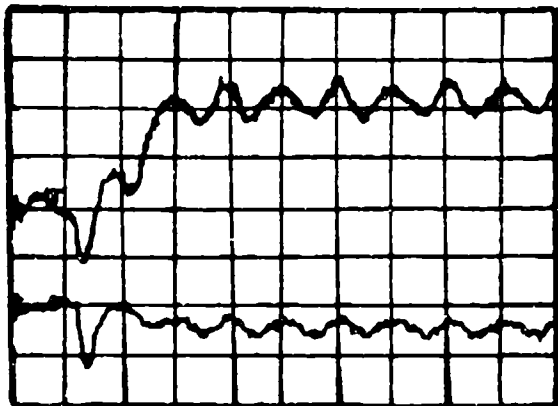
the location of these strain gages. Time restrictions only allowed one nozzle configuration to be tested. Nozzle 1 was selected since it had the best vectored thrust efficiencies and momentum gains of the CJTVC nozzles. Response times for six different switching cases were measured. The secondary flow conditions before and after the appropriate solenoid command for each case are summarized in Table 5. Response times for each case were measured using MFR values of 0.087, 0.115, and 0.147.

Figures 48 and 49 are typical voltage versus time plots for the six test cases. The traces show the voltage for each channel just before the trigger signal is received and the resulting change in side force voltages from the change in secondary flow. When the side force voltages change magnitude, they start to oscillate at a frequency of approximately 19 Hz. To investigate this oscillation, an impulse was applied to the 6-component balance with its voltage output being input to a Hewlett-Packard Model 3582A spectrum analyzer. The resulting power spectral density plots showed a spike at 19.2 Hz after the impulse was applied which was not present before the impulse was applied. This was repeated several times with the same result, thereby confirming that the side force oscillations in Figs 48 and 49 are due to the natural frequency of the force balance.

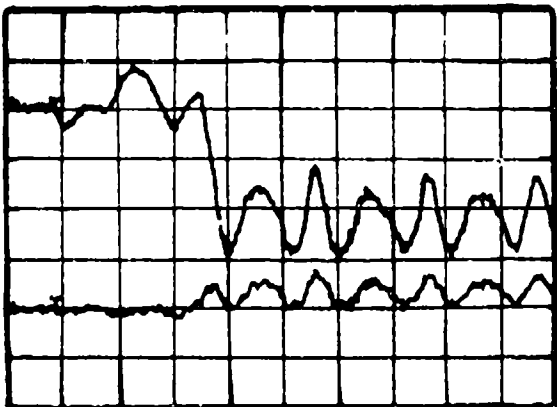
Response times were measured from the trigger signal indication point to the point where the side force channel

Table 5. Nozzle Flow Vectoring Response Time Test
Conditions

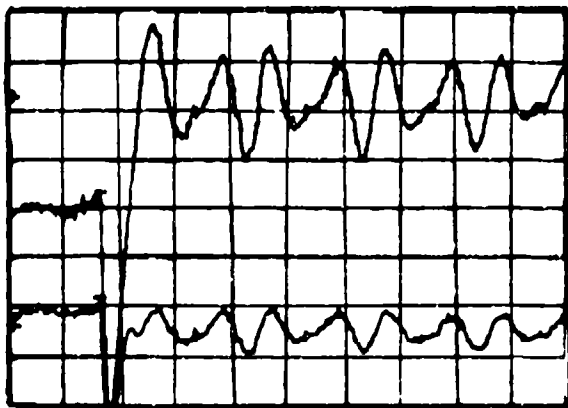
Test Case	Flow Condition Before Solenoid Command	Solenoid Valve Command	Nozzle Exit Flow Direction — Before Command --- After Command
1	Both secondary flows applied	Close valve to lower wall secondary flow	
2	Both secondary flows applied	Close valve to upper wall secondary flow	
3	Lower wall secondary flow applied	Open valve to upper wall secondary flow	
4	Upper wall secondary flow applied	Open valve to lower wall secondary flow	
5	Lower wall secondary flow applied	Simultaneously close valve to lower secondary flow and open valve to upper secondary flow	
6	Upper wall secondary flow applied	Simultaneously close valve to upper secondary flow and open valve to lower secondary flow	



Test Case 1



Test Case 2



Test Case 3

Fig 48 Nozzle 1 Side Force Oscilloscope Traces

Test Cases 1-3

(CMFR = 0.087; y-axis divisions = 50 mV; x-axis divisions = 50 ms; side force channel 1 is top trace; side force channel 2 is bottom trace)

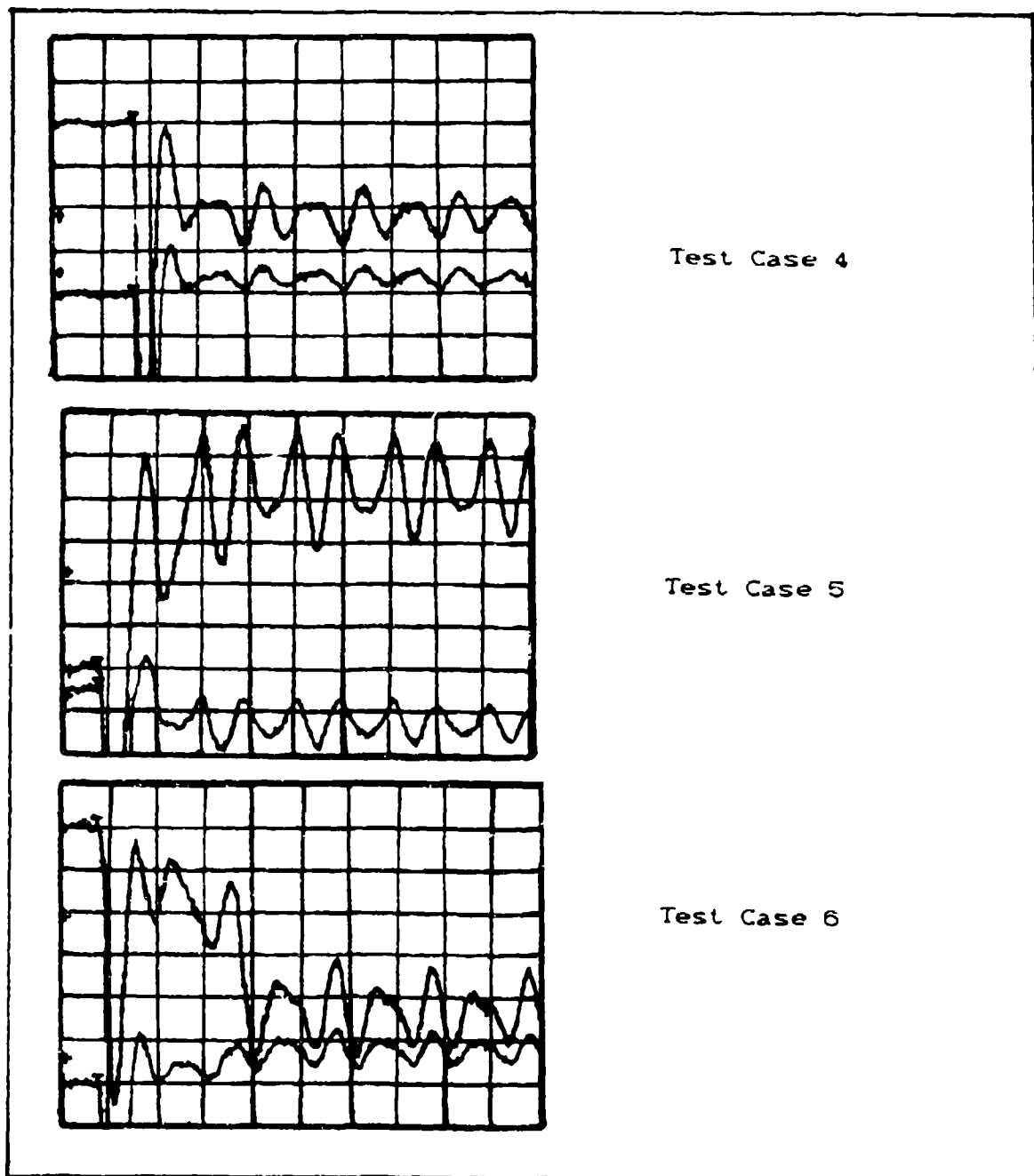


Fig 49 Nozzle 1 Side Force Oscilloscope Traces

Test Cases 4-6

(CMFR = 0.087; y-axis divisions = 50 mV; x-axis divisions = 50 msec; side force channel 1 is top trace; side force channel 2 is bottom trace)

traces begin a repeatable oscillation pattern. The appropriate solenoid valve command and pressure change delay times were subtracted from these times. The resulting times represent (1) the response time from when the solenoid valve opens or closes until the side forces change and (2) the response time from when the secondary flow reaches its supply line pressure until the side forces change. Table 6 presents these response time values for the test cases and MFRs previously mentioned. A MFR of 0.115 produces the shortest response times for test cases 1 and 2. For test cases 3 and 4, the response times (t_R) produced by MFRs of 0.087 and 0.115 are approximately equal, and are much lower than the times for an MFR of 0.147. Response times for test cases 5 and 6 are shortest for an MFR of 0.147. No consistent trends between MFR values and response times are obvious. The response frequencies (f_R) for nozzle 1 at its best vector range MFR of 0.087 vary between 7.13 and 23.3 Hz when measured from solenoid valve opening or closing and vary between 10.2 to 333.3 Hz when measured from the point when supply line pressure is achieved at the secondary port.

Summary

Table 7 summarizes all of the performance parameters presented in this section for test nozzles at the MFR that produced the largest vector angles. As previously discussed, nozzle 1 is superior in all aspects tested except for thrust efficiency with secondary flow from both walls.

Table 6. Nozzle 1 Flow Vectoring Response Times
and Frequencies

Test Case	Delay time	MFR=0.087		MFR=0.115		MFR=0.147	
		t_R (ms)	f_R (Hz)	t_R (ms)	f_R (Hz)	t_R (ms)	f_R (Hz)
1	t_A	72.8	13.7	69.5	14.4	92.0	10.9
	t_B	30.8	32.5	27.5	36.4	70.0	14.3
2	t_A	112.7	8.9	77.8	12.9	101.0	9.9
	t_B	80.7	12.4	35.8	27.9	59.0	16.9
3	t_A	43.0	23.3	45.5	22.0	87.5	11.4
	t_B	3.0	333.3	5.5	181.8	27.5	26.7
4	t_A	45.3	22.1	45.0	22.2	85.0	11.8
	t_B	5.3	188.7	5.0	200.0	45.0	22.2
5	t_A	74.5	13.4	79.3	12.6	49.0	20.4
	t_B	32.5	30.8	37.3	26.8	7.0	142.9
6	t_A	140.2	7.1	82.8	12.1	78.5	12.7
	t_B	98.2	10.2	40.8	24.5	36.5	27.4

Table 7 Summary of Nozzle Best Vector Range Performance

Nozzle	MFR for Best Vector Range	Best Vector Angle Range	Best Momentum Gain		Efficiencies @ Best MFR		
			+1	-1	+1	-1	2
1	0.087	33.1	4.50	3.35	0.794	0.784	0.786
2	0.193	29.5	1.72	1.38	0.767	0.777	0.765
3	0.291	18.3	0.91	0.58	0.783	0.784	0.797
4	0.239	7.4	0.5	0.1	0.737	0.740	0.753

+1 = upper wall secondary flow applied

-1 = lower wall secondary flow applied

2 = both walls secondary flow applied

However, its thrust efficiency for this case is only 1.4 percent less than the best efficiency for the same case.

Again, since the tested parameters for nozzle 1 showed it to have the best overall performance, its external flow patterns were photographed using schlieren techniques. Figure 50 is a composite of these photographs for MFR values of 0.087, 0.115, 0.147, and 0.239. For each MFR, there are three photographs, one for each flow condition (secondary flow from upper wall, secondary flow from both walls, secondary flow from lower wall). The horizontal line in each photograph is a reference line drawn perpendicular to the nozzle exit, thereby indicating the zero degree flow angle.

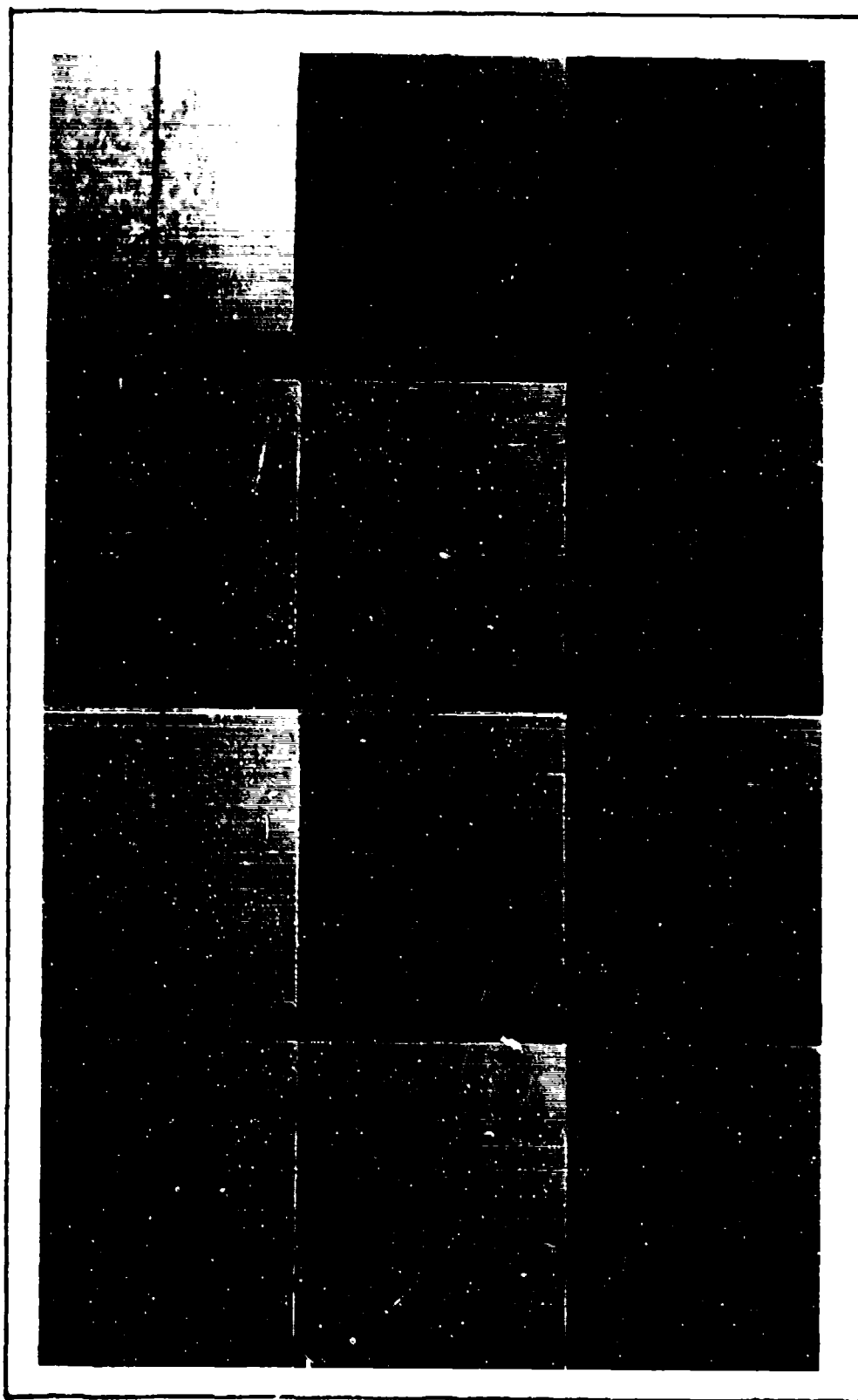


Fig 50 Nozzle 1 External Flow Schlieren Photographs

V. Nozzle Analytical Model Results

The previous sections of this report have described the results of operating mechanism and performance tests. This section deals with attempts to analytically model nozzle performance. Several existing models are presented for predicting the side force to axial force ratio. The author presents a successful model for predicting the nozzle total thrust.

Viscous Effects Analysis

Before any simple analytical modeling is considered, it is important to determine if viscous effects in the nozzle should be considered. Boundary layer thickness will reach its maximum value before the flow separates from the nozzle wall in its diverging section. Since previous discussions in this report indicate that flow separation occurs near the secondary flow ports, the value of boundary layer thickness will be calculated at this point.

Both length and hydraulic diameter-based Reynolds number calculations predict turbulent flow at the secondary points. The walls in the diverging section prior to the secondary ports are flat. Therefore, the following equation for the boundary layer from turbulent flow over a flat plate is used:

$$\delta_t(x) = 0.37 \times \left[\frac{u_\infty x}{\nu} \right]^{-0.2} \quad (1)$$

where δ_t is the boundary layer thickness, x is the length along the flat plate, u_∞ is the flow velocity, and ν is the flow kinematic viscosity (13:638). Using the same model, the displacement thickness, δ_1 , and the momentum, δ_2 , can be calculated:

$$\delta_1 = 0.125 \delta_t \quad (2)$$

$$\delta_2 = 0.097 \delta_t \quad (3)$$

where the displacement thickness is a measure of the displacement of the flow resulting from the presence of the flat plate and its boundary layer. The momentum thickness is the measure of the momentum flux decrement caused by the boundary layer (10:50).

Assuming isentropic flow up to the secondary port, the resulting values were $\delta_t = 0.00548$ in, $\delta_1 = 0.00069$ in, and $\delta_2 = 0.00053$ in. Considering the nozzle dimensions at the secondary port, these values show the calculated boundary layer value is 2.1 percent of the nozzle height and 2.2 percent of the nozzle width. Therefore, it occupies 8.5 percent of the nozzle area. Since these values are relatively small, further consideration of the boundary layer thickness was not included in the analytical models. Detailed boundary layer sample calculations are included in Appendix B.

Side Force to Axial Force Ratio Models

Several prediction models for side force to axial force

ratios for TVC nozzles have been developed from experimental results. Zukoski and Spaid proposed a model which had the side to axial force ratio varying directly with the ratio of secondary mass flow to primary mass flow (20:1696). The results of section IV of this report indicate that this model is not applicable.

Broadwell developed a model using blast wave theory that accounts for secondary flow momentum deficit and volume addition effects. His side to axial force ratio equation is:

$$\frac{F_S}{F_A} = 1.2 \alpha(\gamma) M_\infty \frac{V_\infty}{V_{ex}} \left[1 + \frac{2 + (\gamma - 1) M_\infty^2}{2(\gamma - 1) M_\infty^2} \frac{T_{ti}}{T_{t\infty}} \right] \sin \beta \left(\frac{m_i}{m_p} \right) + \frac{V_i}{V_{ex}} \sin \alpha \left(\frac{m_i}{m_p} \right) \quad (4)$$

where $\alpha(\gamma)$ is an energy term defined by Broadwell, M_∞ , V_∞ , and $T_{t\infty}$ are the primary flow Mach number, velocity, and total temperature at the secondary port, γ is the specific heat ratio for the primary flow, V_{ex} is the effective secondary exhaust velocity to vacuum, V_i is the effective secondary exhaust velocity, T_{ti} is the secondary flow total temperature, m_p and m_i are the primary and secondary mass flow rates, α is the angle between the secondary and primary axes, and β is the angle between a line normal to the nozzle wall at the secondary port and the primary axis (3:1071).

By considering the rates of change of primary flow momentum and secondary flow momentum along with experimental results, Green and McCullough developed a model for fluid injection thrust vector control. Their side to axial force ratio equation is:

$$\frac{F_S}{F_A} = C_1 \left[\frac{w_1}{w_p} \right]^{0.5} \left[\frac{1}{I_{sp}} \right]^{0.5} \left[\Delta p_1 \right]^{0.25} \quad (5)$$

where w_1 and w_p are the secondary and primary weight flow rates, I_{sp} is specific impulse, Δp_1 is the secondary flow difference between supply and exit, and C_1 is an empirical constant (9:577). For constant mass flow and thrust, specific impulse is defined as:

$$I_{sp} = \frac{F_t}{w_t} \quad (6)$$

where F_t is total thrust and w_t is total weight flow rate (15:22).

Figures 51 through 54 show the relation between the differences between the measured side to axial force ratios and the ratios as modeled by the Broadwell and Green/McCullough equations for nozzles 1,2,3, and 4. Appendix B contains sample calculations for these values. For brevity, "Green" appears on the graphs instead of "Green/McCullough". Clearly, the Broadwell model does not

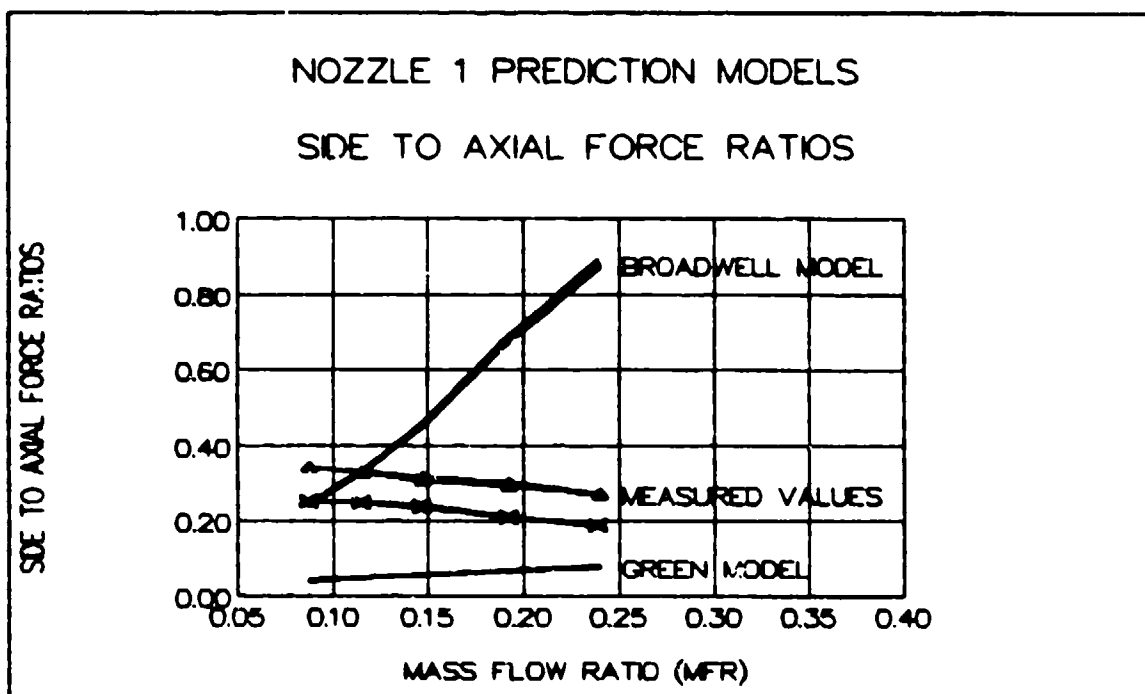


Fig 51 Nozzle 1 Side to Axial Force Ratio
Prediction Results

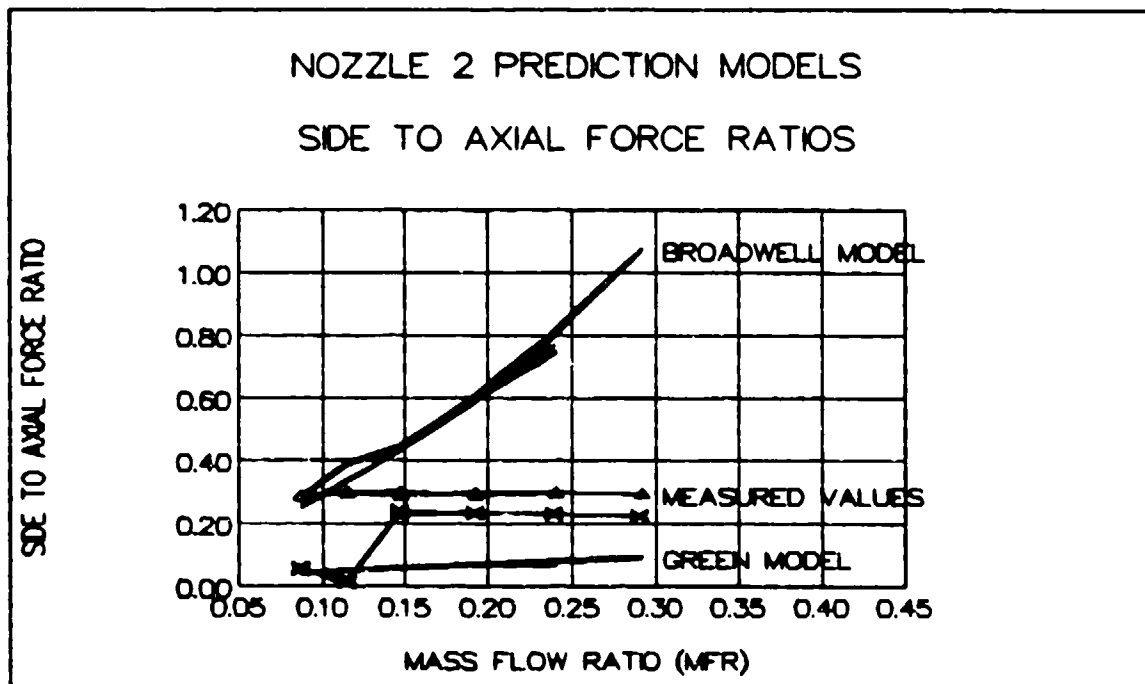


Fig 52 Nozzle 2 Side to Axial Force Ratio
Prediction Results

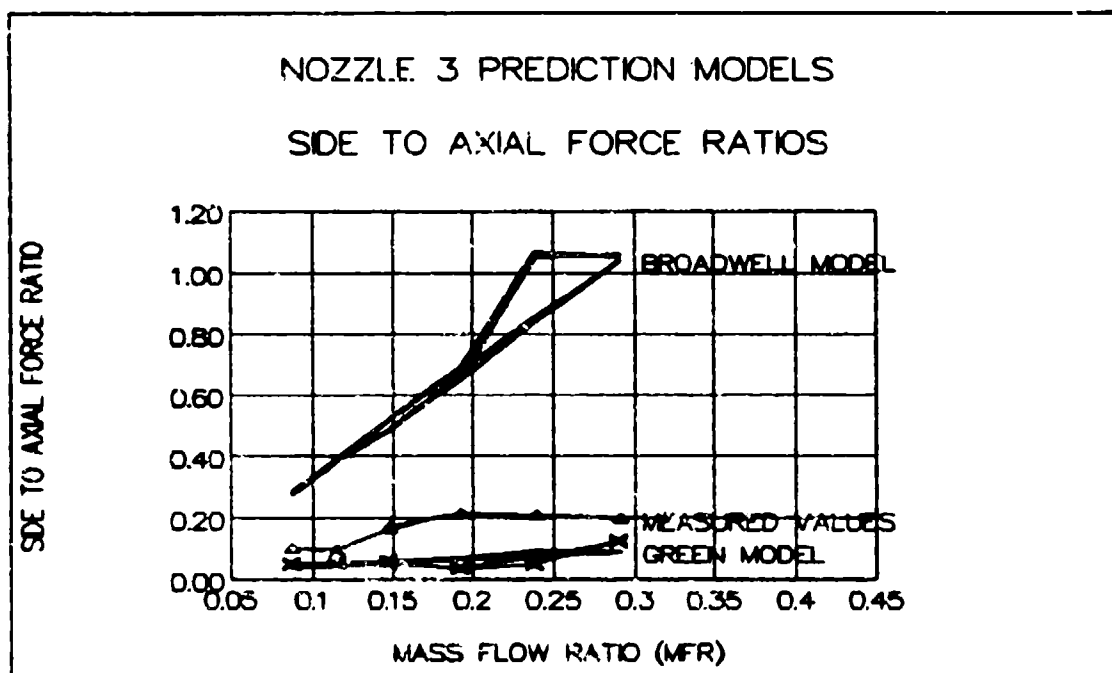


Fig 53 Nozzle 3 Side to Axial Force Ratio
Prediction Results

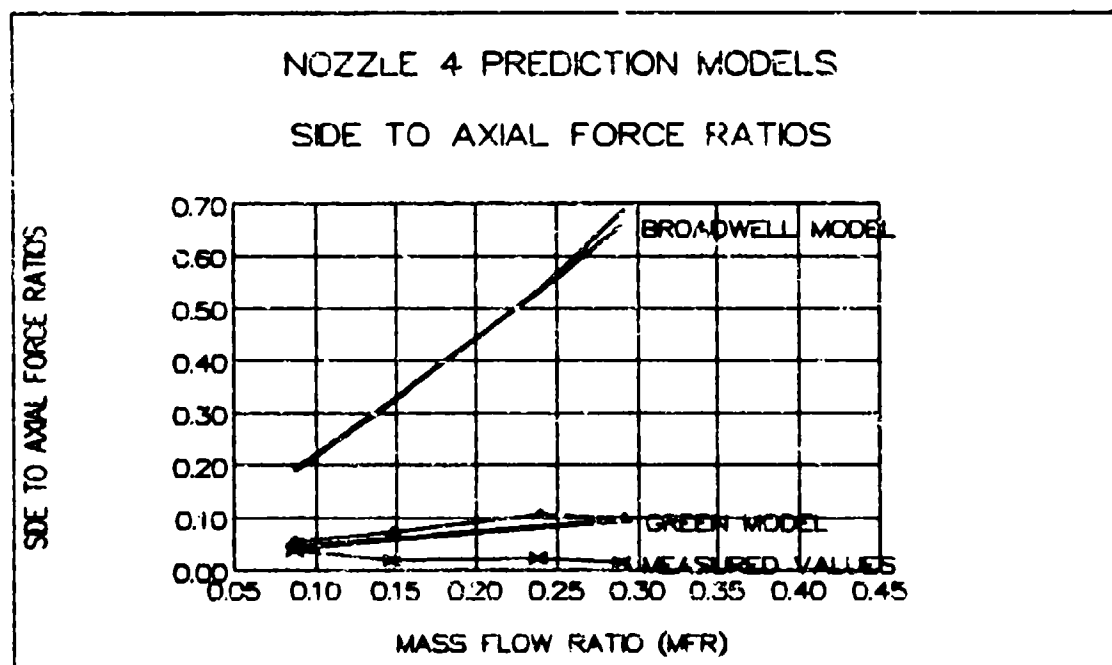


Fig 54 Nozzle 4 Side to Axial Force Ratio
Prediction Results

match the measured data trends. On the other hand, the Green/McCullough model with $C_1 = 1$ does appear to provide some correlation with the measured data. This model requires an empirically derived value for C_1 , which was selected by iteration to be the value that gave the smallest average error from measured data for all vectored flow cases. From observation, some data trends seem to follow the Green/McCullough model, except their values were too large. For these cases it seemed that adding an empirical constant, C_2 , to the Green/McCullough equation (with $C_1 = 1$) might provide better correlation with the measured data than multiplying by the coefficient C_1 . Again, this constant was derived by iteration to produce the lowest error between predicted and measured data. Table 8 lists the resulting coefficients (C_1) and constants (C_2) and their appropriate errors for each nozzle. Figures 55 through 58 graphically illustrate the correlation between the measured and modeled data. For nozzles 1 and 2, the average errors for using C_2 (17.3 and 10.9 percent) were significantly less than the average errors for using C_1 . For nozzles 3 and 4, the average error for using C_1 (26.6 and 28.1 percent) were slightly less than the average errors using C_2 .

Shock Loss Model

Although the Green/McCullough equation can provide an approximate value for side to axial force ratio, it does not provide any information concerning the magnitude of the

Table 8. Average Error from Actual Results for
Green/McCullough Side to Axial Force Prediction Model

Nozzle	Model Coefficient C_1	Error using Model with Coefficient	Model Constant C_2	Error using Model with Constant
1	4.29	29.9	0.200	17.3
2 *	3.71	18.3	0.218	10.9
3 *	1.44	26.6	0.039	28.1
4 *	0.69	80.7	0.029	81.1

* data for non-vectorized cases not considered

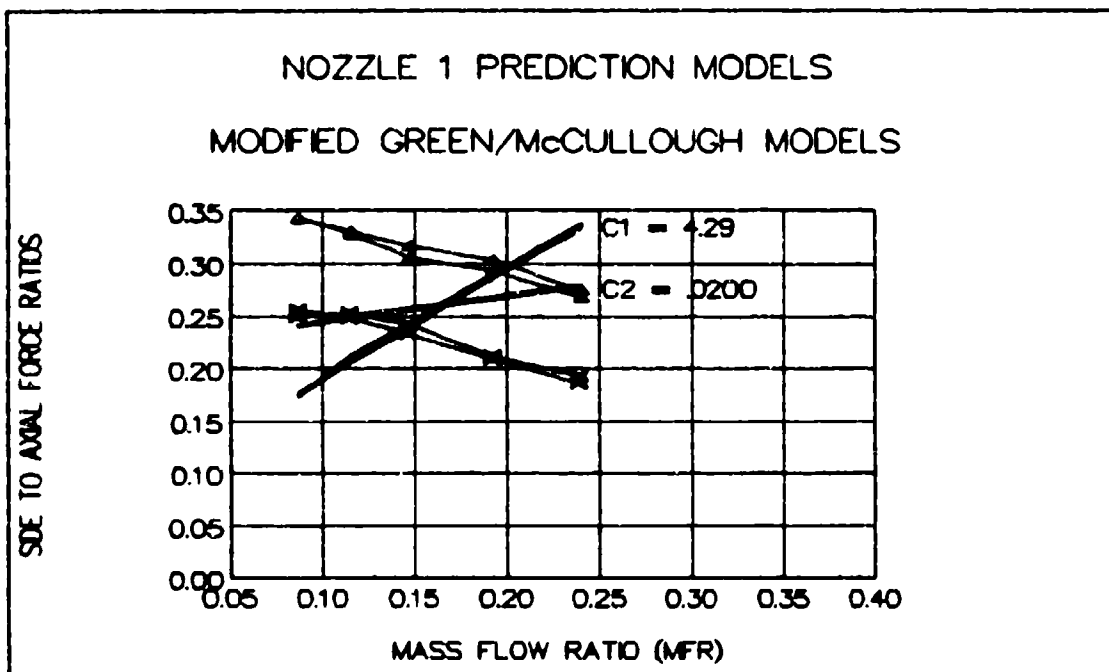


Fig 55 Nozzle 1 Side to Axial Force Ratio Prediction
Results with Modified Green/McCullough Model

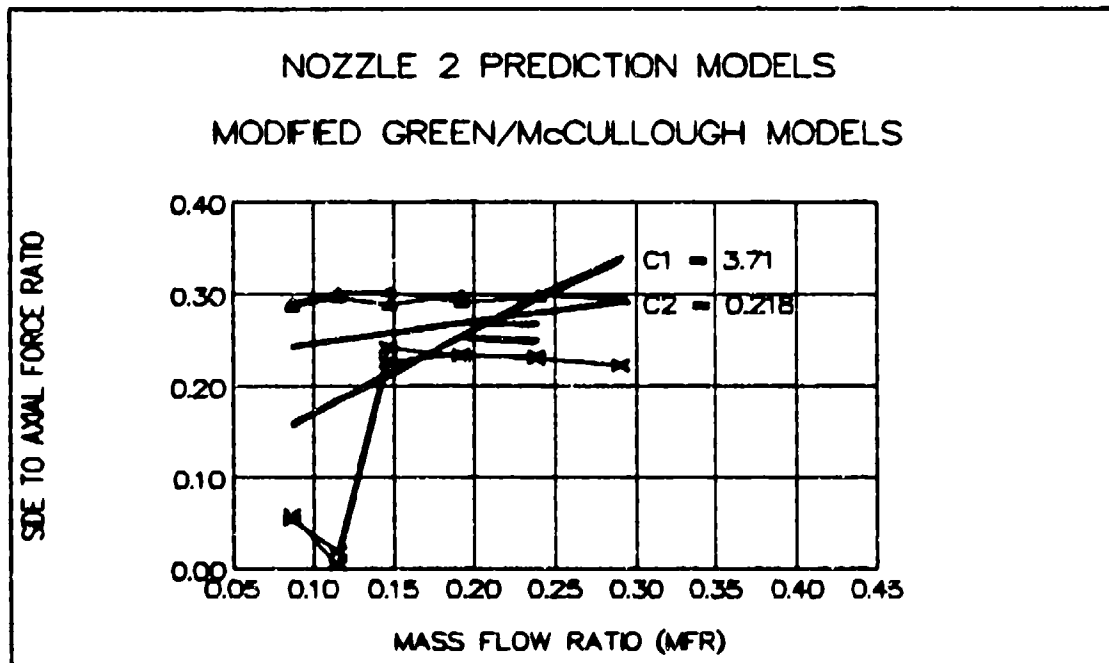


Fig 56 Nozzle 2 Side to Axial Force Ratio Prediction
Results with Modified Green/McCullough Model

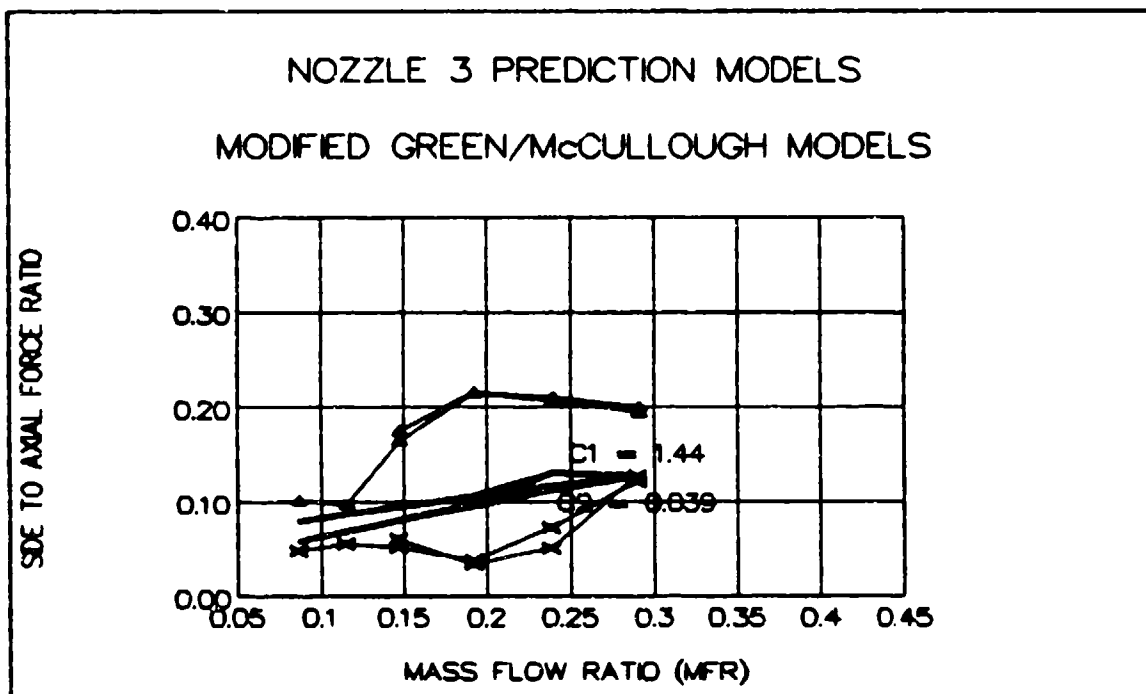


Fig 57 Nozzle 3 Side to Axial Force Ratio Prediction
Results with Modified Green/McCullough Model

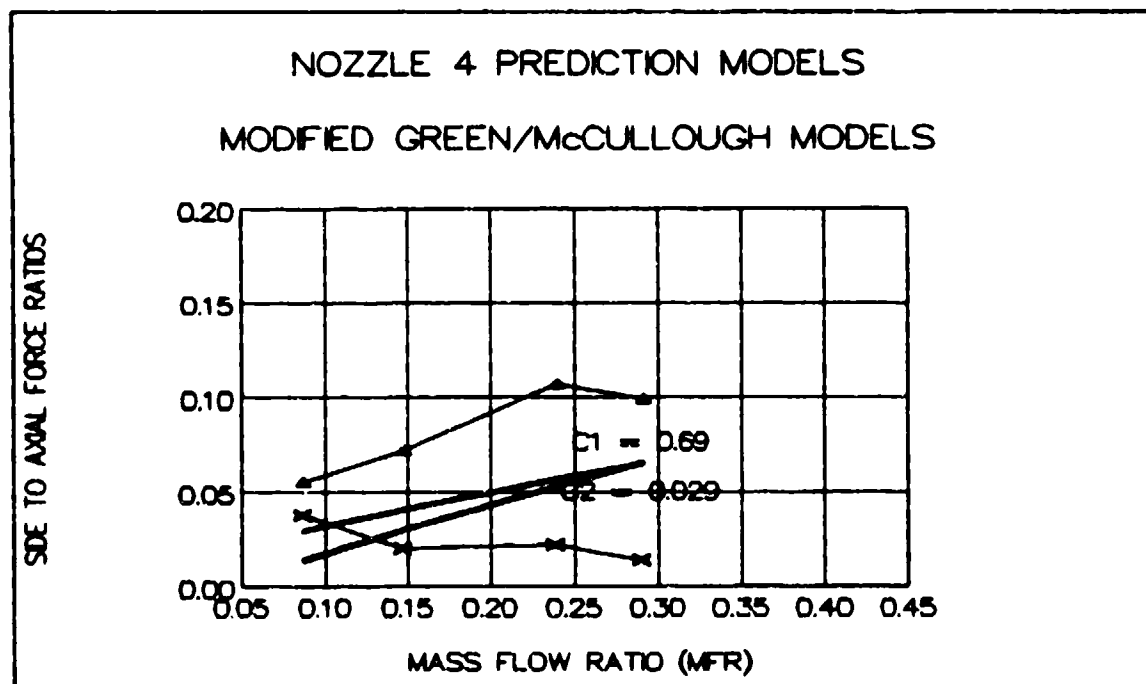


Fig 58 Nozzle 4 Side to Axial Force Ratio Prediction
Results with Modified Green/McCullough Model

forces that the nozzle produces. Earlier calculations of thrust efficiencies in section IV of this report show that ideal thrust equations do not always provide accurate values of the actual nozzle thrust. In order to be able to predict the nozzle total thrust, the author has developed a model which calculates a loss ratio for total pressure used to determine a nozzle exit velocity which is applied to the thrust equation. For this simple model, other losses such as those due to wall friction are not considered. The following paragraphs describe the development of this model.

The thrust equation for a nozzle can be written as:

$$F_t = (m_s + m_p) V_e + (P_e - P_a) A_e \quad (7)$$

where F_t is the total thrust, m_s and m_p are the secondary and primary mass flow rates, V_e is the nozzle flow exit velocity, P_e and P_a are the nozzle exit and ambient static pressures, and A_e is the nozzle exit area (15:49). In order to account for the thrust loss due to the radial divergence of streamlines in the nozzle, the value of F_t must be adjusted:

$$F_{t,loss} = \lambda F_t \quad (8)$$

$$\lambda = \frac{1 + \cos \alpha}{2} \quad (9)$$

where λ is the loss coefficient for radial divergence and α is the nozzle half angle of the diverging section, which

equals 20° for all test nozzles for this report (20:233). For this report, all equations except V_e were measured using relatively simple instrumentation. Therefore, the goal of the author's model is to predict the value of V_e and apply it to the thrust equation in order to predict the total thrust of the nozzle.

Standard isentropic equations provide an ideal exit velocity for nozzles (19:238). However, as discussed in section IV of this report, the nozzles tested suffered thrust losses due to internal shocks. If a total pressure ratio for shock loss were determined, the isentropic equation for exit velocity could be used with this ratio to predict the actual values of V_e . This ratio will be defined as:

$$\eta_{SL} = \frac{P_{t2}}{P_{t1}} \quad (10)$$

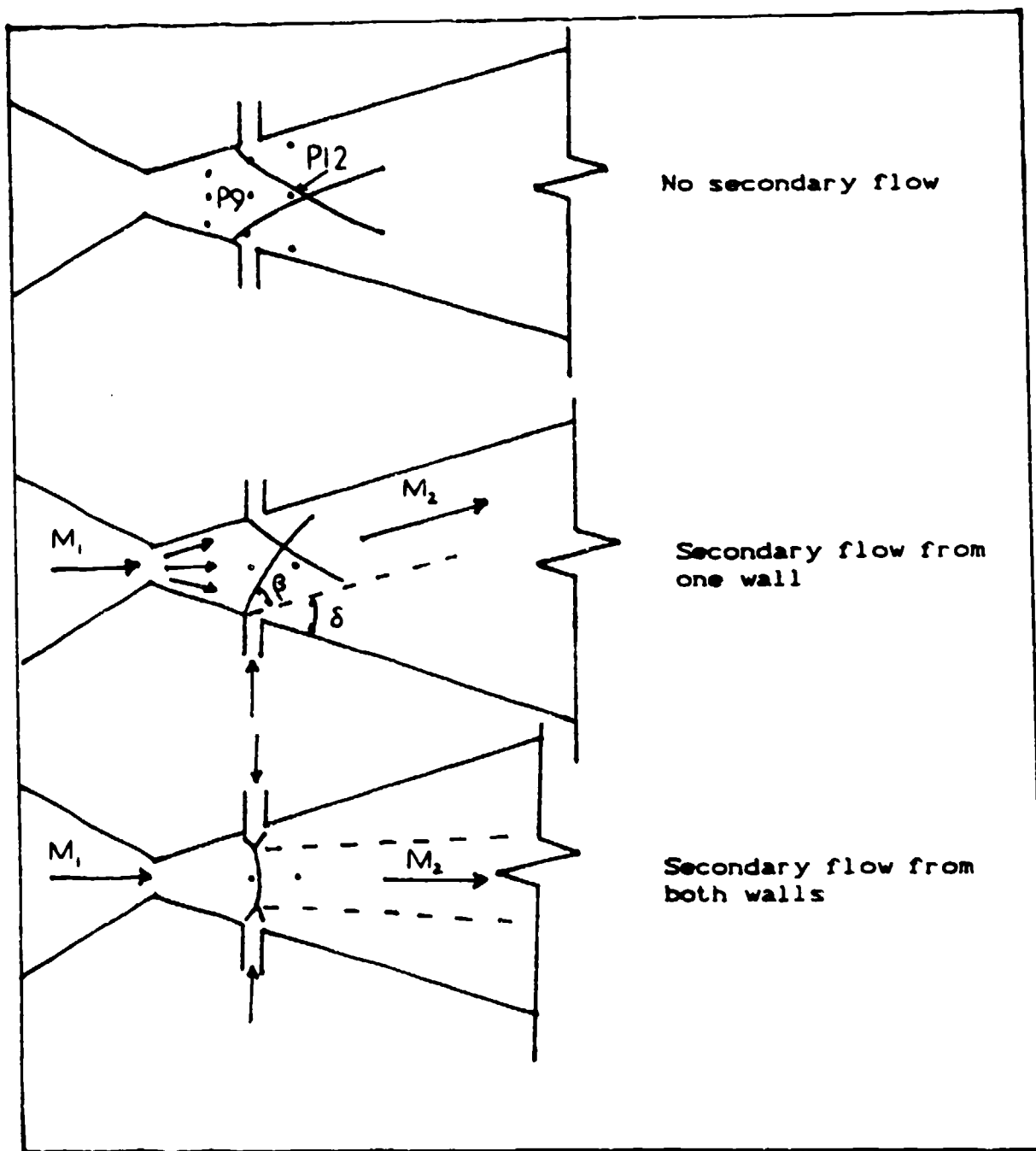
where η_{SL} is the total pressure ratio for shock loss, P_{t1} is the nozzle flow total pressure before shock loss, and P_{t2} is the nozzle flow total pressure after shock loss. Using this ratio and the isentropic exit velocity equation, the equation for the calculated exit velocity including shock loss effects becomes:

$$v_e = \left\{ \frac{2\gamma RT_t}{(\gamma-1)} \left[1 - \left(\eta_{SL} \frac{P_t}{P_e} \right)^{-\frac{(\gamma-1)}{\gamma}} \right] \right\}^{0.5} \quad (11)$$

where γ is the specific heat ratio, R is the universal gas constant, T_t is nozzle flow total temperature, P_e is exit static pressure and P_t is nozzle supply total pressure. From the results and observations of sections III and IV of this report, it is reasonable to assume that η_{SL} will be related to the pressure losses resulting from oblique shocks. In order to determine the total pressure loss across an oblique shock, the Mach number upstream of the shock and the shock angle must be known. The isentropic Mach number at the secondary flow port can be determined by the ratio of nozzle area at the port to the nozzle throat area. Oblique shock angle can be calculated by the equation:

$$\beta = \arcsin \left\{ \frac{1}{M_1} \left[\frac{\gamma + 1}{2\gamma} \left(\frac{P_2}{P_1} \right) + \left(\frac{\gamma - 1}{2\gamma} \right) \right] \right\}^{0.5} \quad (12)$$

where β is the oblique shock angle with respect to the flow turning angle, M_1 is the Mach number before the shock, γ is the specific heat ratio, P_1 is the static pressure before the shock, and P_2 is the static pressure after the shock (6:463). Figure 59 illustrates how the value of P_1 and P_2 can be taken from the measured values at static ports P9 and P12 of the test nozzle.



P_1 = static pressure upstream of oblique shock (= P_9)

P_2 = static pressure downstream of oblique shock (= P_{12})

Fig 59. Oblique Shock Formation in Nozzle Diverging Section

Once the oblique shock angle has been determined, M_2 , the Mach number downstream of the oblique shock can be calculated as:

$$M_2 = \left\{ \sin^2 \beta \left[\frac{\tan(\delta + \beta)}{\tan \beta} \left(\frac{\gamma + 1}{2} \right) - \left(\frac{\gamma - 1}{2} \right) \right] \right\}^{-0.5} \quad (13)$$

where β is the oblique shock angle, δ is the flow turning angle, and γ is the specific heat ratio (19:360). For nozzle flow with secondary flow applied from one wall, a value of $\delta = 40^\circ$ is used to model the flow turning to become parallel to the opposite nozzle wall. For nozzle flow with secondary flows applied from both walls, a value of $\delta = 20^\circ$ is used to model the flow turning to become parallel to the nozzle axis. From the values of M_1 and M_2 , the isentropic total to static pressure ratio can be determined:

$$\frac{P_t}{P} = \left[1 + \left(\frac{\gamma - 1}{2} \right) M^2 \right]^{\frac{\gamma}{\gamma - 1}} \quad (14)$$

Using these ratios, the value of the total pressure ratio due to shock loss is simply:

$$\eta_{SL} = \frac{P_{t2}}{P_{t1}} = \left[\frac{P_{t2}}{P_2} \right] \left[\frac{P_1}{P_{t1}} \right] \left[\frac{P_2}{P_1} \right] \quad (15)$$

In summary, the above loss model requires the following inputs:

m_p = primary mass flow rate

m_s = secondary mass flow rate

P_a = ambient static pressure

P_e = nozzle exit static pressure

P_t = nozzle primary flow supply pressure

P_1 = nozzle centerline static pressure at secondary
flow port

P_2 = nozzle centerline static pressure downstream
of secondary flow port

A_e = nozzle exit area

When the total force values calculated using this loss model were compared to measured values, the model values were consistently larger. Therefore, an additional loss coefficient of 0.9 was added to equation 8 for the case of secondary flow being applied from both nozzle walls. This additional total pressure loss coefficient reflects the formation of Mach reflections instead of simple oblique shocks for these cases. Table 9 lists the average ratios of the total force calculated using the shock loss model developed above to the measured total force. From this one can see that the shock loss model provides an excellent prediction of the nozzle total force. Figures 60 through 63 graphically illustrate the correlation between the shock loss model total forces and actual measured total forces.

Table 9 Average Ratio of Total Force Calculated Using the
Shock Loss Model to Measured Total Force

Nozzle	Ratio of Loss Model to Measured Total Force		
	Secondary Flow Applied from Upper Wall	Secondary Flow Applied from Lower Wall	Secondary Flow Applied from Both Walls
1	0.952 \pm 0.058	0.952 \pm 0.057	1.01 \pm 0.008
2	0.992 \pm 0.057	0.956 \pm 0.053	1.01 \pm 0.033
3	0.901 \pm 0.010	0.893 \pm 0.013	0.978 \pm 0.018
4	0.985 \pm 0.017	0.995 \pm 0.015	0.995 \pm 0.014

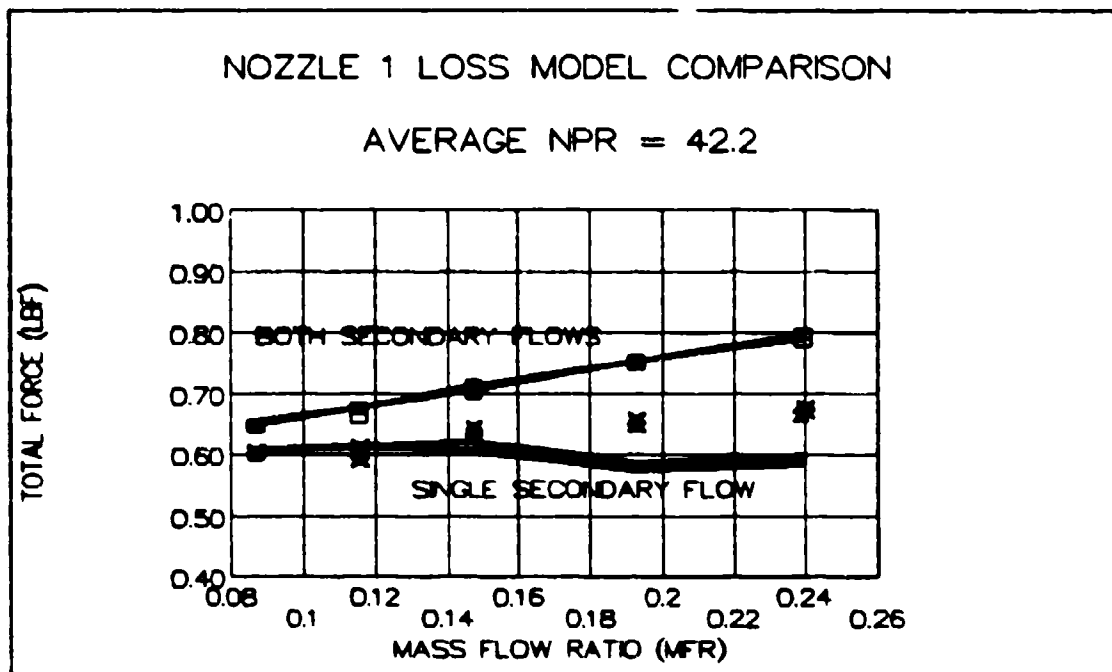


Fig 60 Comparison of Loss Model and Measured Total Force Values for Nozzle 1

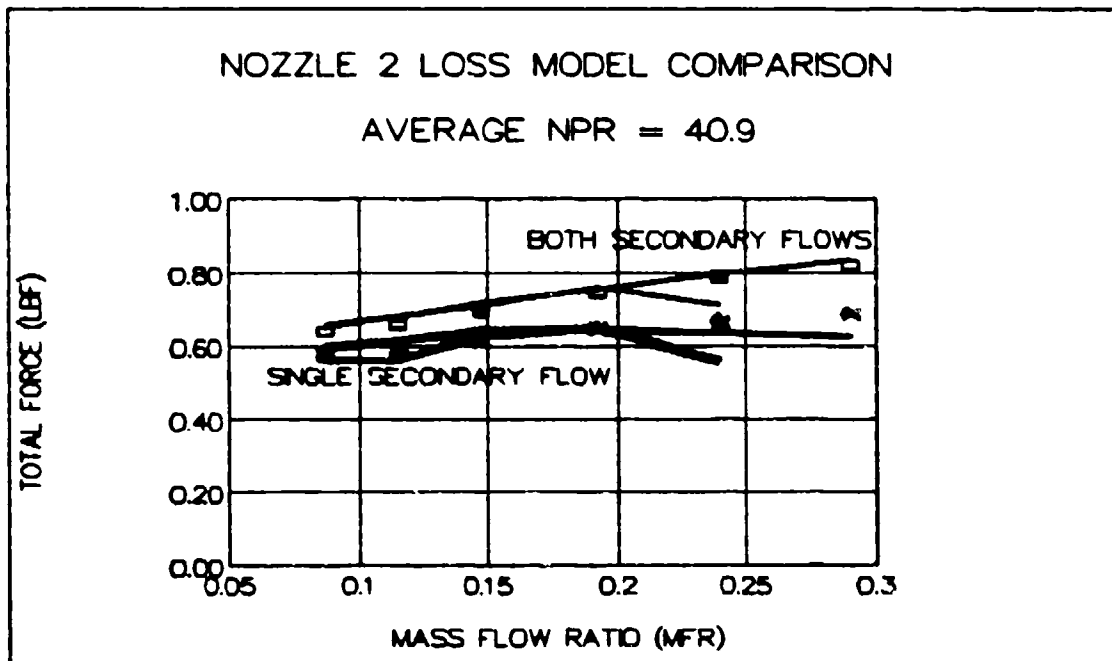


Fig 61 Comparison of Loss Model and Measured Total Force Values for Nozzle 2

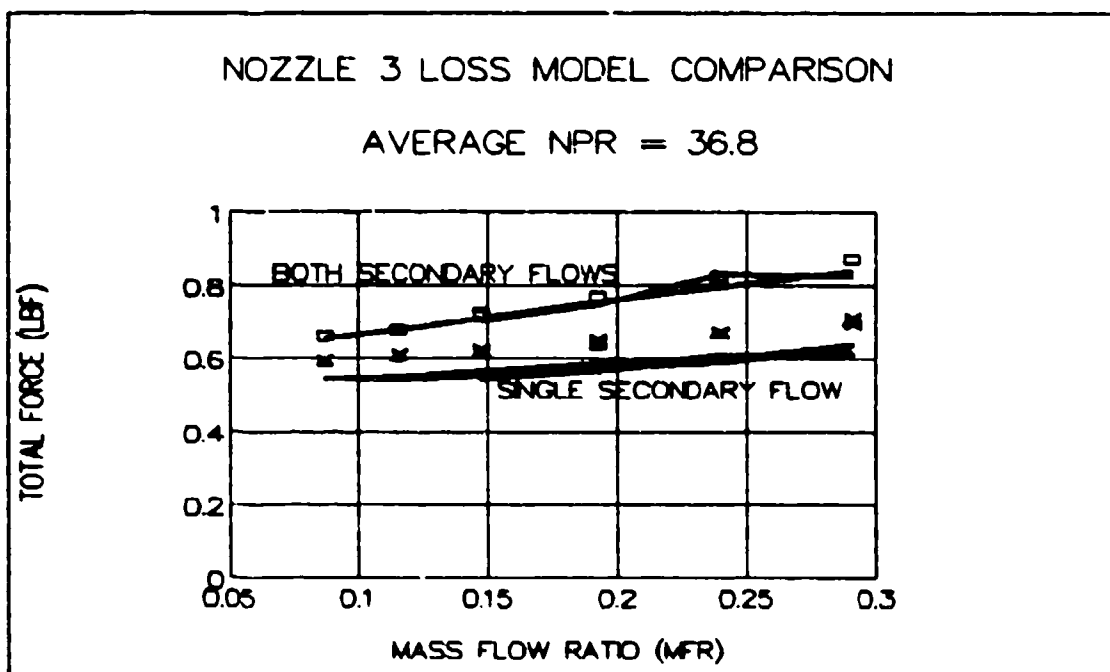


Fig 62 Comparison of Loss Model and Measured Total Force Values for Nozzle 3

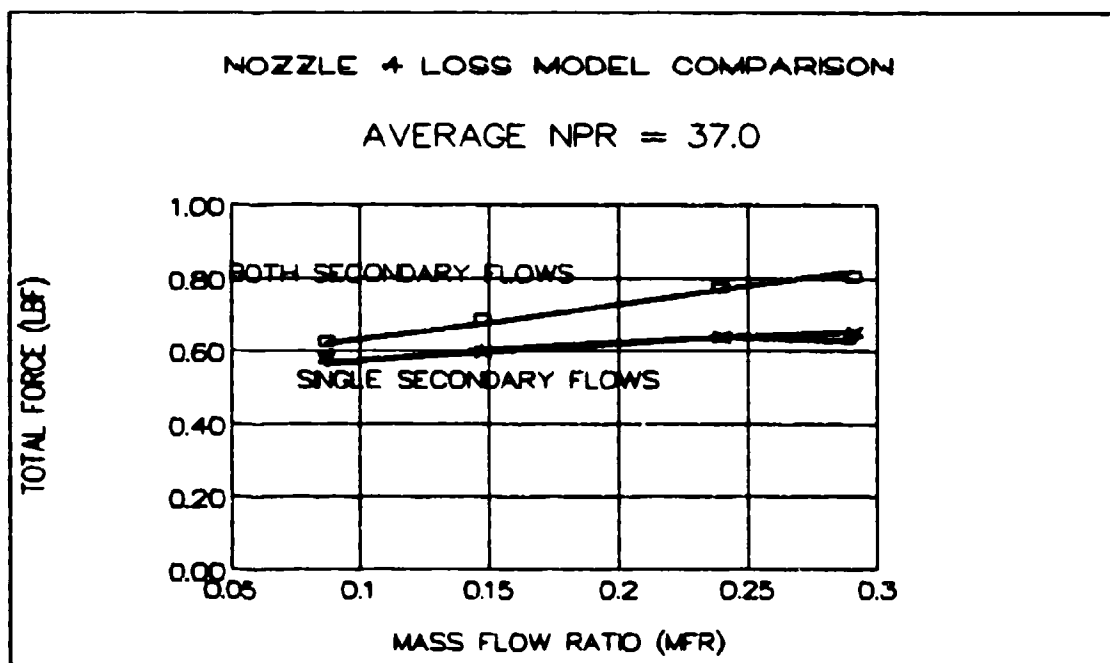


Fig 63 Comparison of Loss Model and Measured Total Force Values for Nozzle 4

VI. Conclusions

From the observations, results, and analyses presented in this report, the following conclusions can be made:

1. The presence of secondary injection ports may induce oblique shocks to form in the diverging section of the nozzles tested. These shocks cause the flow to separate from the nozzle wall. The interactions of these shocks influence the flow path within the nozzle.

2. The CJTVC nozzles tested showed increased axial flow stability with increasing NPR for primary flows with no secondary flow.

3. A critical secondary flow to primary flow mass flow ratio (MFR) exists below which a nozzle will not vector. A second critical MFR exists that produces maximum vector performance within a given nozzle.

4. Flow visualization and side force measurements show that all nozzles had a slight bias towards flow attachment to the lower nozzle wall, therefore producing a positive vector angle bias.

5. From a comparison of the flow performance parameters measured at a primary flow supply pressure of 2.923 bar absolute, nozzle 1 has the best vectoring performance of all the nozzles tested.

6. Flow vectoring response times for nozzle 1 at its best vector range MFR vary from 43.0 to 140.2 ms (7.1 to 23.3 Hz) when measured from the point of time when the

secondary flow solenoid valve opens or closes. The same response times vary between 3.0 and 98.2 ms (10.2 to 333.3 Hz) when measured from the point in time when the secondary flow reaches its supply line pressure.

7. The Green/McCullough model for side force to axial force ratio provides a good approximation of the actual ratio when the proper multiplicative coefficient or additive constant is used.

8. The shock loss model developed in this report provides an excellent prediction of the actual total force produced by the nozzles tested.

VII. Recommendations

For anyone desiring to continue research in the areas described in this report, the following recommendations are provided:

1. Replace the existing plexiglass walls of the nozzle test assembly for schlieren photographs with optical-quality glass. This would allow for better photographs of shock and boundary layer structures within the nozzle.

2. Study nozzle starting process at lower NPRs to determine causes of flow bias, especially the formation of vortices. High speed cameras and oil film or china clay flow visualization could be used in this study.

3. Develop permanently sealed nozzle assemblies rather than interchangeable nozzle walls and plates. This will help avoid any flow bias due to nozzle leakage or assembly misalignment.

4. Study the effects of using suction in the secondary flow port for enhanced flow attachment to the wall opposite the secondary port which is injecting flow.

5. Study the effects of varying the angle of the secondary flow axis to where it points upstream into the primary flow.

6. Modify the existing test assemblies to move the secondary flow solenoid valves as close as possible to the secondary injection ports.

Appendix A: Test Model and Test Facilities

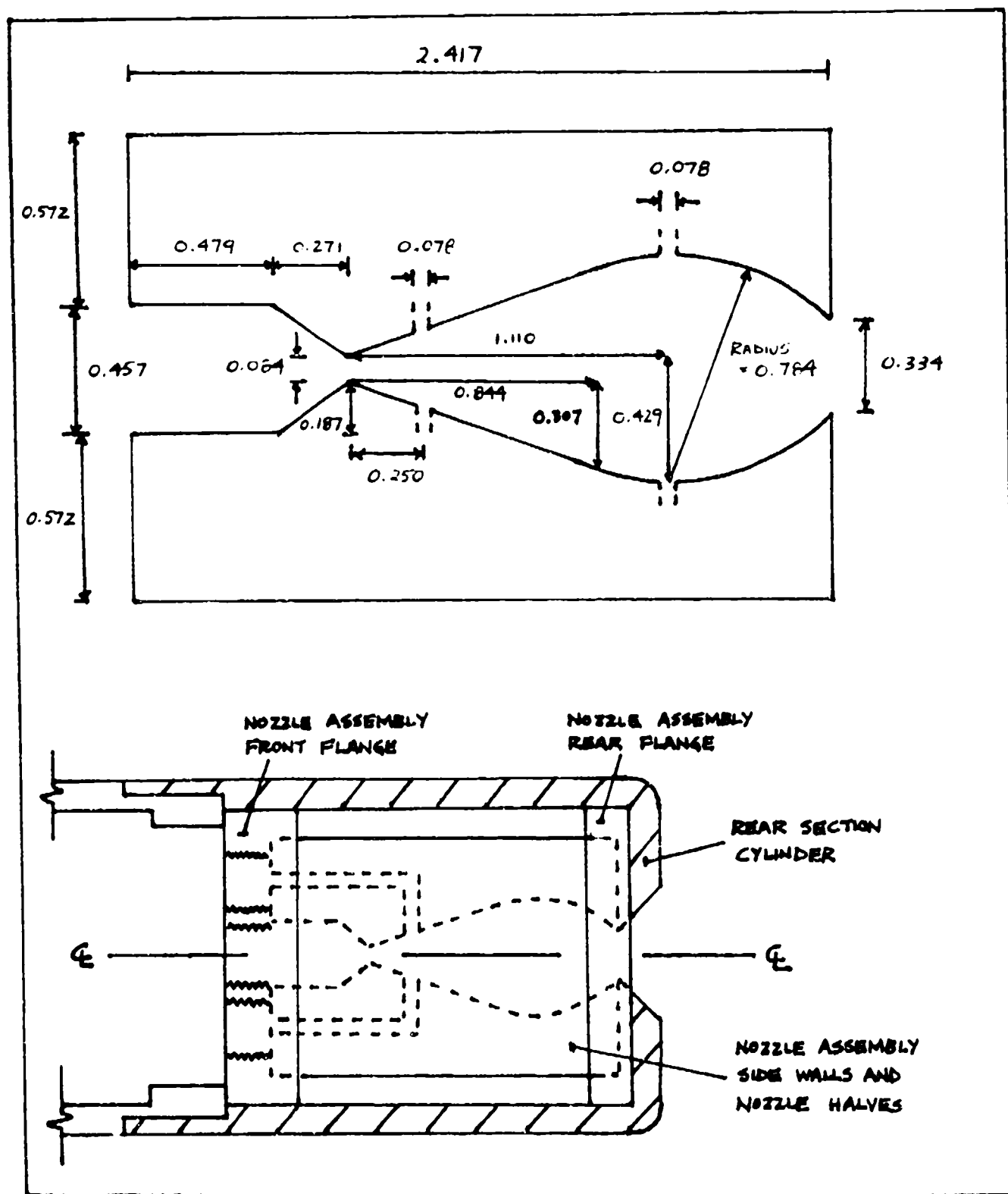


Fig 64 Nozzle Design Details and Dimensions

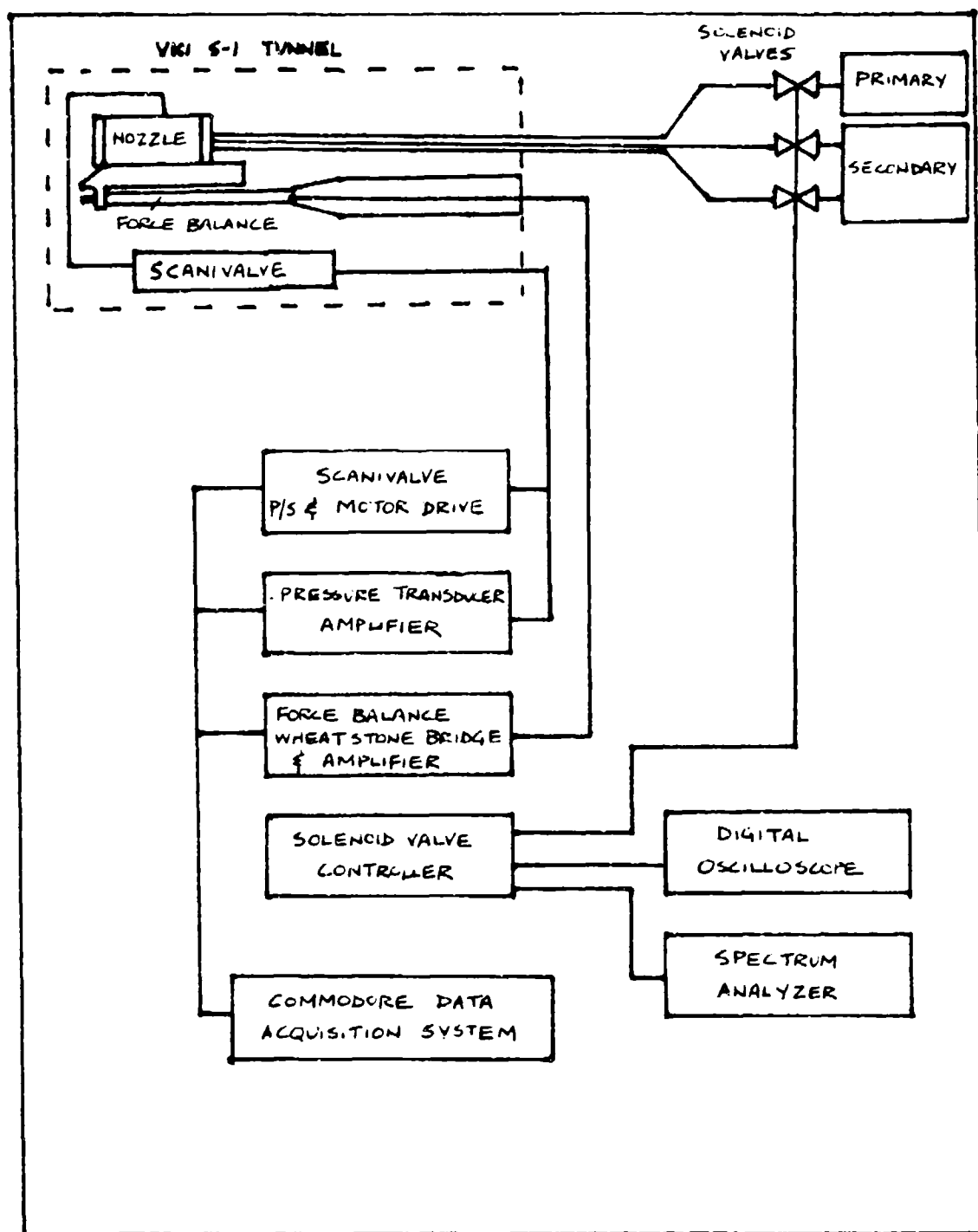


Fig 65 VKI Wind Tunnel Apparatus

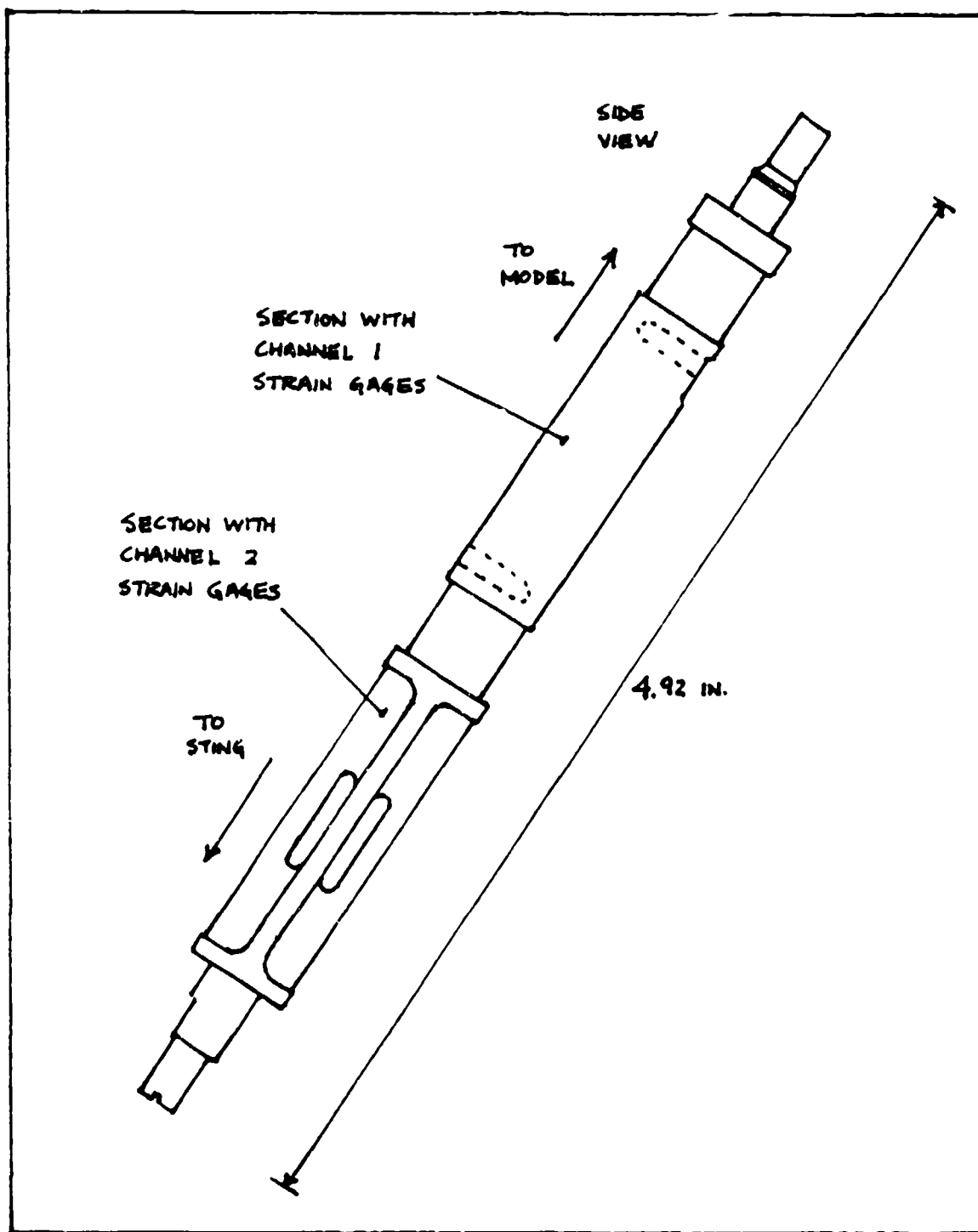


Fig 66 VKI Six Component Force Balance

Appendix B: Sample Calculations

- Thompson Separation Model
- Ideal Thrust and Thrust Efficiency
- Side Momentum Gain (G_M)
- Flow Momentum Ratio (R_M)
- Reynolds Number
- Boundary Layer Thickness
- Broadwell Force Ratio Model
- Green/McCullough Force Ratio Model
- Shock Loss Total Force Model

Thompson Separation Model

Thompson developed the following equation for predicting the Mach number at flow separation (M_s) in a convergent-divergent nozzle subjected to an adverse pressure gradient (20:4):

$$M_s = \left[6.17 \left(\frac{P_t}{P_a} \right)^{0.286} - 5 \right]^{0.5} \quad (16)$$

Using isentropic relations, the area ratio at which this Mach occurs can be determined (7:84):

$$\frac{A}{A_t} = \frac{1}{M} \left\{ \frac{2}{\gamma + 1} \left[1 + \left(\frac{\gamma - 1}{2} \right) M^2 \right] \right\}^{\frac{(\gamma + 1)}{2(\gamma - 1)}} \quad (17)$$

where A is the nozzle area at which M occurs and A_t is the nozzle throat area. For constant channel height nozzle geometry, the following equation for the length along the nozzle axis at which separation occurs (x_s) is:

$$x_s = \frac{1}{2 \tan \alpha} \left[w_t \left(\frac{A}{A_t} \right) - w_t \right] \quad (18)$$

SAMPLE CALCULATION:

Input Values:

$$\frac{P_t}{P_a} = 20$$

$$w_t = 0.050 \text{ (normalized value)}$$

Output Values:

$$M_s = 3.09$$

$$\frac{A}{A_t} = 4.61$$

$$x_s = 0.248 \text{ (normalized value)}$$

Ideal Thrust and Thrust Efficiency

For ideal thrust calculations, the flow is assumed to isentropically expand to where the exit static pressure equals the ambient static pressure (18:26). This reduces equation 7 of this report to:

$$F_{t,ideal} = (m_s + m_p) V_e \quad (19)$$

where V_e is calculated using equation 11 of this report with $\eta_{SL} = 1$ (no shock loss) and $P_e = P_a$. Thrust efficiency is simply the ratio of the measured total thrust to the ideal total thrust:

$$\text{THRUST EFFICIENCY} = \frac{F_t}{F_{t,ideal}} \quad (20)$$

SAMPLE CALCULATION:

Input Values:

- $F_t = 0.603 \text{ lbf}$
- $m_s = 0.000971 \text{ lbm/s}$
- $m_p = 0.011162 \text{ lbm/s}$
- $T_t = 530 \text{ }^\circ\text{R}$
- $P_t = 42.4 \text{ psia}$
- $P_e = P_a = 1.13 \text{ psia}$
- $\gamma = 1.4$
- $R = 1716 \text{ ft}^2/\text{s}^2 \text{ }^\circ\text{R}$

Output Values:

- $V_e = 2026 \text{ ft/s}$
- $F_{t,ideal} = 0.764 \text{ lbf}$

THRUST EFFICIENCY = 0.789

Side Momentum Gain

The side momentum gain (G_M) is defined as the ratio of measured side force (F_s) to the momentum of the secondary jet flow, and is given by:

$$G_M = \frac{F_s}{m_s V_s} \quad (21)$$

where m_s is the secondary mass flow rate and V_s is the secondary flow velocity. V_s is calculated using equation 11 of this report with $\eta_{SL} = 1$ (no shock loss), with P_t equal to the secondary supply pressure, and with P_e equal to the static pressure measured at the exit of the secondary flow port.

SAMPLE CALCULATION:

Input Values: $F_s = 0.196$ lbf
 $m_s = 0.000971$ lbm/s
 $T = 530$ °R
 $P_t = 17.2$ psia
 $P_e = 4.22$ psia
 $\gamma = 1.4$
 $R = 1716$ ft²/s² °R

Output Values: $V_s = 1451$ ft/s
 $G_M = 4.47$

Flow Momentum Ratio

The flow momentum ratio (R_M) is defined as the ratio of secondary flow momentum to primary flow momentum at the secondary flow port, and is given by:

$$R_M = \frac{m_s V_s}{m_p V_p} \quad (22)$$

where m_s and V_s are the same quantities as in equation 21. m_p is primary mass flow rate, and V_p is the flow velocity at the secondary port. V_∞ is given by the isentropic equations:

$$V_p = M_1 \left(\gamma R T \right)^{0.5} \quad (23)$$

$$T = T_t \left[1 + \left(\frac{\gamma - 1}{2} \right) M_1^2 \right]^{-1} \quad (24)$$

where M_1 , T , T_t are the Mach number, static temperature, and total temperature at the secondary port (7:55). M_∞ is calculated using equation 17 of this report.

SAMPLE CALCULATION:

Input Values:

$$\frac{A}{A_t} = 2.84$$

$$m_s = 0.000971 \text{ lbm/s}$$

$$m_p = 0.011162 \text{ lbm/s}$$

$$T_t = 530 \text{ }^\circ\text{R}$$

$$P_{t, \text{secondary}} = 17.2 \text{ psia}$$

$$P_{e, \text{secondary}} = 4.22 \text{ psia}$$

$$\gamma = 1.4$$

$$R = 1716 \text{ ft}^2/\text{s}^2 \text{ } ^\circ\text{R}$$

Output Values:

$$V_s = 1451 \text{ ft/s}$$

$$M_1 = 2.58$$

$$V_2 = 1907 \text{ ft/s}$$

$$R_M = 0.662$$

Reynolds Number

The length-based and hydraulic diameter-based Reynolds numbers are defined as:

$$Re_L = \frac{u_{\infty} L}{\nu} \quad (25)$$

$$Re_{D_h} = \frac{u_{\infty} D_h}{\nu} \quad (26)$$

where L is the length along a nozzle wall, u_{∞} is flow velocity, ν is flow kinematic viscosity, and D_h is hydraulic diameter defined by

$$D_h = \frac{4A}{P} \quad (27)$$

where A is the area of the flow channel and P is the perimeter of the flow channel. If the value of Re_L and Re_{D_h} are greater than 3.5×10^5 , the flow is considered to be turbulent (16:41).

SAMPLE CALCULATION:

Input Values: $L = 0.239 \text{ in} = 0.01992 \text{ ft}$
 $A = 0.0619 \text{ in}^2 = 4.30 \times 10^{-4} \text{ ft}^2$
 $P = 0.996 \text{ in} = 0.0830 \text{ ft}$
 $u_{\infty} = 1907 \text{ ft/s}$
 $\nu = 3.48 \times 10^{-5} \text{ ft}^2/\text{s}$
Output Values: $D_h = 0.249 \text{ in} = 0.021 \text{ ft}$

$$\begin{aligned} \text{Re}_L &= 1.09 \times 10^6 && \text{TURBULENT FLOW} \\ \text{Re}_{D_h} &= 1.15 \times 10^6 && \text{TURBULENT FLOW} \end{aligned}$$

Boundary Layer Thickness

Equation 1 of this report is used to calculate the boundary layer thickness at the secondary port location. Equations 2 and 3 are then used to determine displacement thickness and momentum thickness.

SAMPLE CALCULATION:

Input Values: $x = 0.225 \text{ in} = 0.01992 \text{ ft}$

$$u_\infty = 1907 \text{ ft/s}$$

$$\nu = 3.48 \times 10^{-5} \text{ ft}^2/\text{s}$$

Output Values: $\delta_t = 0.00548 \text{ in}$

$$\delta_1 = 0.00069 \text{ in}$$

$$\delta_2 = 0.00053 \text{ in}$$

Broadwell Force Ratio Model

Equation 4 of this report is used to calculate the Broadwell model values for side force to axial force ratio. V_e is calculated using equation 11 of this report with $\eta_{SL} = 1$ (no shock loss) and $P_e = P_a$. V_s is calculated using the same method as described for G_M calculations (equation 21 of this report).

SAMPLE CALCULATION:

Input Values: $\gamma = 1.4$
 $\alpha = 0.17$
 $M_\infty = 2.58$
 $V_\infty = 1907 \text{ ft/s}$
 $P_{t,\text{secondary}} = 17.2 \text{ psia}$
 $P_{e,\text{secondary}} = 4.22 \text{ psia}$
 $P_{t,\text{primary}} = 42.4 \text{ psia}$
 $P_{e,\text{primary}} = P_a = 1.13 \text{ psia}$
 $R = 1716 \text{ ft}^2/\text{s}^2 \text{ } ^\circ\text{R}$
 $T_{t1} = T_{t\infty} = 530 \text{ } ^\circ\text{R}$
 $\dot{m}_1 = 0.000971 \text{ lbm/s}$
 $\dot{m}_p = 0.011162 \text{ lbm/s}$
 $\alpha = 90^\circ$
 $\beta = 70^\circ$

Output Values: $V_{ex} = 2026 \text{ ft/s}$
 $V_1 = 1451 \text{ ft/s}$
 $\frac{F_s}{F_A} = 0.241$

Green/McCullough Model

Equation 5 of this report is used to calculate the Green/McCullough model values for side force to axial force ratio. I_{sp} is calculated using equation 6 of this report. Two values of the equation are given; one value for when the coefficient C_1 is multiplied to equation 5 and one value for when the constant C_2 is added to equation 5 (with $C_1 = 1$).

SAMPLE CALCULATION:

Input Values

$$C_1 = 4.29$$

$$C_2 = 0.200$$

$$w_i = 0.000971 \text{ lbf/s}$$

$$w_p = 0.011182 \text{ lbf/s}$$

$$F_t = 0.803 \text{ lbf}$$

$$P_{t, \text{secondary}} = 1.187 \text{ bar abs}$$

$$P_{e, \text{secondary}} = 0.291 \text{ bar abs}$$

Output Values:

$$I_{sp} = 49.7 \text{ s}$$

$$\left(\frac{F_S}{F_A} \right)_{C_1} = 0.175$$

$$\left(\frac{F_S}{F_A} \right)_{C_2} = 0.241$$

Shock Loss Total Force Model

Equations 7 through 15 of this report are used to calculate the total force value using the shock loss modeling developed by the author. The order of calculation is as follows:

1. Use equation 12 to calculate β
2. Use equation 13 to calculate M_2
3. Use equation 14 to calculate P_t / P
4. Use equation 15 to calculate η_{SL}
5. Use equation 11 to calculate V_e
6. Use equation 9 to calculate λ
7. Use equations 7 and 8 to calculate F_t

SAMPLE CALCULATION:

Input Values:

$M_1 = 2.58$
 $P_2 = 5.89 \text{ psia}$
 $P_1 = 2.21 \text{ psia}$
 $\gamma = 1.4$
 $\delta = 40^\circ$
 $\alpha = 20^\circ$
 $m_s = 0.000971 \text{ lbm/s}$
 $m_p = 0.011162 \text{ lbm/s}$
 $P_e = 3.39 \text{ psia}$
 $P_a = 1.13 \text{ psia}$
 $A_e = 0.08397 \text{ in}^2$

Output Values:

$\beta = 37.9^\circ$
 $M_2 = 0.617$

$$\eta_{SL} = 0.184$$

$$V_e = 1162 \text{ ft/s}$$

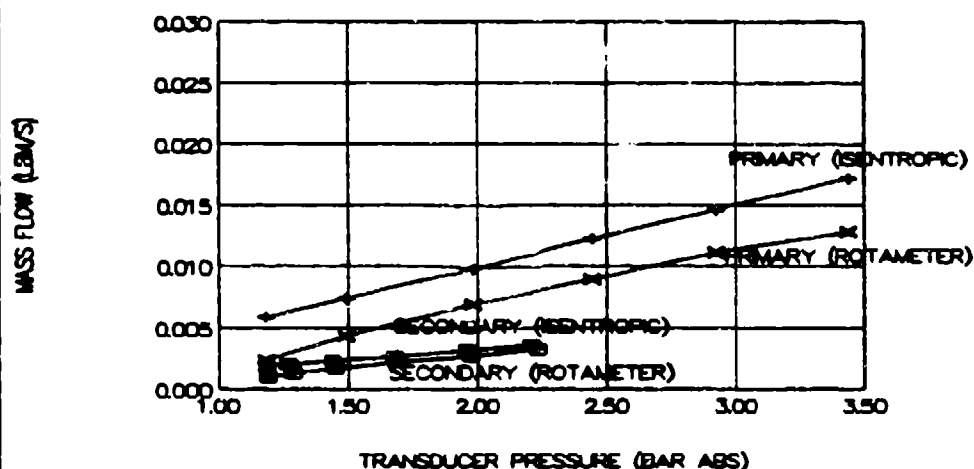
$$\lambda = 0.97$$

$$F_t = 0.609 \text{ lbf}$$

Appendix C: Mass Flow Measurements

The nozzle mass flow rates were measured using a model G1.1000 ROTAMETER which consists of a wedge-shaped float in a tapered glass tube with an inlet fitting on the bottom and an exit fitting on the top. The principle of operation of the device is that the equilibrium between the float's weight, buoyancy, and drag will place it at a certain height in the tube for a given mass flow rate and pressure. The values of float height and fluid pressure are recorded and the mass flow rate is calculated using formulas contained in ROTAMETER company literature. A metal float with a mass of 59.3 g, density of 7.94 g/cm^3 , and maximum diameter of 21.6 mm was used to measure primary flow. A plastic float with a mass of 16.28 g, density of 2.140 g/cm^3 , and maximum diameter of 21.6 mm was used to measure secondary flow. Three measurements were recorded and averaged for each flow condition. Fig 63 summarizes the mass flow rate measurement results and compares it to isentropic mass flow rates calculated assuming choked flow at the nozzle throat.

MASS FLOW VALUES ROTAMETER VS ISENTROPIC VALUES



MASS FLOW CALCULATIONS	DIAL PRESS (BAR ABS)	TRANS PRESS (BAR ABS)	DIAL ERROR (%)	ROTA MASS FLOW (LBM/S)	ISEN MASS FLOW (LBM/S)	ISEN ERROR (%)	ROTA HT (CM)
PRIMARY LINE	1.20	1.182	-1.50	0.002366	0.005916	150.01	1.92
	1.50	1.489	-0.73	0.004346	0.007452	71.49	3.32
	2.00	1.982	-0.90	0.006964	0.00992	42.46	4.32
	2.50	2.446	-2.16	0.008973	0.012242	36.43	4.97
	3.00	2.923	-2.57	0.011162	0.01463	31.07	5.55
	3.50	3.439	-1.74	0.01284	0.017212	34.05	6.07
+1 SECONDARY	1.20	1.187	-1.08	0.000971	0.001903	96.03	1.60
	1.36	1.284	-5.59	0.001292	0.002059	59.40	2.05
	1.51	1.447	-4.17	0.001645	0.00232	41.02	2.55
	1.81	1.685	-6.91	0.002152	0.002702	25.55	3.12
	2.11	1.976	-6.35	0.00268	0.003169	18.24	3.55
	2.41	2.236	-7.22	0.003253	0.003585	10.21	3.80
-1 SECONDARY	1.20	1.183	-1.42	0.000969	0.001897	95.70	1.60
	1.36	1.262	-7.21	0.001281	0.002024	58.03	2.05
	1.51	1.436	-4.90	0.001639	0.002303	40.48	2.55
	1.81	1.675	-7.46	0.002146	0.002686	25.18	3.10
	2.11	1.955	-7.35	0.002666	0.003135	17.61	3.52
	2.41	2.209	-8.34	0.003234	0.003542	9.54	3.80

Fig 87 Nozzle Mass Flow Measurements

Appendix D: Static Pressure Profiles

The figures on the following pages are the individual static pressure profiles used to generate the summary plots of centerline pressures found in this report. Pressure values shown in the nozzle outlines are given in bar absolute. The following is an index for determining which individual figures match which summary figures:

Summary Figure	Nozzle	Individual Figure
Fig 23	0	68
	1	69
	3	70
	4	71
	5	72
Fig 44	1	73
	2	76
	3	79
	4	82
Fig 45	1	74
	2	77
	3	80
	4	83
Fig 46	1	75
	2	78
	3	81
	4	84

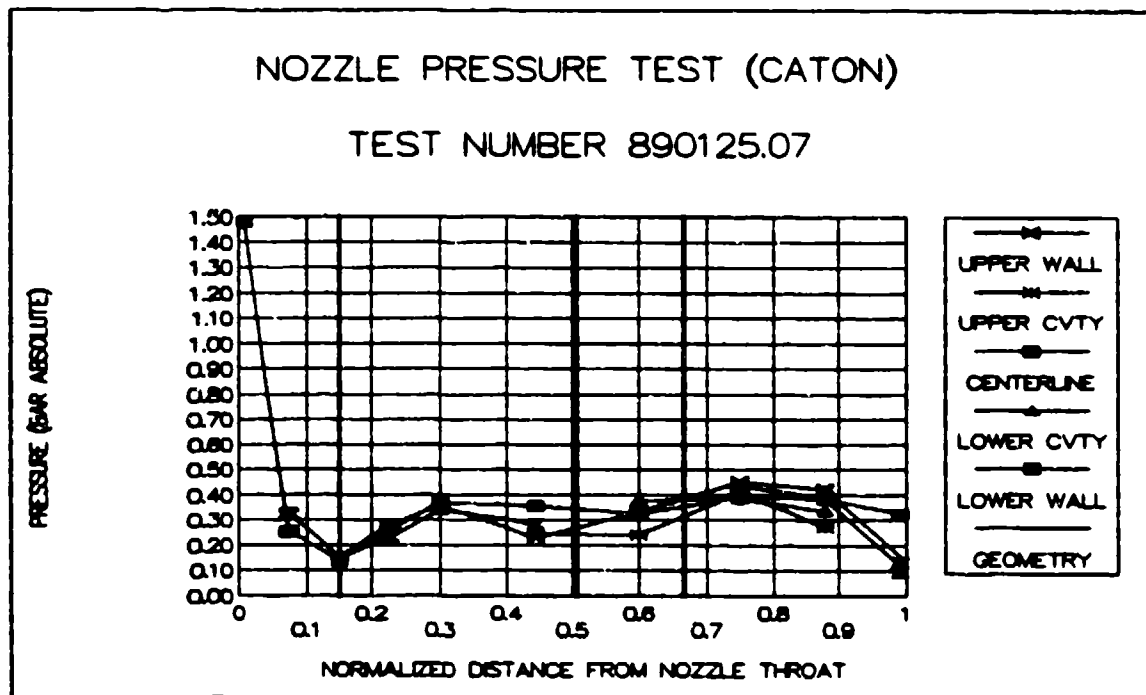
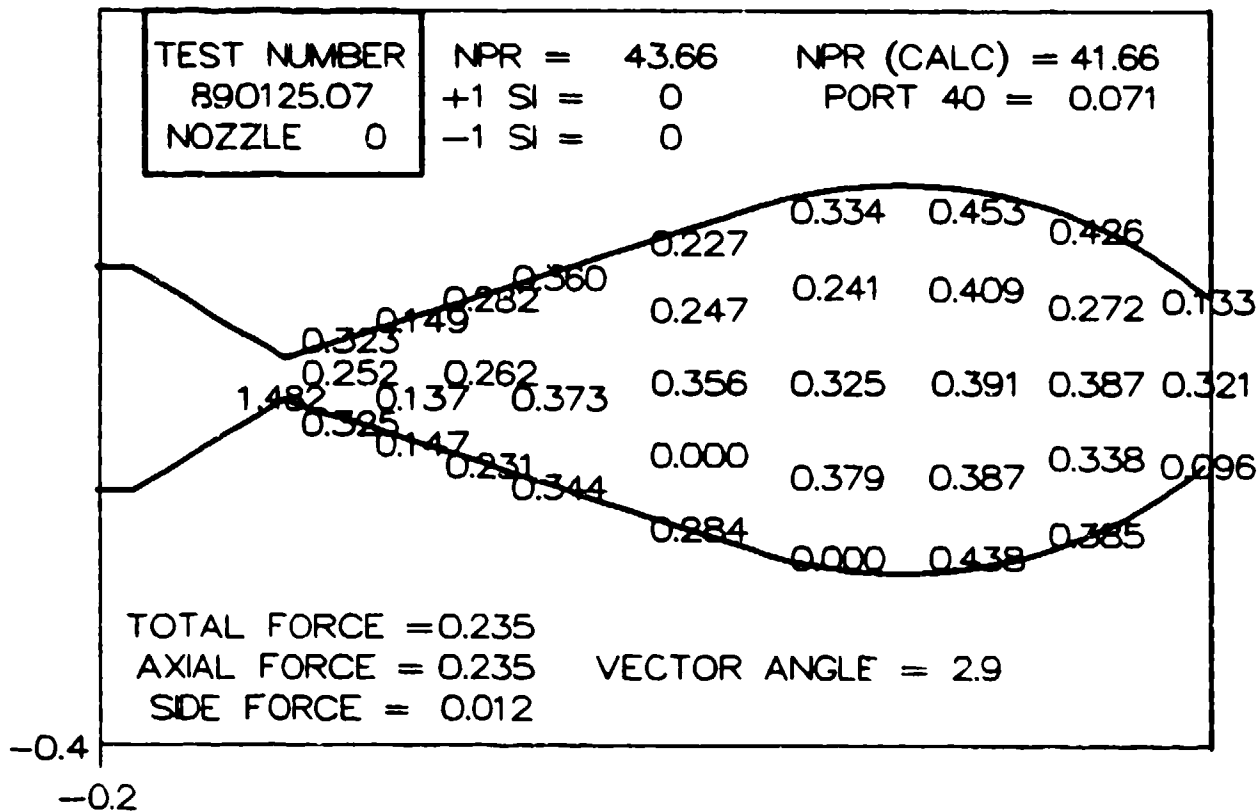


Fig 68 Static Pressure Profiles for Test Number 890125.07

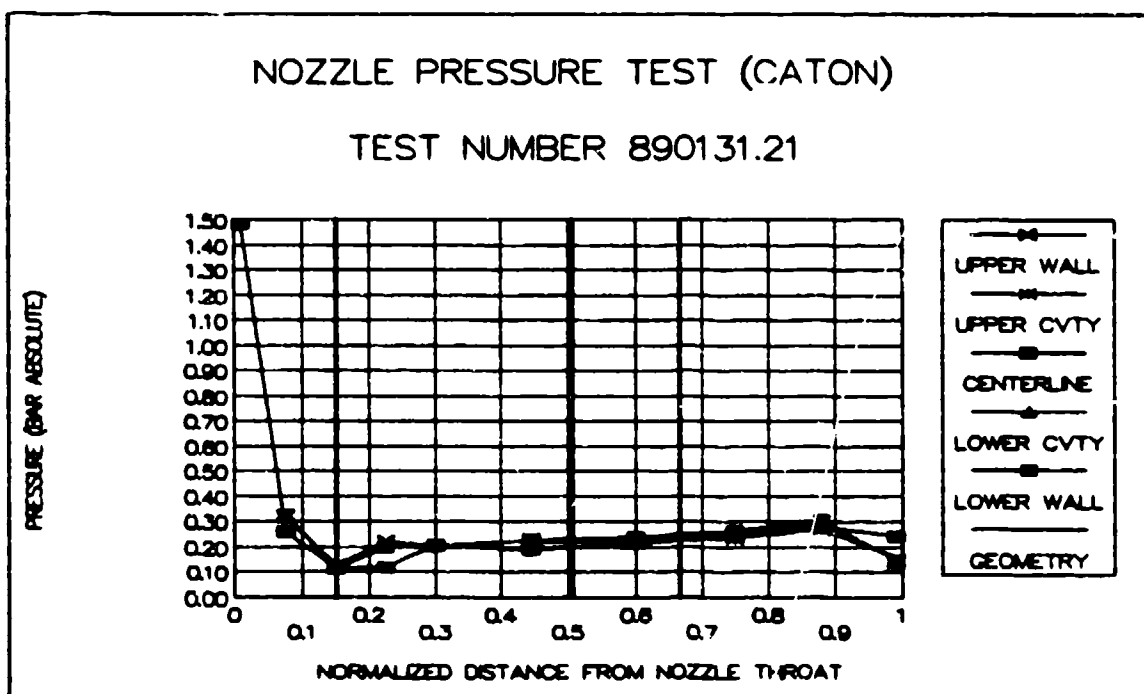
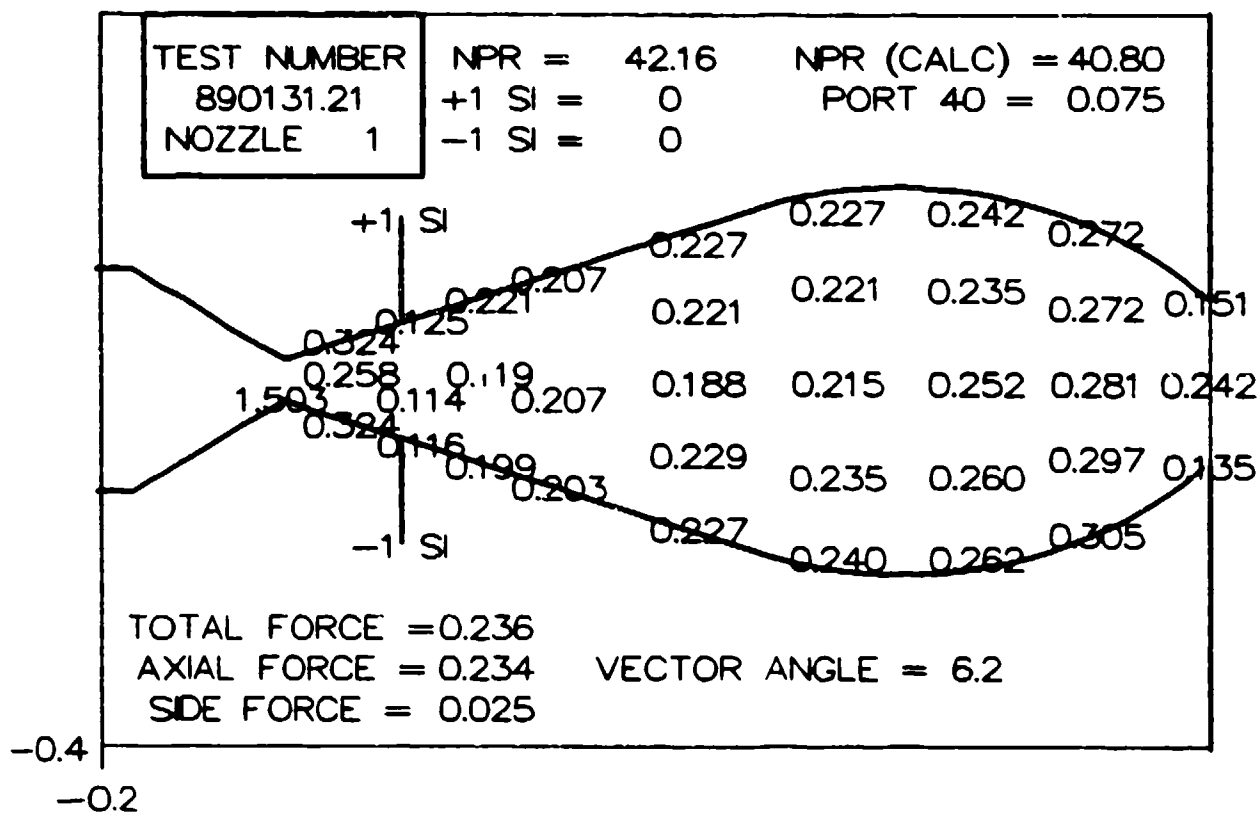


Fig 69 Static Pressure Profiles for Test Number 890131.21

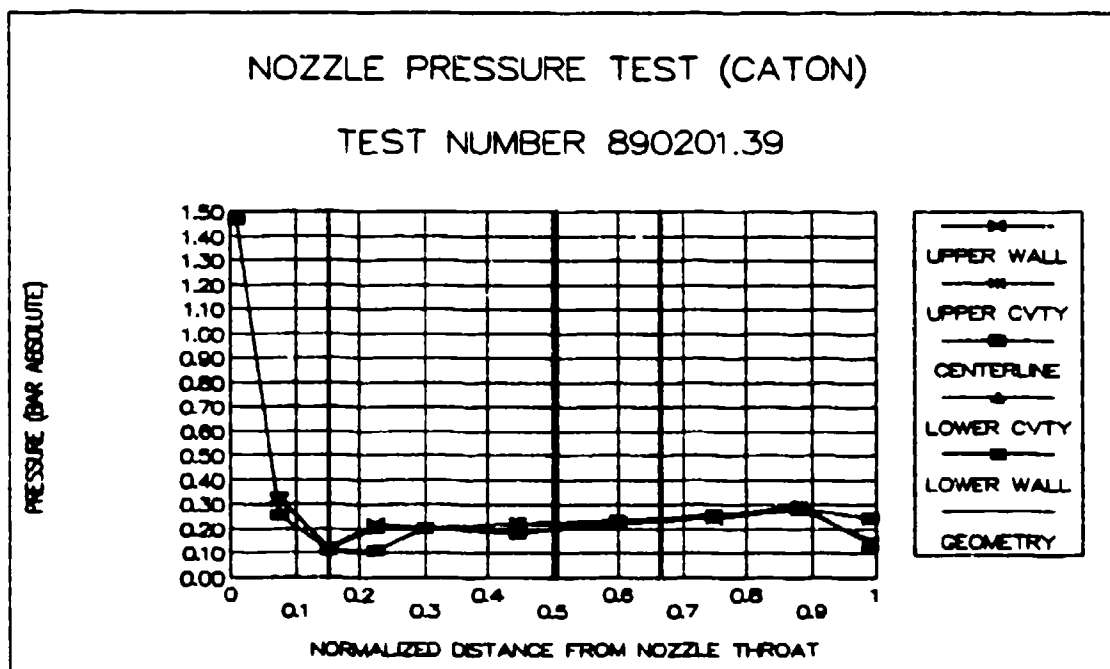
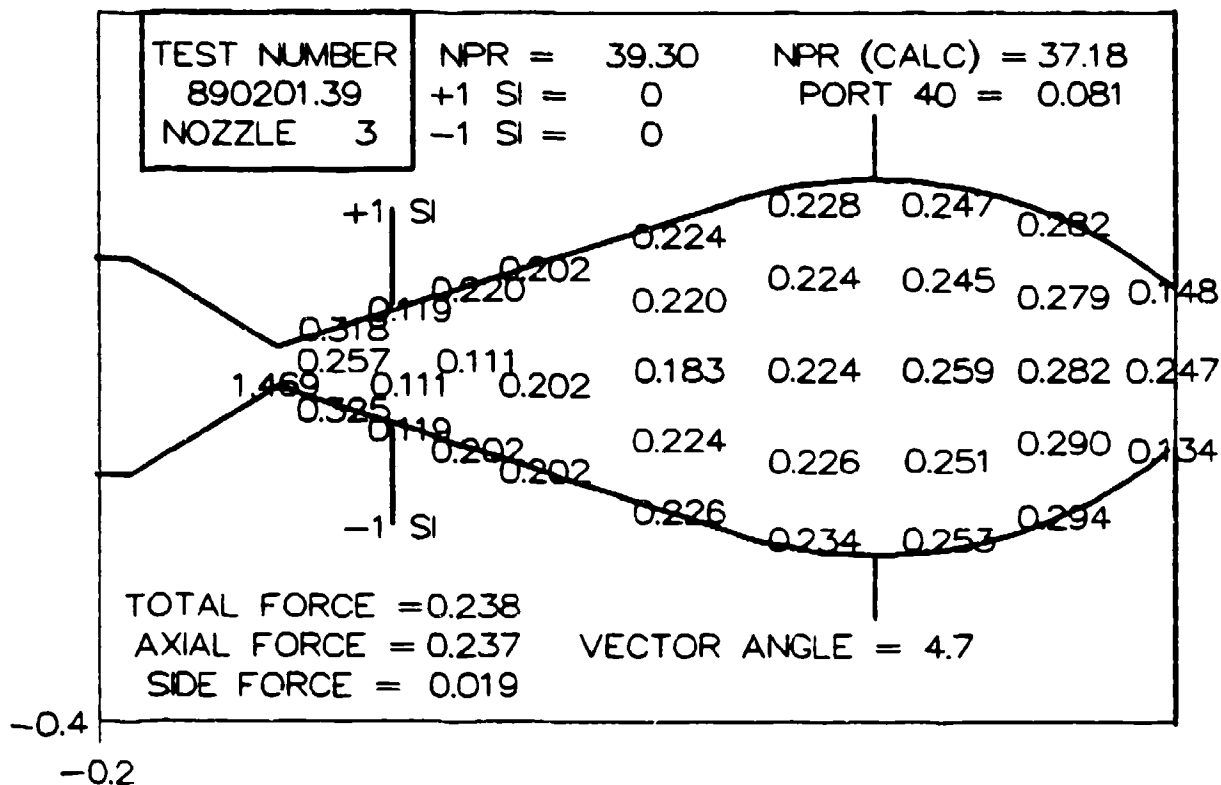


Fig 70 Static Pressure Profiles for Test Number 890201.39

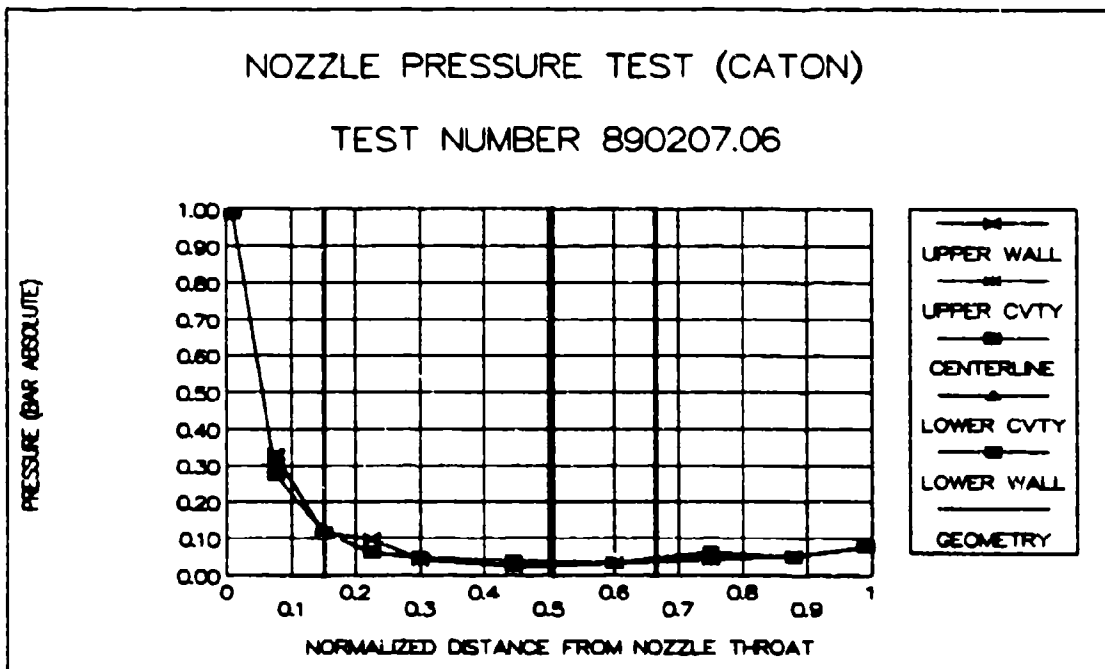
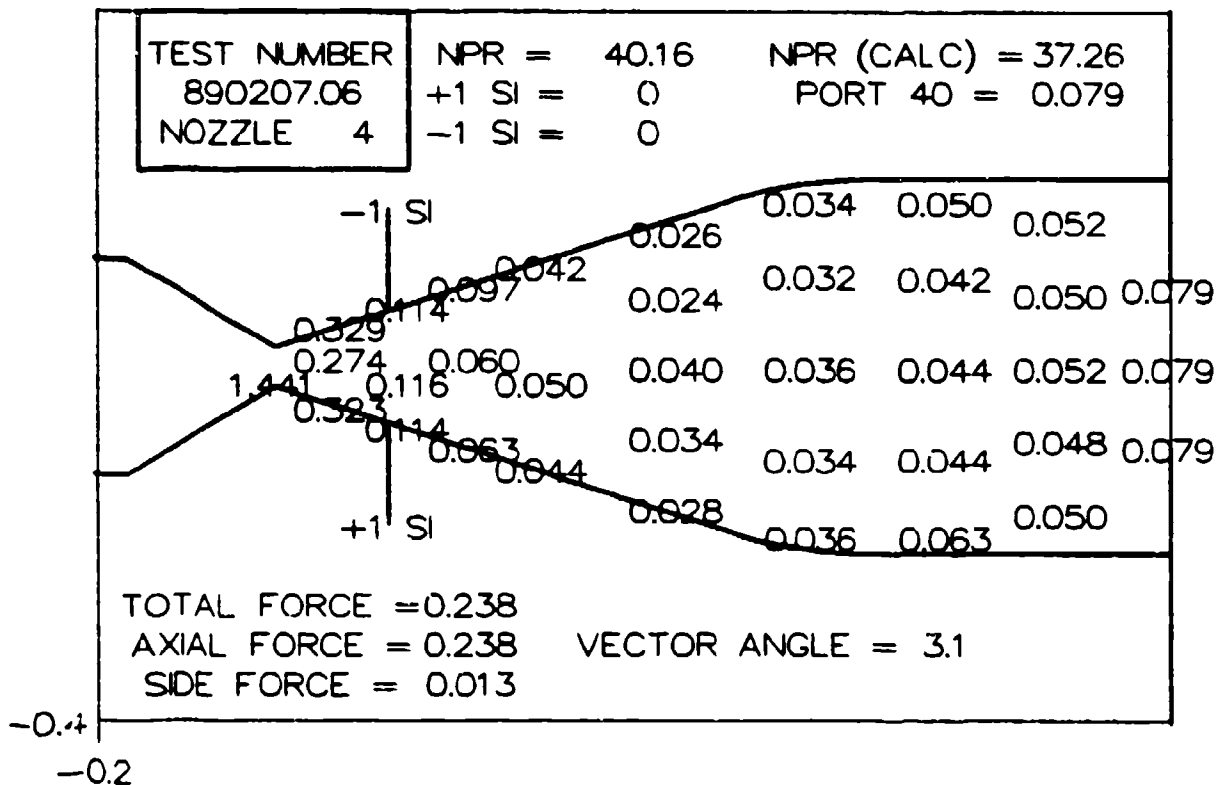


Fig 71 Static Pressure Profiles for Test Number 890207.06

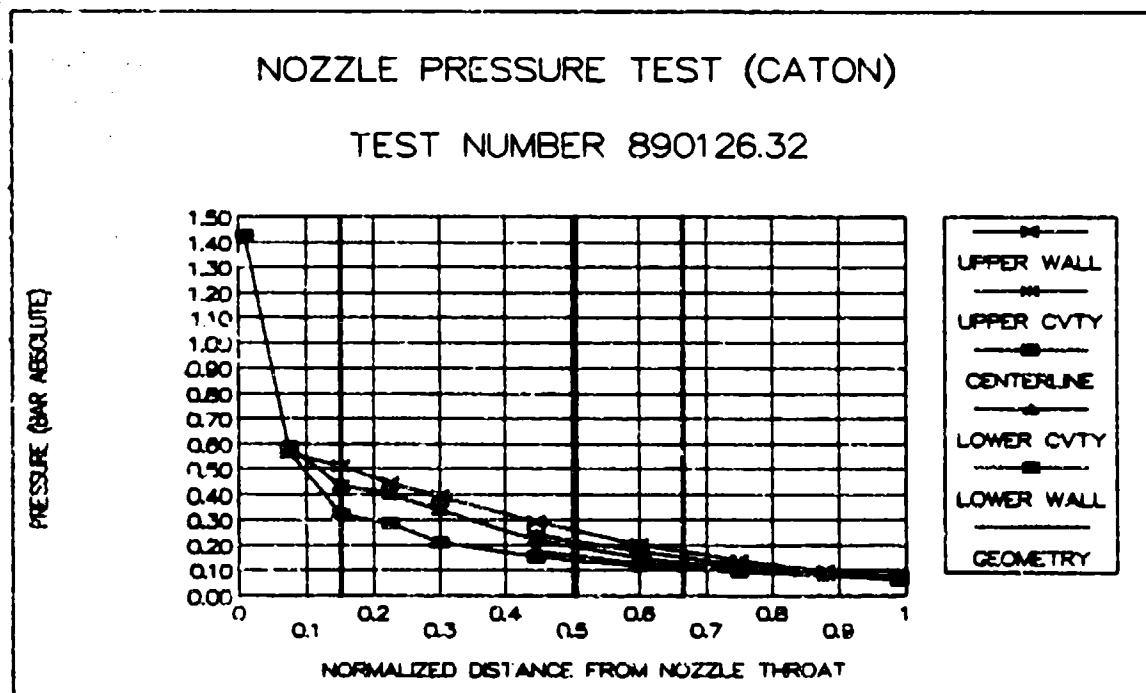
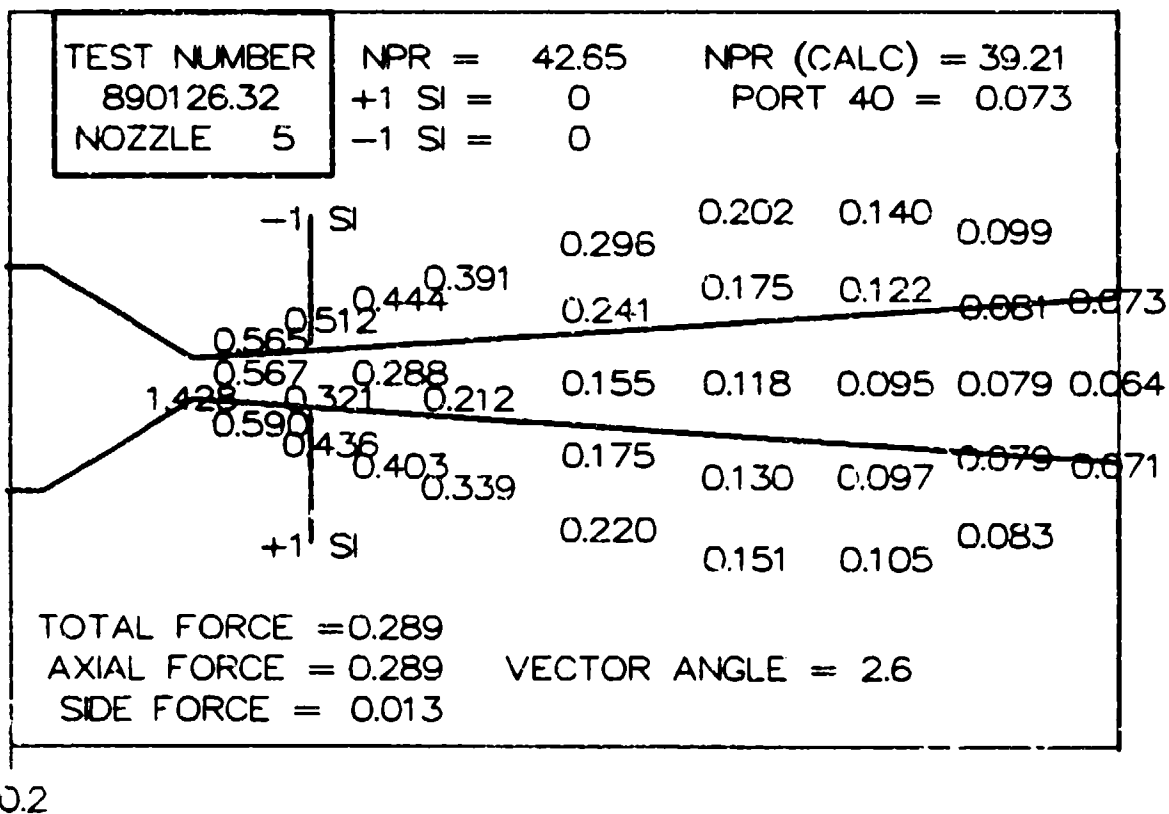


Fig 72 Static Pressure Profiles for Test Number 890126.32

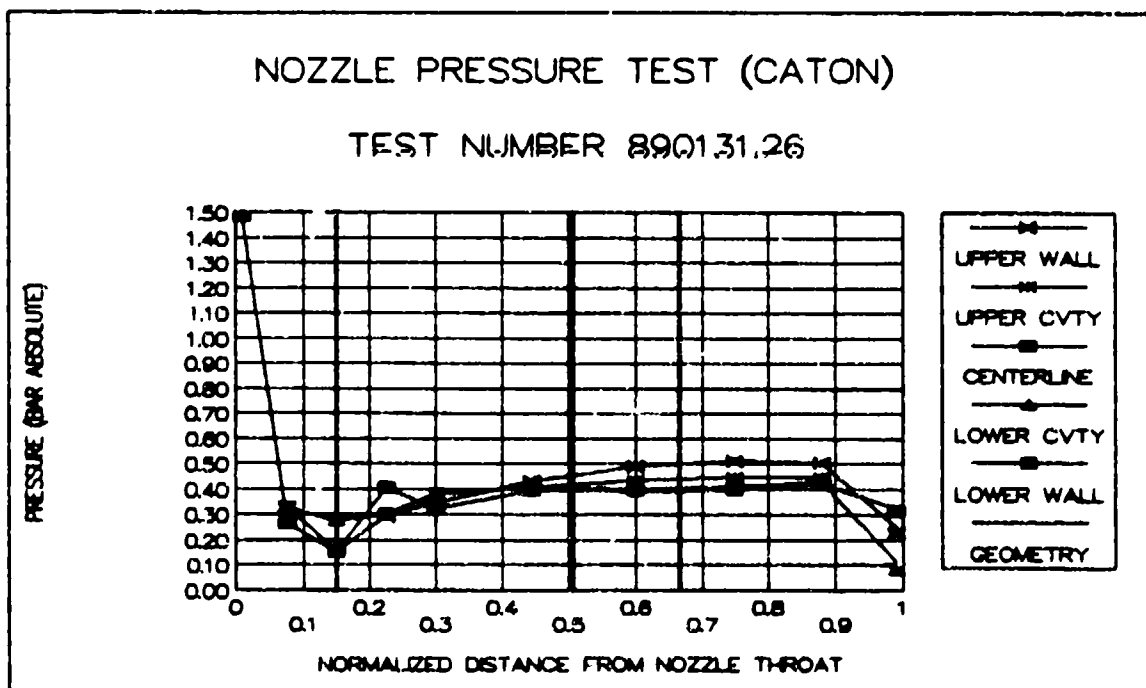
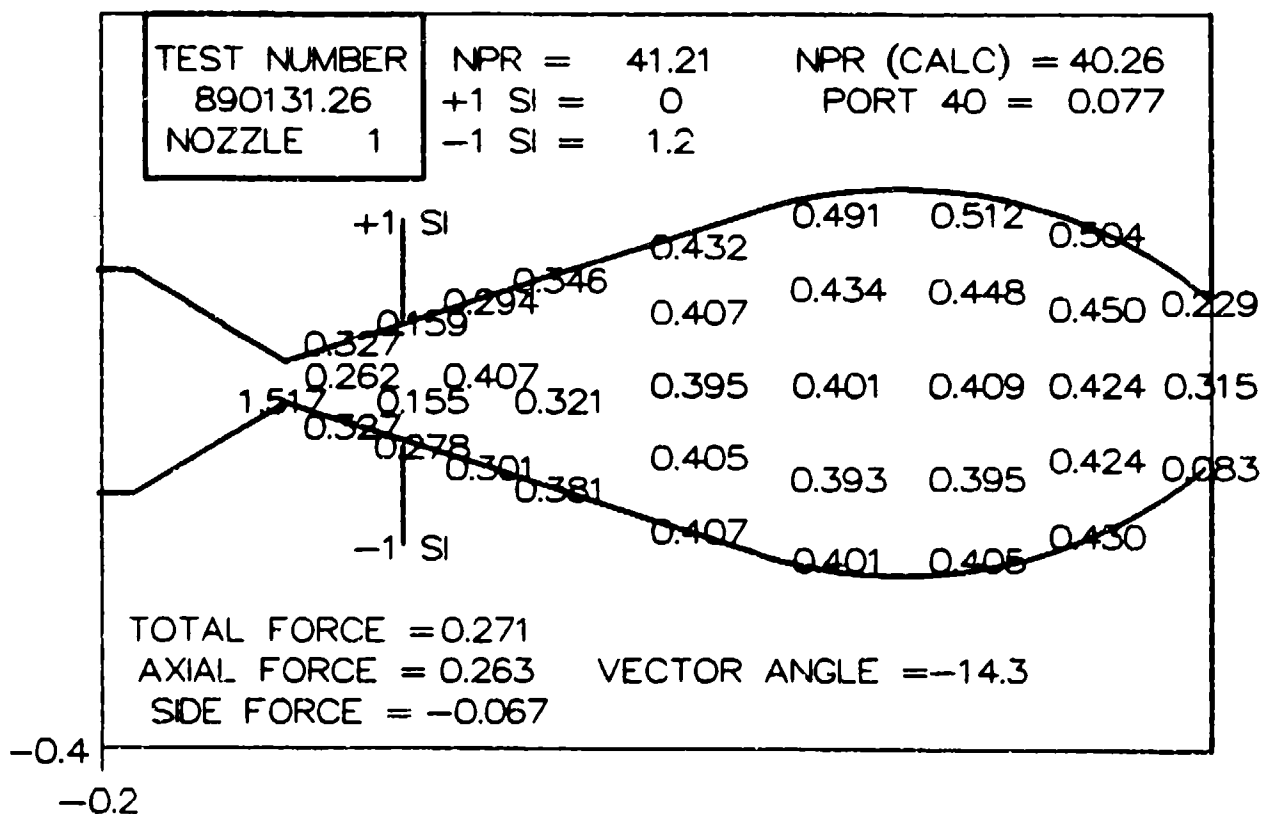


Fig 74 Static Pressure Profiles for Test Number 890131.26

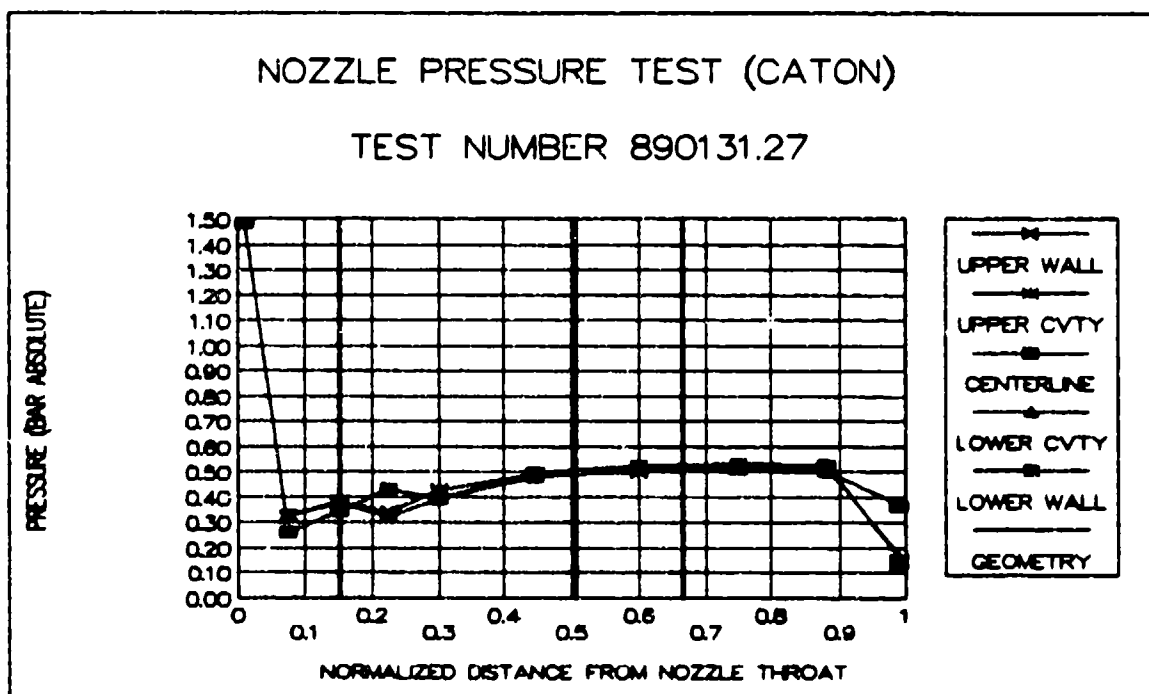
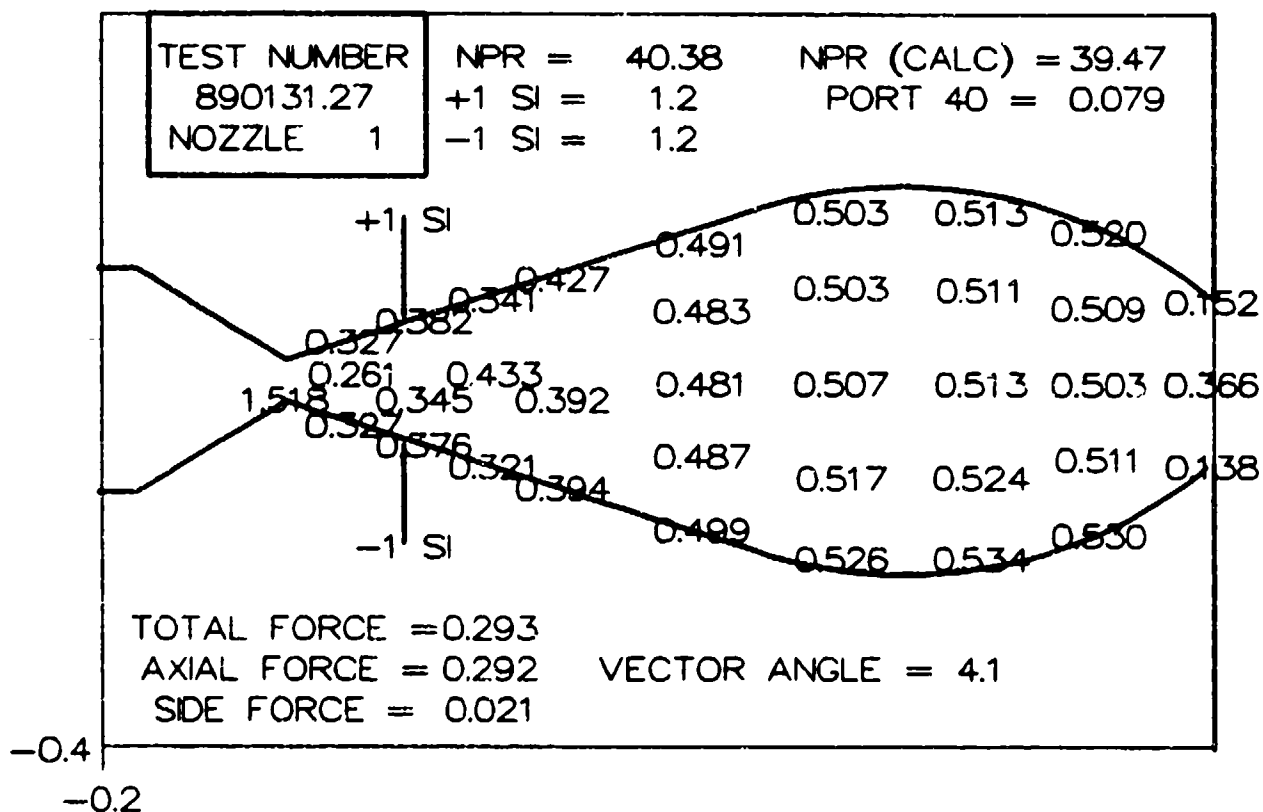


Fig 75 Static Pressure Profiles for Test Number 890131.27

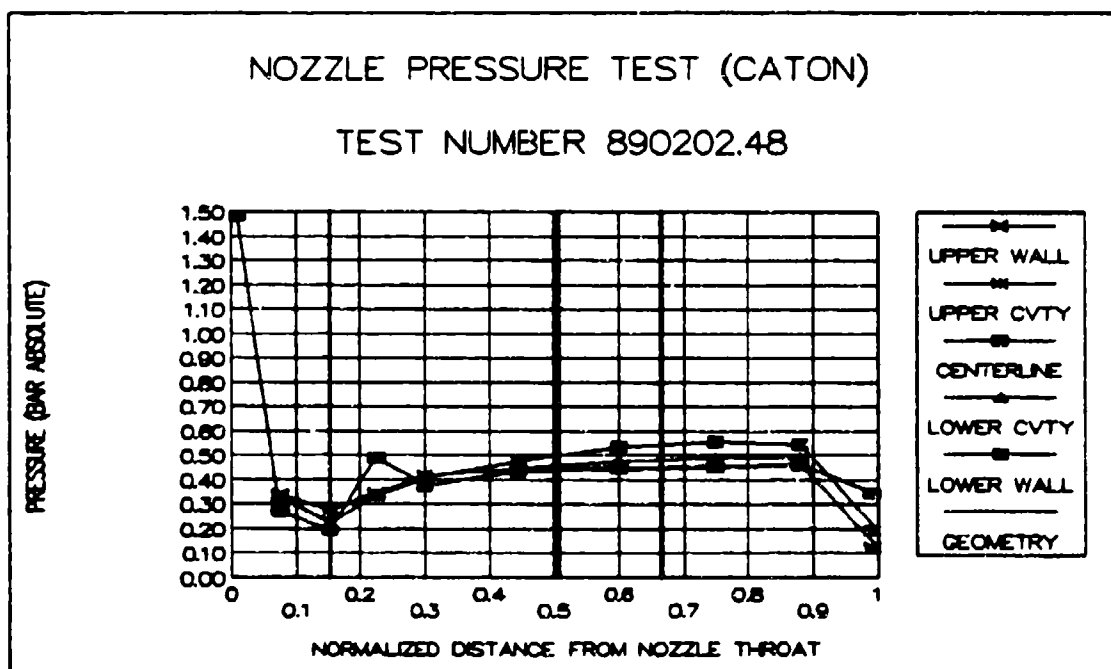
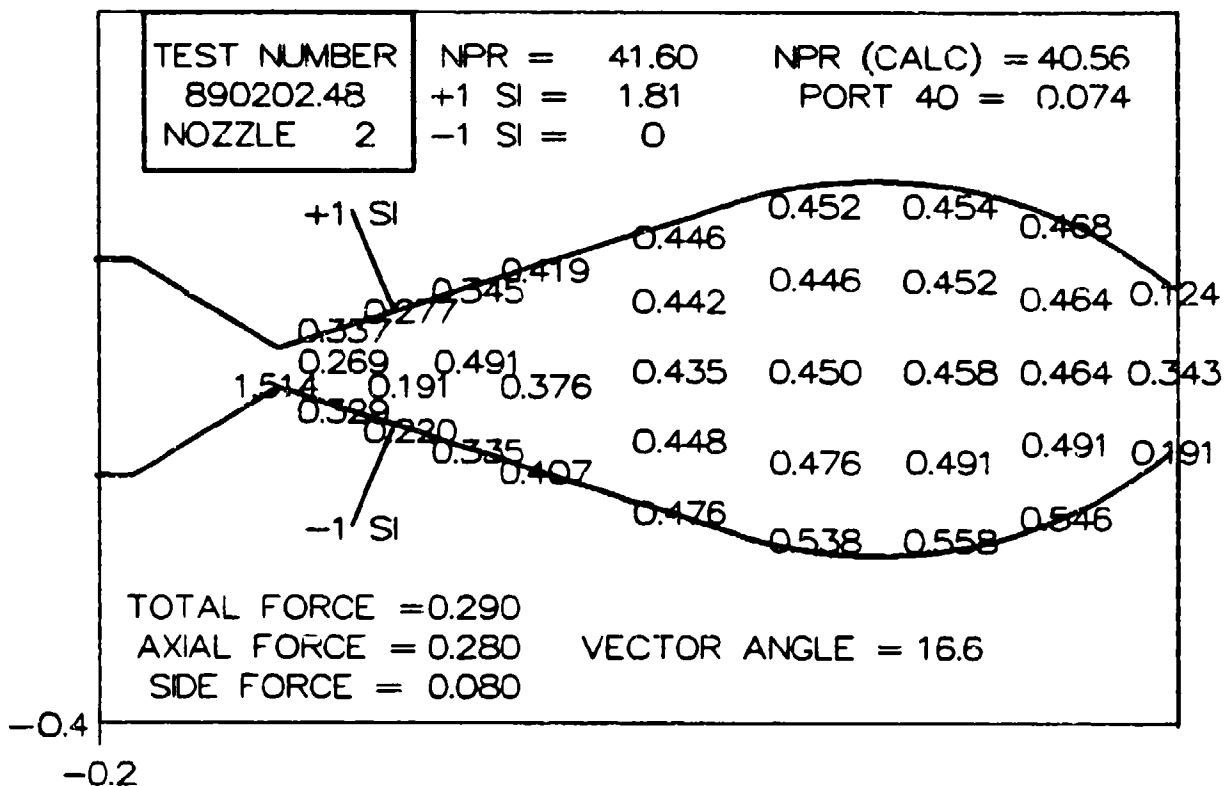


Fig 78 Static Pressure Profiles for Test Number 890202.48

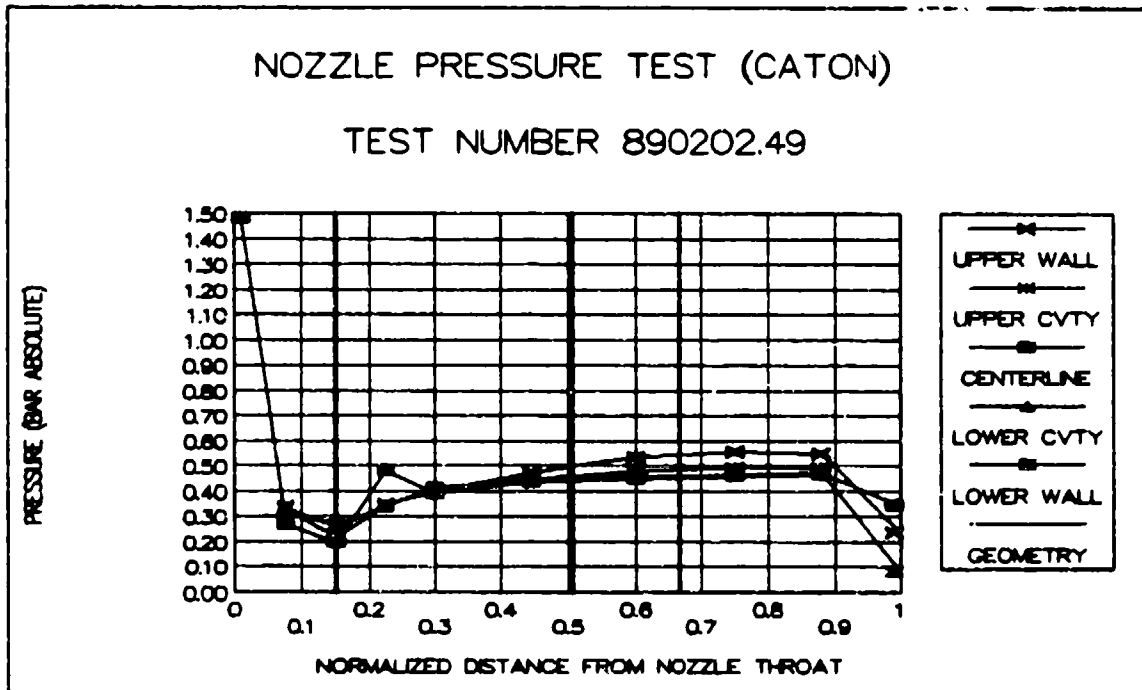
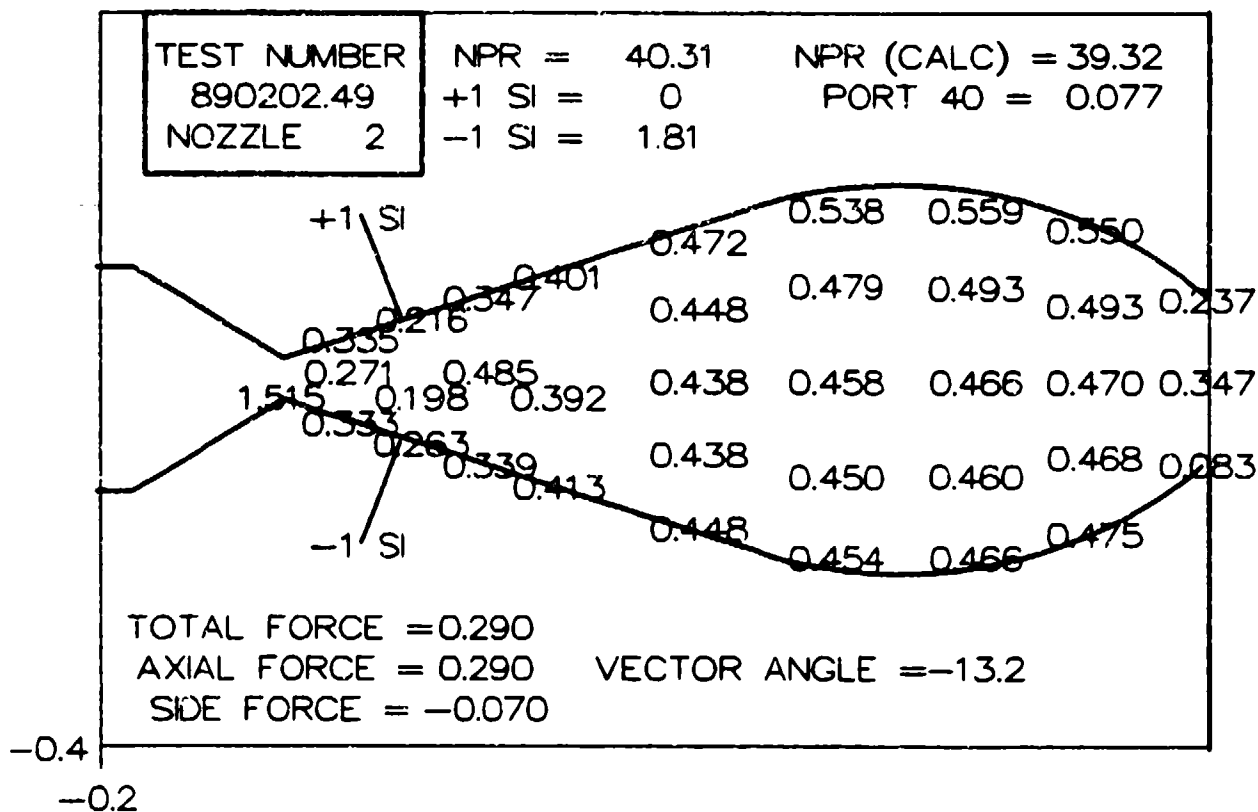


Fig 77 Static Pressure Profiles for Test Number 890202.49

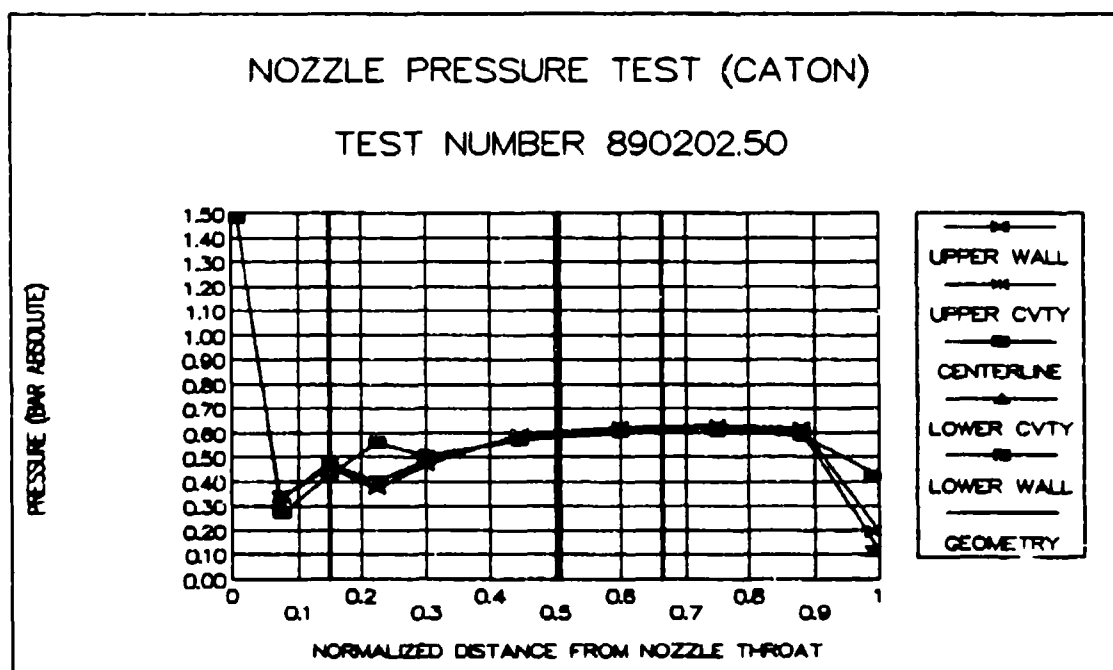
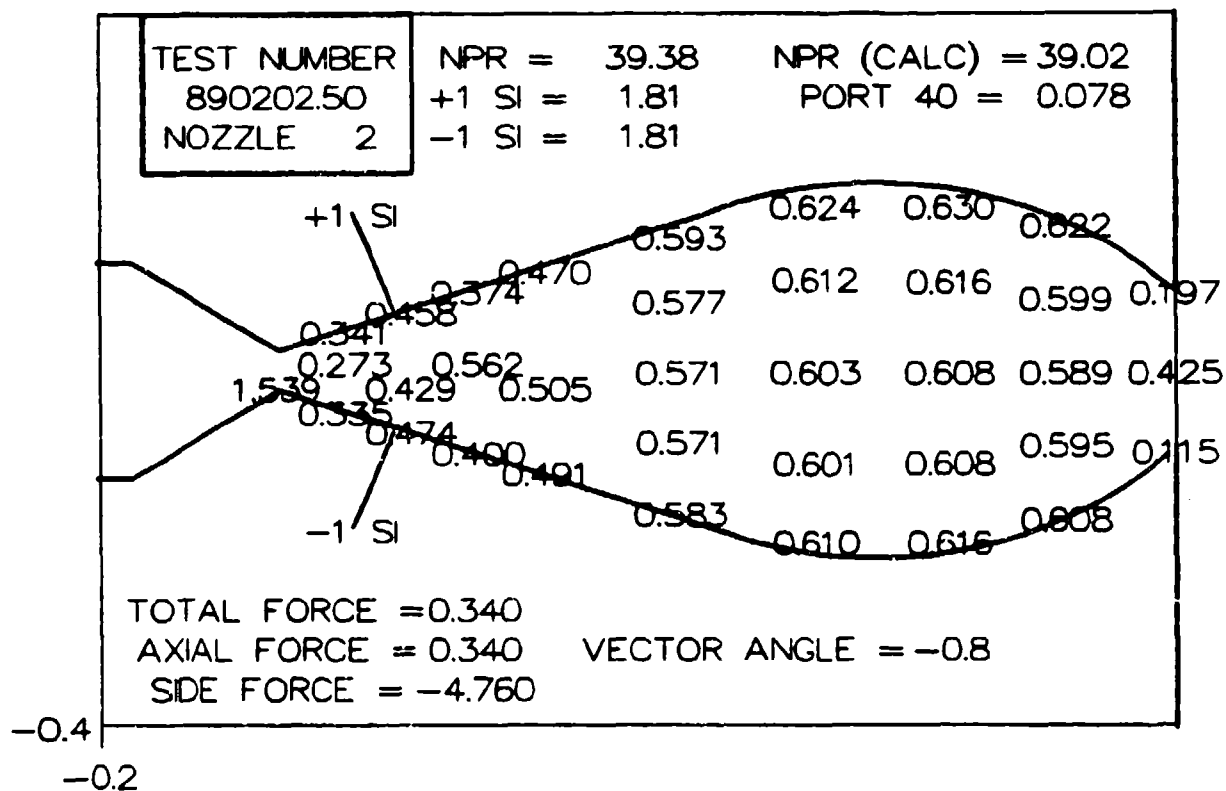


Fig 78 Static Pressure Profiles for Test Number 890202.50

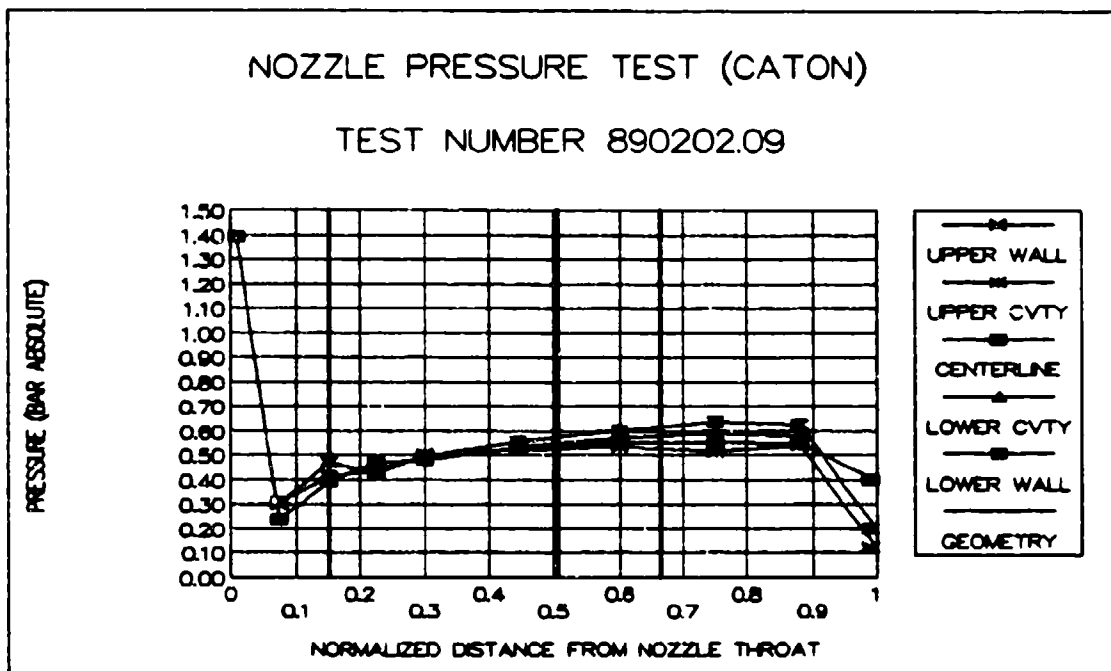
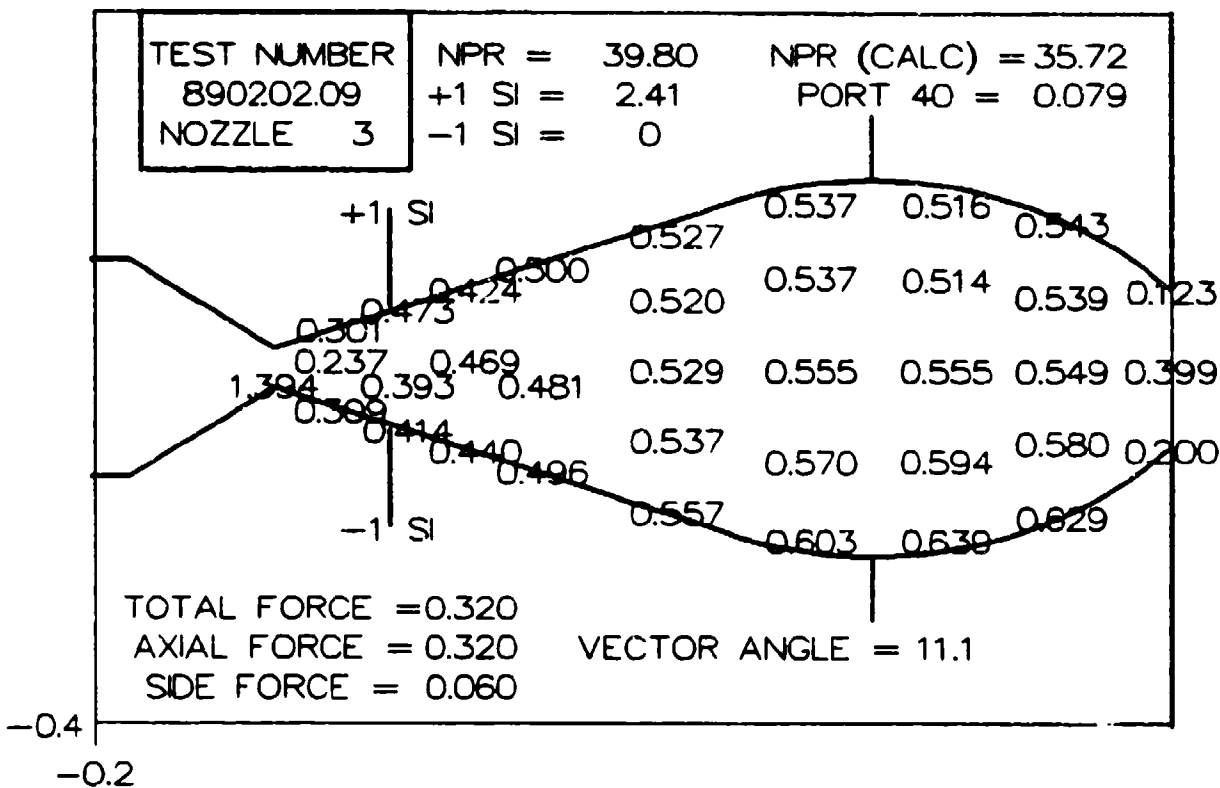


Fig 79 Static Pressure Profiles for Test Number 890202.09

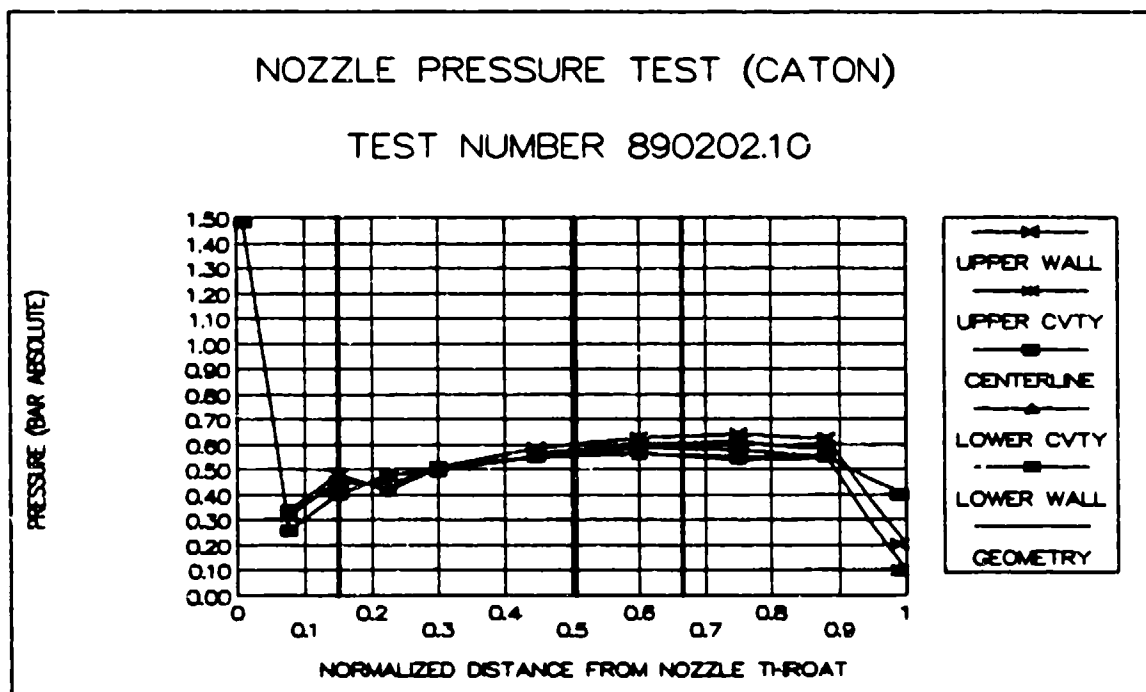
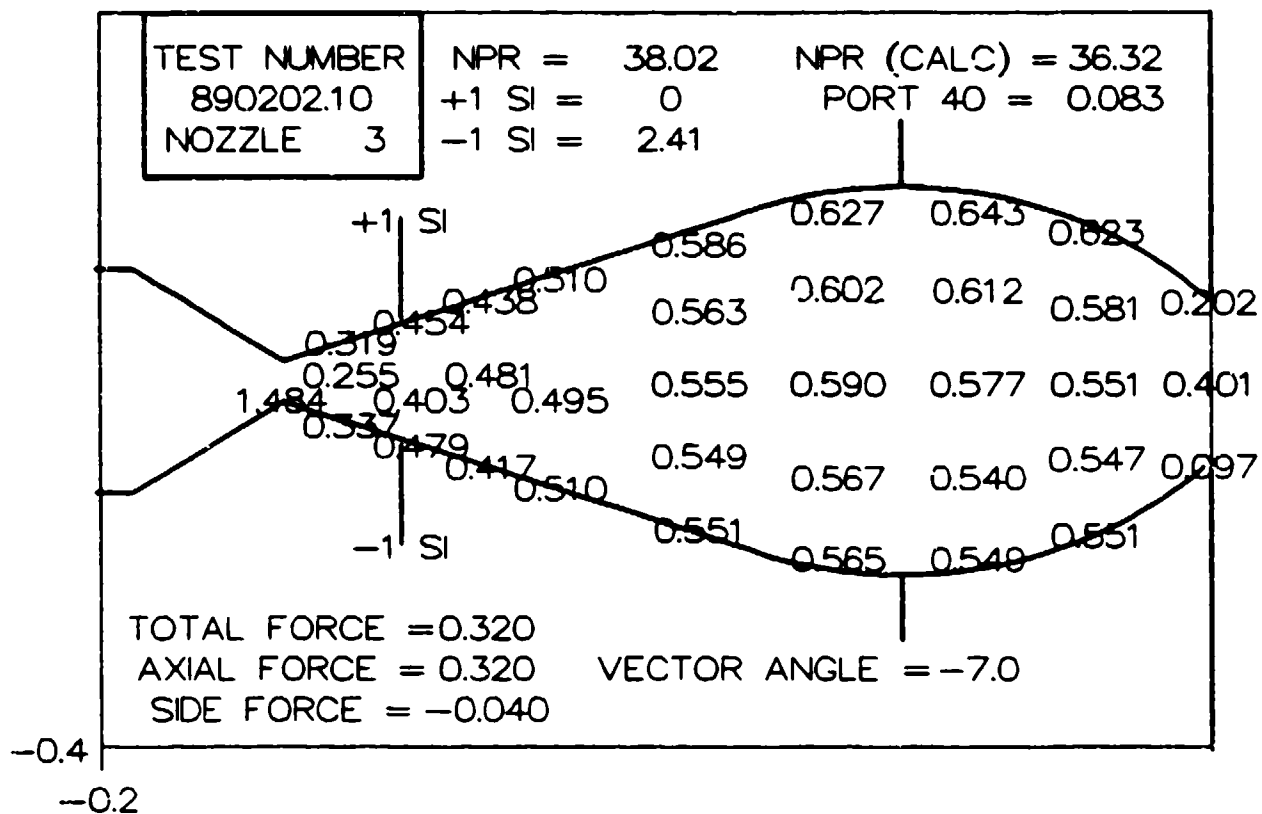


Fig 80 Static Pressure Profiles for Test Number 890202.10

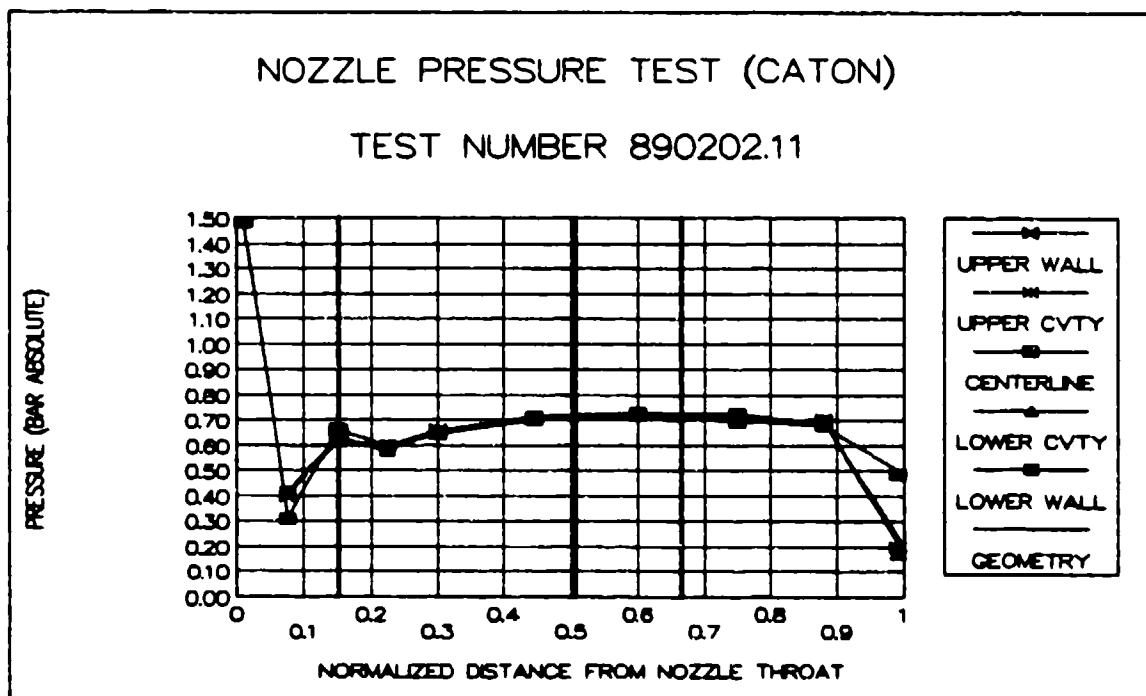
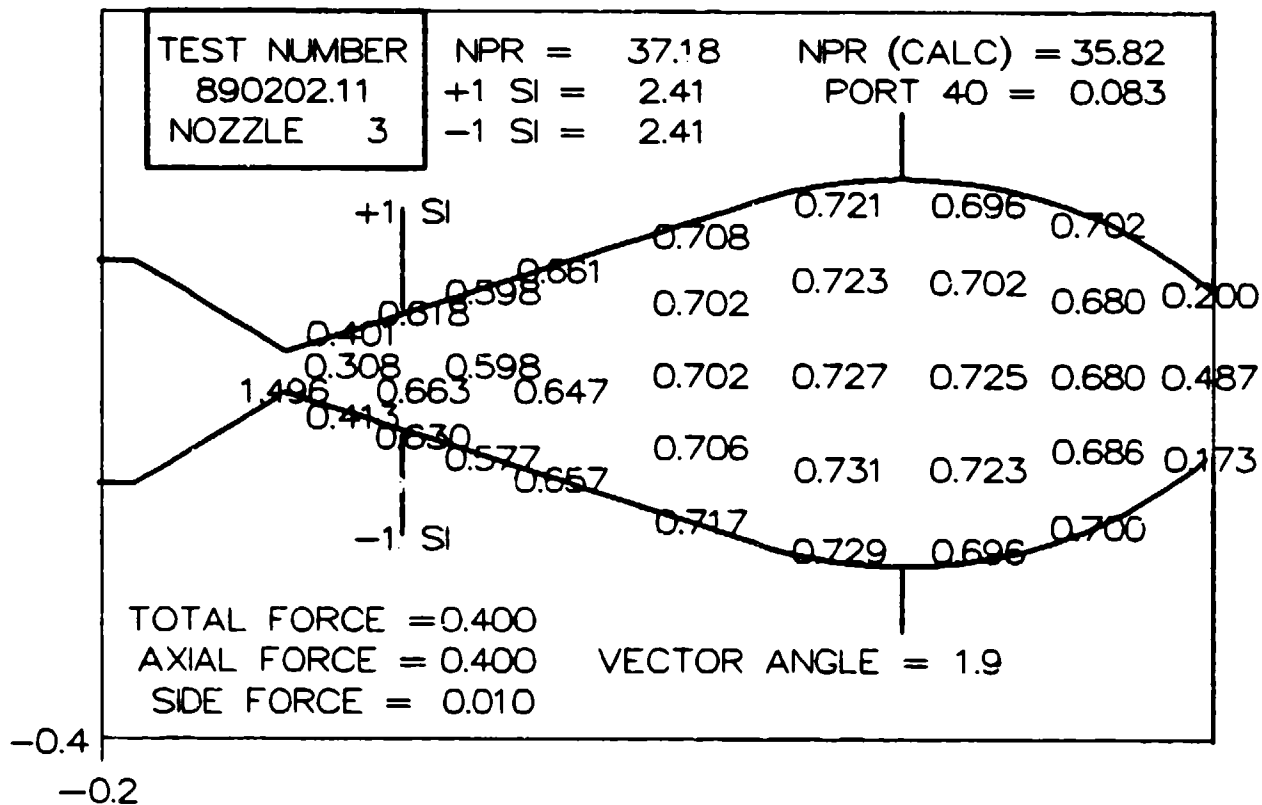


Fig 81 Static Pressure Profiles for Test Number 890202.11

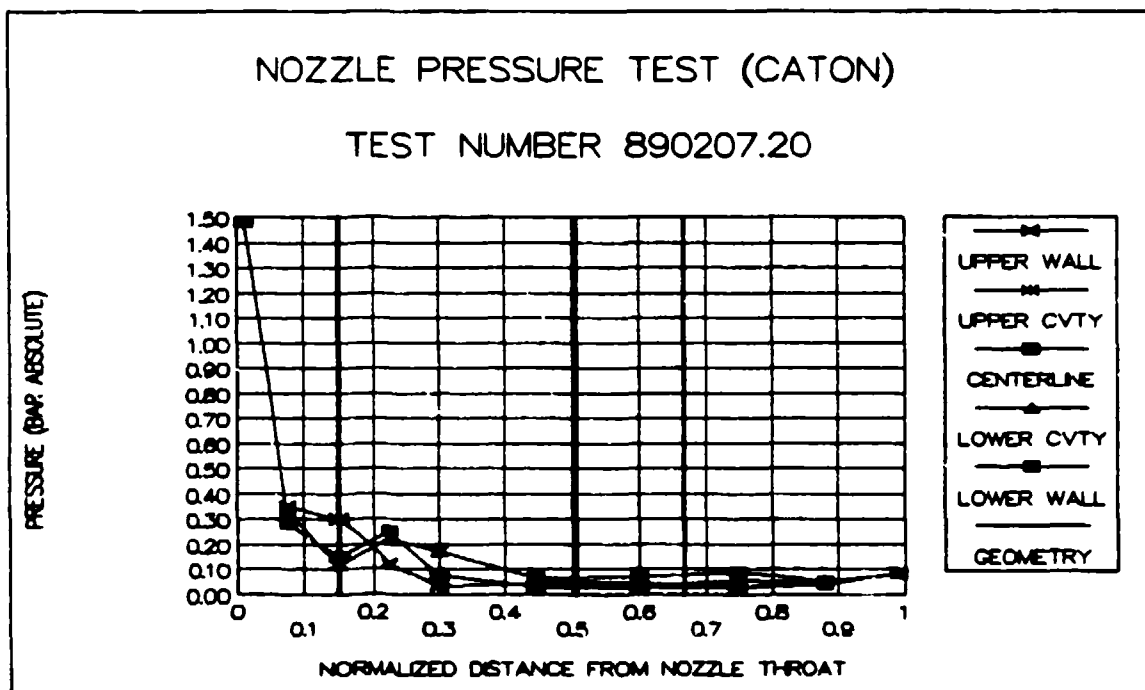
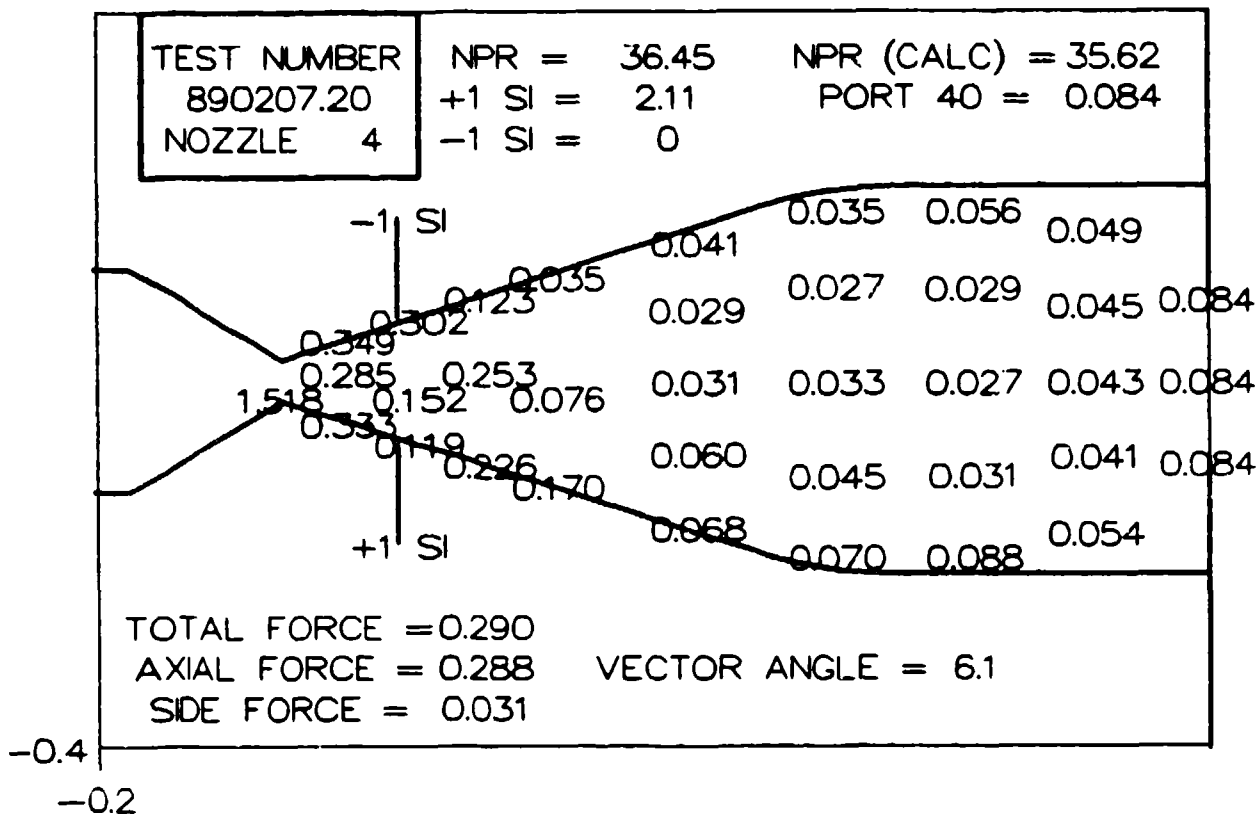


Fig 82 Static Pressure Profiles for Test Number 890207.20

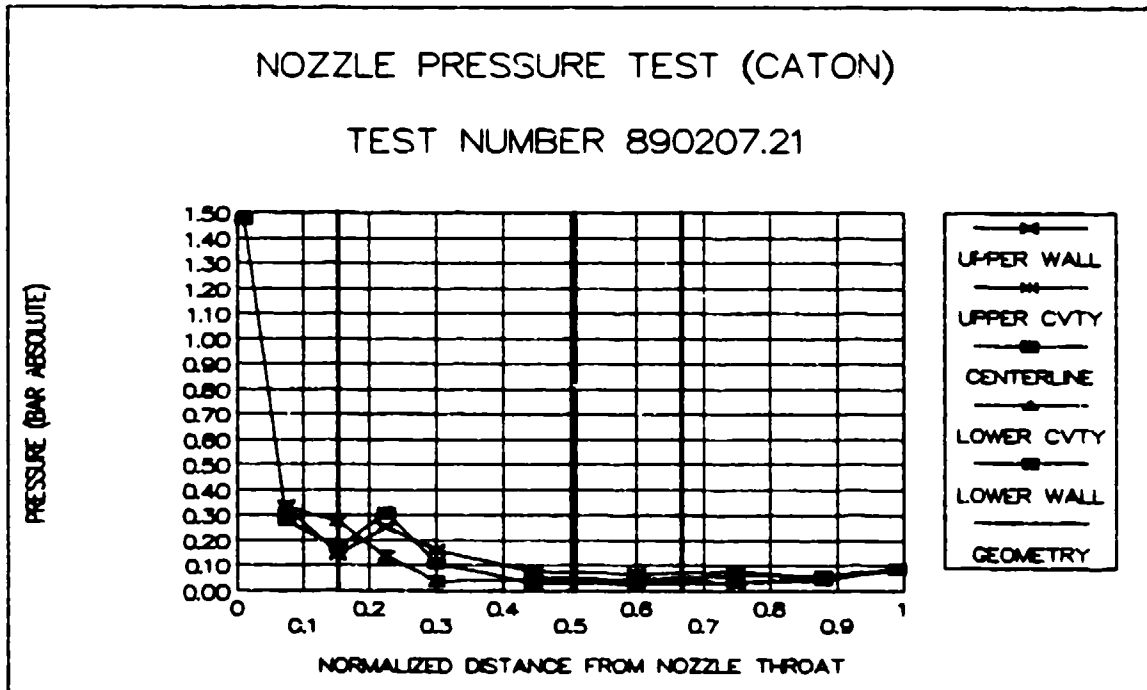
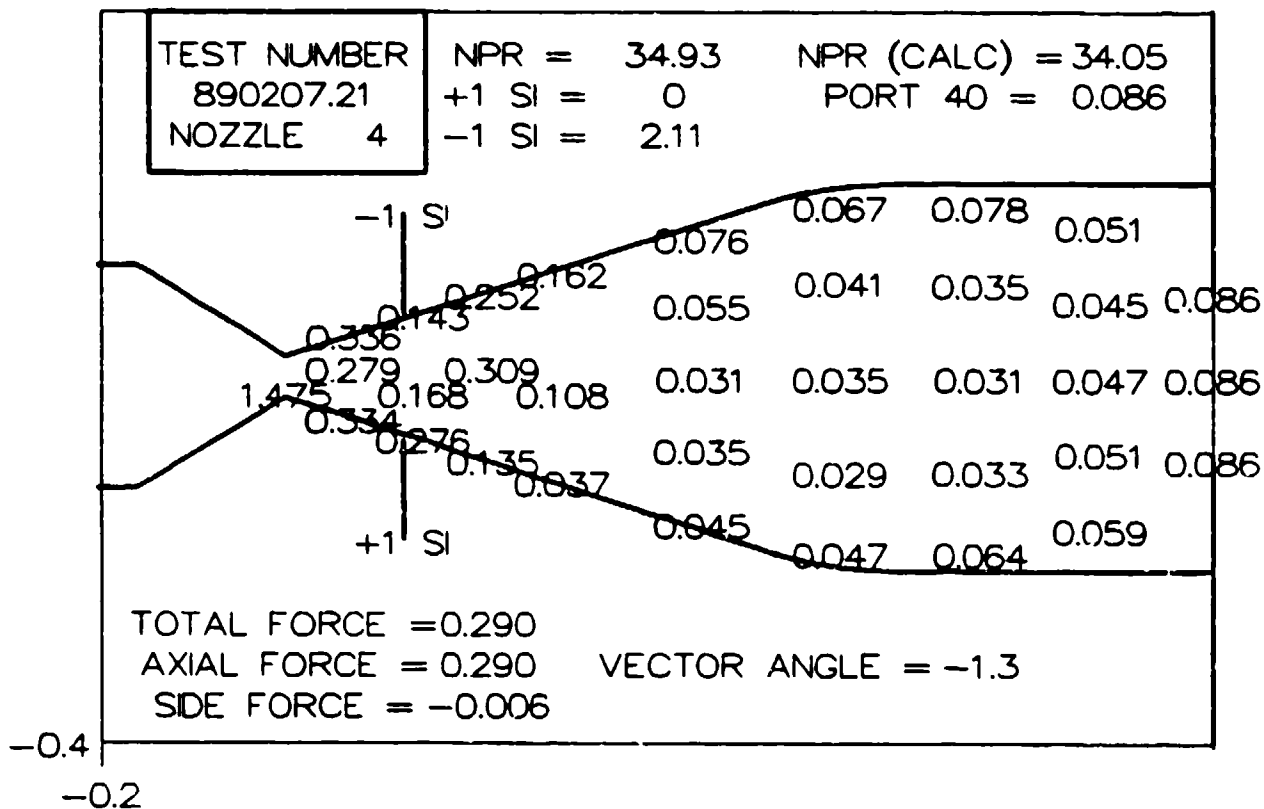


Fig 83 Static Pressure Profiles for Test Number 890207.21

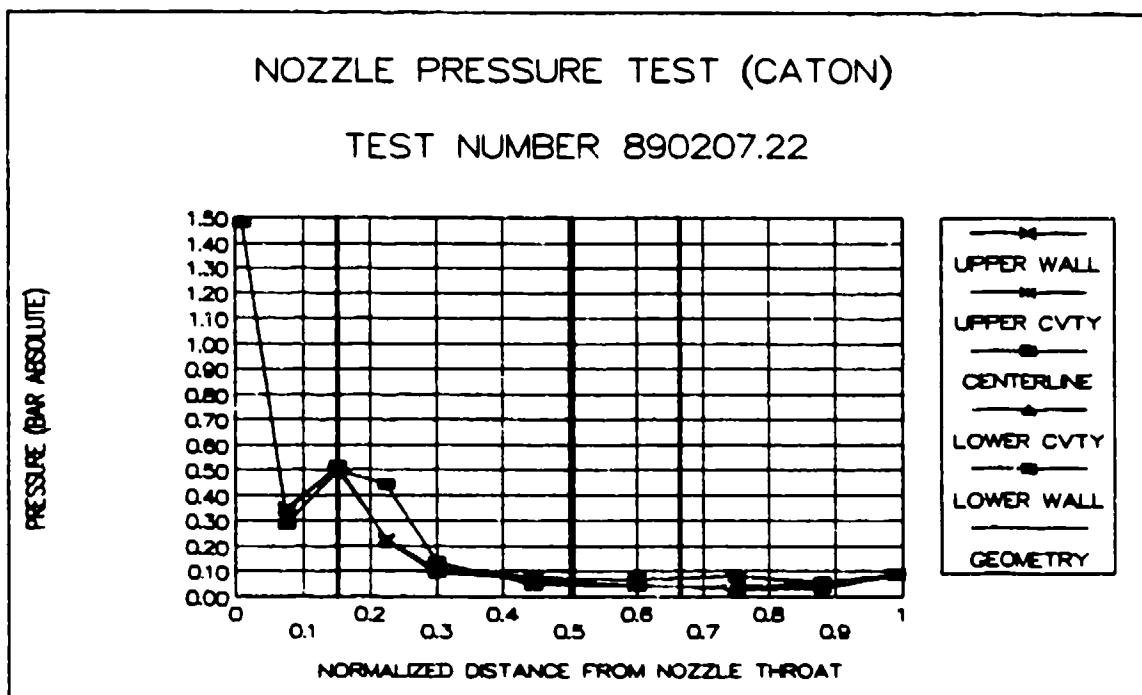
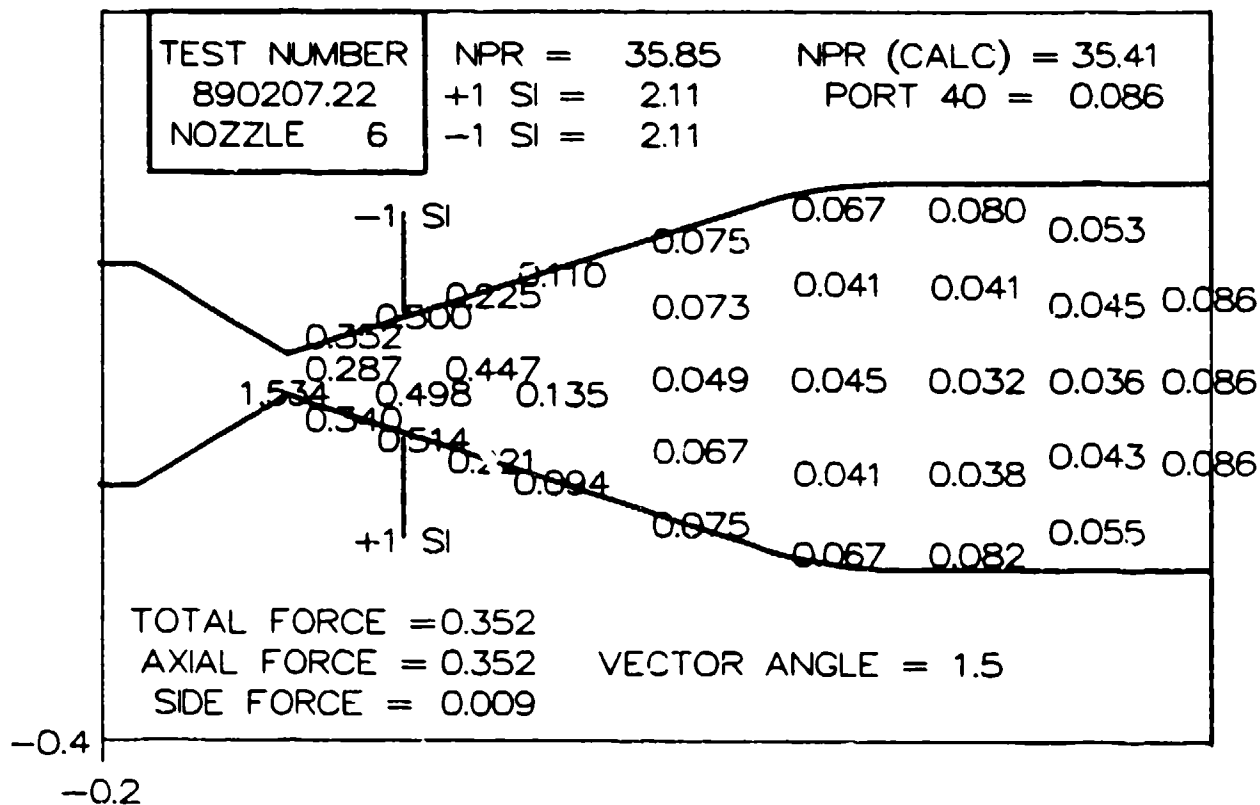


Fig 84 Static Pressure Profiles for Test Number 890207.22

Bibliography

1. Blondeaux, P. and B. de Bernardinis "On the Formation of Vortex Pairs Near Orifices," Journal of Fluid Mechanics, 1983.
2. Brinsmade, A. "Thrust Vector Control," Solid Rocket Technology, edited by M. Shorr and A. Zaehring. New York: Wiley and Sons, Inc., 1967.
3. Broadwell, James E. "Analysis of the Fluid Mechanics of Secondary Injection for Thrust Vector Control," AIAA Journal, 1: 1067-1075, May 1963.
4. Carter, J.M. "Thrust-Axis Control In Solid-Propellant Rocket Motors," Rocket Propulsion Technology Volume 1, Proceeding of the First Rocket Propulsion Symposium. 1-15. New York, Plenum Press, 1961.
5. Cates, James W. Two-Dimensional Confined Jet Thrust Vector Control with Flow Visualization and Variable Flow Geometry. MS Thesis AFIT/GAE/AA/85D-2. School of Engineering, Air Force Institute of Technology (AU), Wright-Patterson AFB OH, December 1985.
6. Chapman, Alan J. and William F. Walker Introductory Gas Dynamics. New York: Holt, Rinehart, and Winston, Inc., 1971.
7. Clemow, T. Short-Range Guided Weapons. London: Temple Press, 1961.
8. Fitzgerald, R.E. and R.F. Kampe "Boundary Layer TVC for Missile Applications," AIAA/SAC/ASME 19th Joint Propulsion Conference AIAA-83-1153. American Institute of Aeronautics and Astronautics, New York, 1983.
9. Green, C.J. and Foy McCullough Jr. "Liquid Injection Thrust Vector Control," AIAA Journal, 1: 573-578, March 1963.
10. Kayes, W.M. and M.E. Crawford. Convective Heat and Mass Transfer. New York: McGraw-Hill Book Company, 1980.
11. Lambert, P.G. and M.E. Franke. "Characteristics of Axisymmetric Confined Jet Thrust Vector Control," AIAA/ASME/SAE/ASEE 24th Joint Propulsion Conference, AIAA-88-3237, Washington, D.C., 1988.
12. Porzio, Anthony J. "Experimental Study of a Confined Jet Thrust Vector Control Nozzle," AIAA 24th Aerospace Sciences Meeting, AIAA-86-0448, Reno, Nevada 1986.

13. Schlichting, Hermann. Boundary-Layer Theory. New York: McGraw-Hill Book Company, 1979.
14. Shapiro, A.H. The Dynamics and Thermodynamics of Compressible Fluid Flow. Volume I. New York: The Ronald Press, 1953.
15. Sutton, George P. Rocket Propulsion Elements, Fifth Edition. New York: John Wiley and Sons, 1986.
16. Talda, Timothy A. Experimental Investigation of Two-Dimensional Confined Thrust Vector Control. MS Thesis AFIT/GAE/AA/87D-22. School of Engineering, Air Force Institute of Technology (AU), Wright-Patterson AFB OH, December 1987.
17. Thompson, R.V. Theoretical Determination of the Point of Separation in a Compressible, Turbulent, Supersonic Boundary Layer Subjected to an Adverse Pressure Gradient. ASME Paper 67-WA/FE-38, American Society of Mechanical Engineers, New York, 1967.
18. von Karman Institute for Fluid Dynamics. Facilities and Instrumentation 1986. Wyckmans and Company, Brussels, Belgium, 1986.
19. Zucrow, Maurice J. and Joe D. Hoffman Gas Dynamics. Volume I. New York: John Wiley and Sons, 1976.
20. Zukoski, Edward E. and Frank W. Spaid. "Secondary Injection of Gases into a Supersonic Flow," AIAA Journal, 2: 1689-1696, October 1964.

Vita

Captain Jeffrey L. Caton was born on 9 September 1960 in Arlington, Virginia. He graduated from high school in Nokesville, Virginia in 1978 and attended the University of Virginia, from which he received the degree of Bachelor of Science in Chemical Engineering in May 1982. Upon graduation, he received a commission in the USAF through the ROTC program. He reported to Wright-Patterson AFB, Ohio in September 1982 where he completed USAF System Acquisition Training and Reliability and Maintainability training in April 1983. He then served as Lead Product Assurance Engineer for the F/FB-111 Avionics Modernization Program, Deputy for Strategic Systems, Aeronautical Systems Division until September 1984 when he became Mission Planning Systems Integration Engineer for the Advanced Cruise Missile Program, Deputy for Strategic Systems, Aeronautical Systems Division. Following this assignment, he entered the School of Engineering, Air Force Institute of Technology, in June 1987.

REPORT DOCUMENTATION PAGE

Form Approved
OMB No. 0704-0188

1a. REPORT SECURITY CLASSIFICATION Unclassified			1b. RESTRICTIVE MARKINGS		
2a. SECURITY CLASSIFICATION AUTHORITY			3. DISTRIBUTION / AVAILABILITY OF REPORT Approved for public release; Distribution unlimited		
2b. DECLASSIFICATION / DOWNGRADING SCHEDULE					
4. PERFORMING ORGANIZATION REPORT NUMBER(S) AFIT/GAE/AA/89M-1			5. MONITORING ORGANIZATION REPORT NUMBER(S)		
6a. NAME OF PERFORMING ORGANIZATION School of Engineering		6b. OFFICE SYMBOL (if applicable) AFIT/ENG		7a. NAME OF MONITORING ORGANIZATION	
6c. ADDRESS (City, State, and ZIP Code) Air Force Institute of Technology (AU) Wright-Patterson AFB, Ohio 45433-6583				7b. ADDRESS (City, State, and ZIP Code)	
8a. NAME OF FUNDING / SPONSORING ORGANIZATION von Karman Institute		8b. OFFICE SYMBOL (if applicable)		9. PROCUREMENT INSTRUMENT IDENTIFICATION NUMBER	
8c. ADDRESS (City, State, and ZIP Code) von Karman Institute for Fluid Dynamics Chaussee de Waterloo, 72 1640 Rhode-St-Genese, Belgium				10. SOURCE OF FUNDING NUMBERS	
		PROGRAM ELEMENT NO.		PROJECT NO.	TASK NO.
				WORK UNIT ACCESSION NO.	
11. TITLE (Include Security Classification) TWO-DIMENSIONAL CONFINED JET THRUST VECTOR CONTROL: OPERATING MECHANISMS AND PERFORMANCE					
12. PERSONAL AUTHOR(s) Jeffrey L. Caton, Captain, USAF					
13a. TYPE OF REPORT Thesis		13b. TIME COVERED FROM _____ TO _____		14. DATE OF REPORT (Year, Month, Day) March, 1989	
15. PAGE COUNT 165					
16. SUPPLEMENTARY NOTATION					
17. COSATI CODES			18. SUBJECT TERMS (Continue on reverse if necessary and identify by block number)		
FIELD	GROUP	SUB-GROUP			
21	08		Thrust Control, Secondary Injection, Two-Dimensional, Thrust Vector Control Systems, Flow Visualization		
19. ABSTRACT (Continue on reverse if necessary and identify by block number) Dr. Milton E. Franke					
20. DISTRIBUTION / AVAILABILITY OF ABSTRACT <input checked="" type="checkbox"/> UNCLASSIFIED/UNLIMITED <input type="checkbox"/> SAME AS RPT. <input type="checkbox"/> DTIC USERS			21. ABSTRACT SECURITY CLASSIFICATION Unclassified		
22a. NAME OF RESPONSIBLE INDIVIDUAL Dr. Milton E. Franke, Professor			22b. TELEPHONE (Include Area Code) 513-255-2562		22c. OFFICE SYMBOL AFIT/ENY

UNCLASSIFIED

An experimental investigation of two-dimensional confined jet thrust vector control nozzles was performed. Thrust vector control was accomplished by using secondary flow injection in the diverging section of the nozzle. Schlieren photographs and video tapes were used to study flow separation and internal shock structures. Nozzle performance parameters were determined for nozzle flow with and without secondary flows. These parameters included nozzle forces, vector angles, thrust efficiencies, and flow switching response times. Vector angles as great as 18 degrees with thrust efficiencies of 0.79 were measured. Several confined jet nozzles with variations in secondary flow port design were tested and results were compared to each other. Converging-diverging nozzles of similar design to the confined jet nozzles were also tested and results were compared to the confined jet nozzle results.

Existing prediction models for nozzle side to axial force ratio were evaluated. A model for nozzle total forces based on shock losses that predicted values very close to actual results was developed. *Figure 1. Two dimensional flow*
through a jet control jets, Pocket nozzles, No. 1
Figure 2. Pocket nozzles, Thrust, 1000 lb

UNCLASSIFIED